Spektrální metody

Principy analytických metod

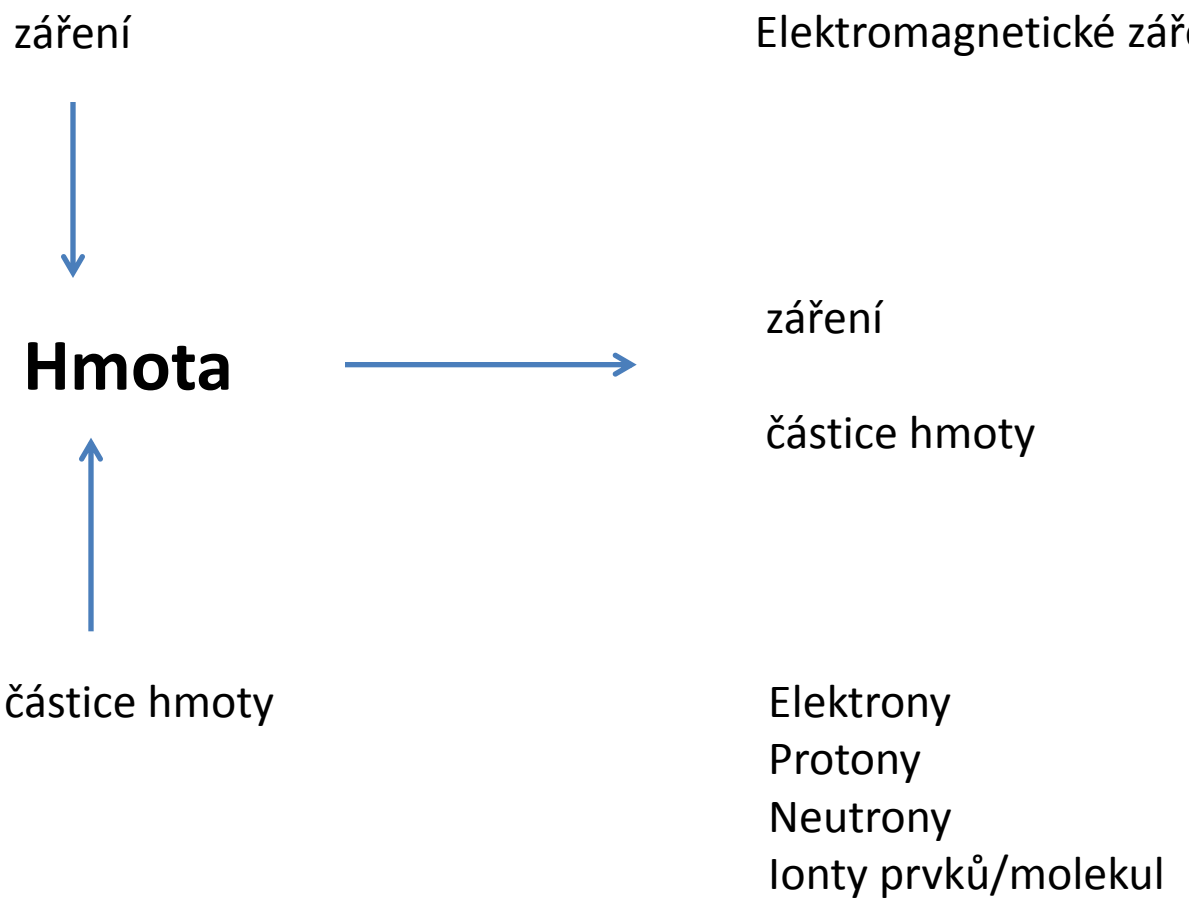

Elektromagnetické záření

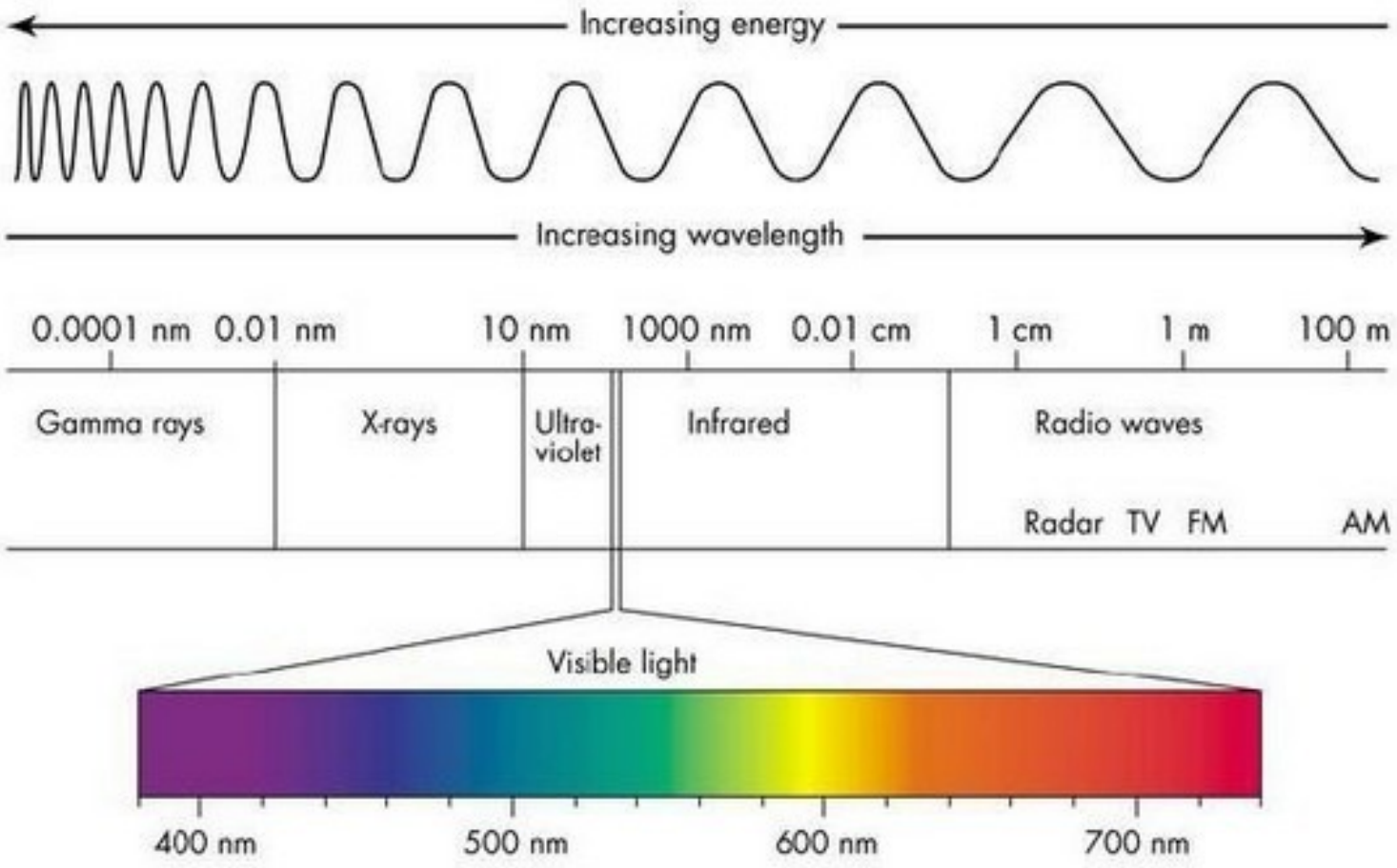

Vlnění

Částice

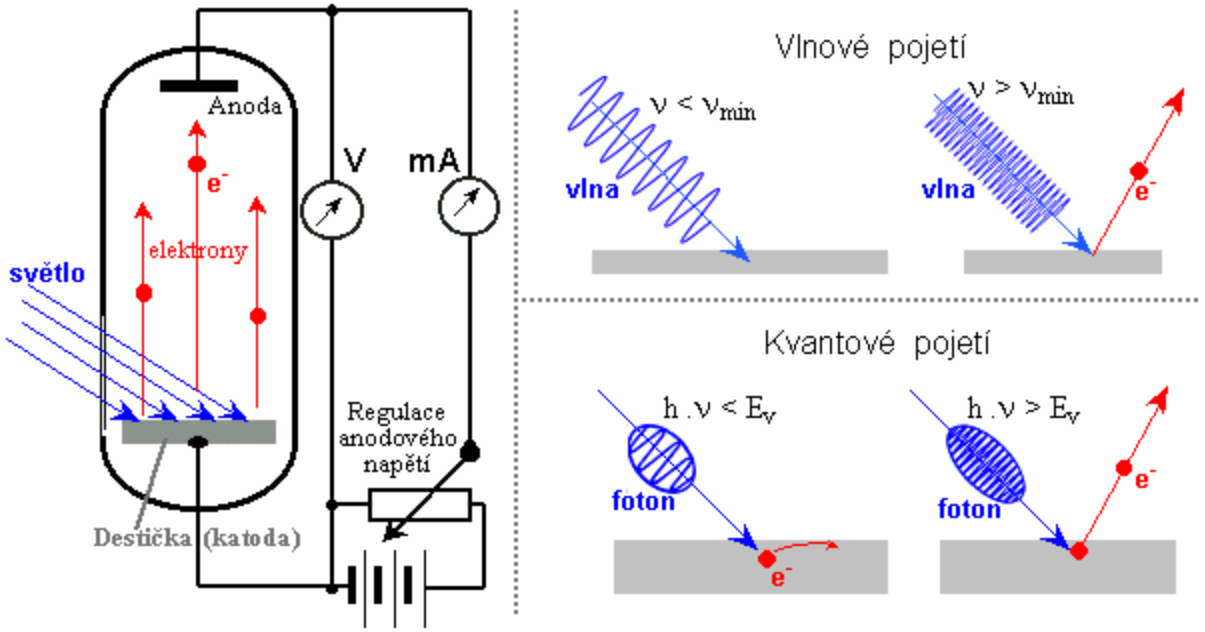

Každá mikročástice o hmotnosti m pohybující se rychlostí v, se může chovat jako vlna o vlnové délce

$$\lambda = \frac{h}{p} = \frac{h}{\gamma m v} = \frac{h}{mv}\sqrt{1 - \frac{v^2}{c^2}}$$

***De Broglieova-Comptonova* vlnová délka**

Stavba atomu

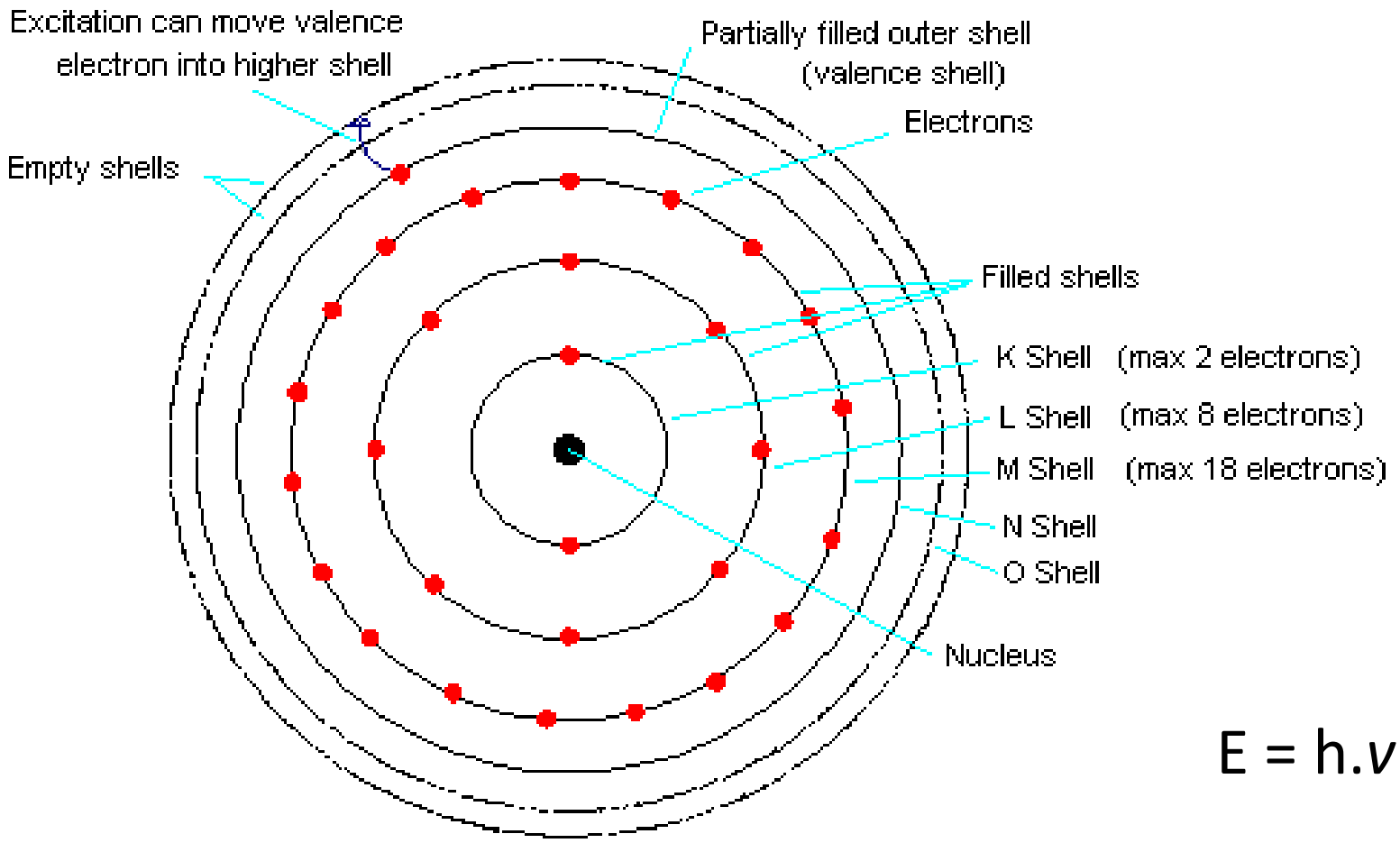

SIMPLIFIED ORBITAL MODEL OF A MANY-ELECTRON ATOM

$E = h.\nu$

UV záření
Rentgenové záření

Kovalentní vazba

Vibrační spektrometrie:

Infračervená

Ramanova

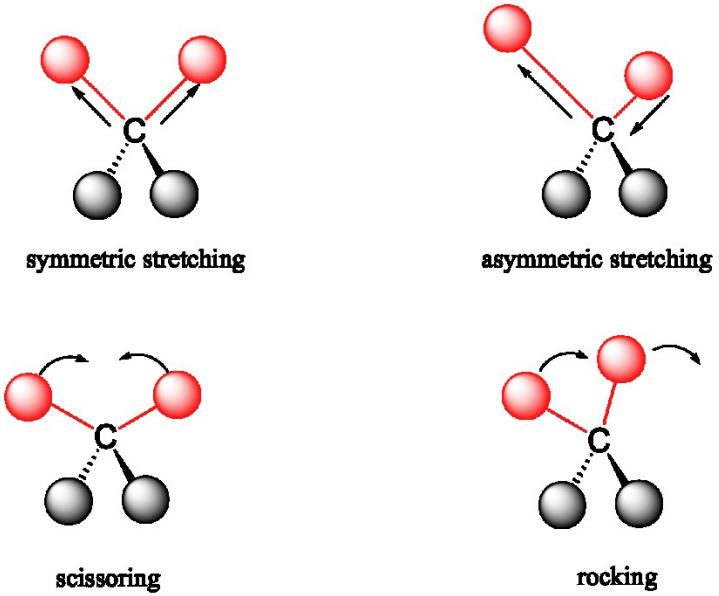

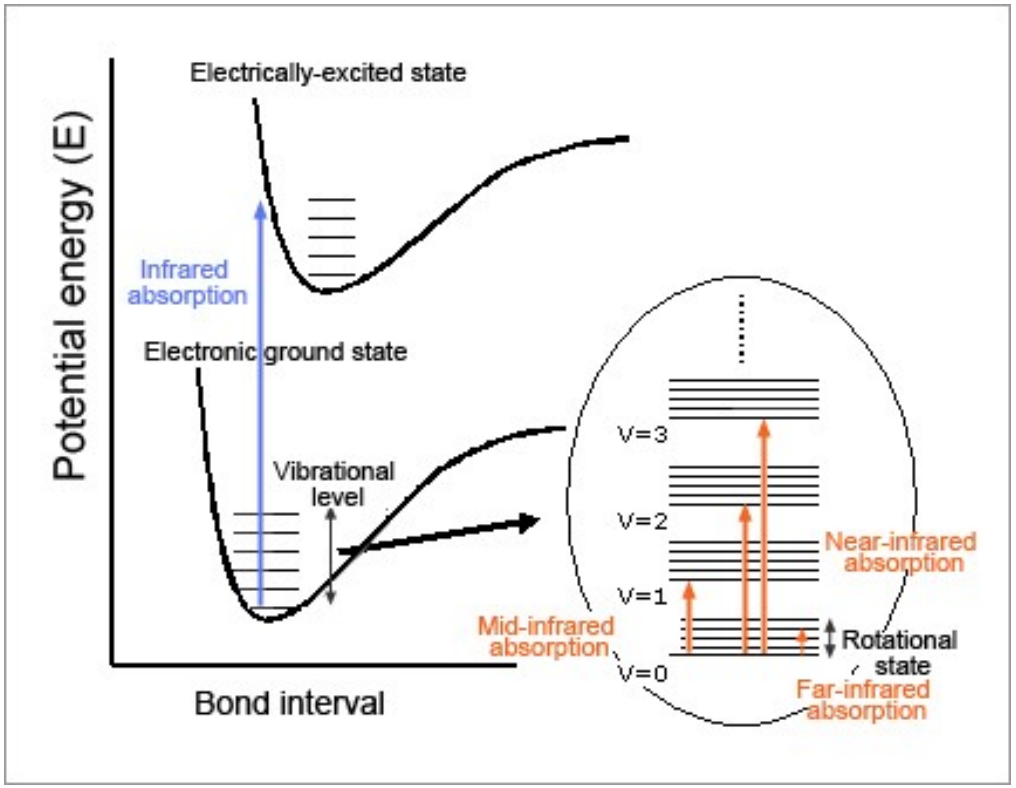

Analytické metody

„bulk“ (průměrná složení) vs lokální analýza

Destruktivní
Semidestruktivní
Nedestruktivní

Kvalitativní
Semikvantitativní
Kvantitativní

Atomová spektrometrie
Molekulová spektrometrie

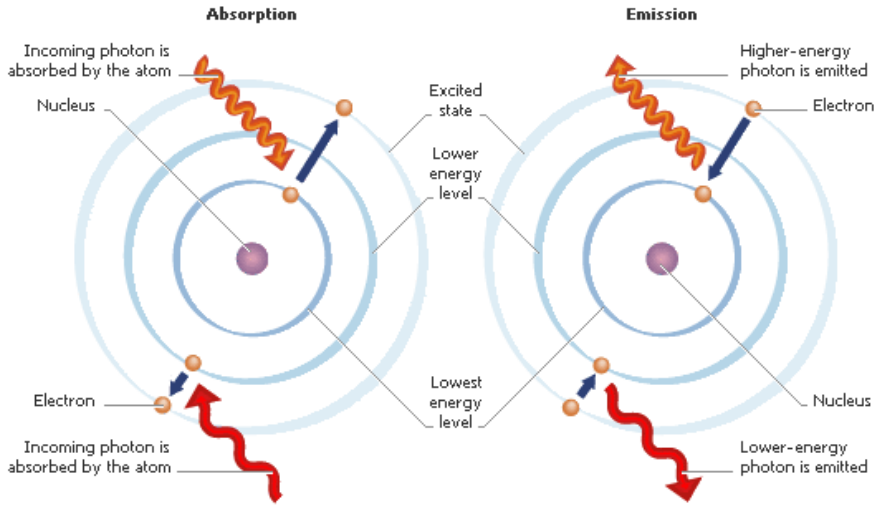

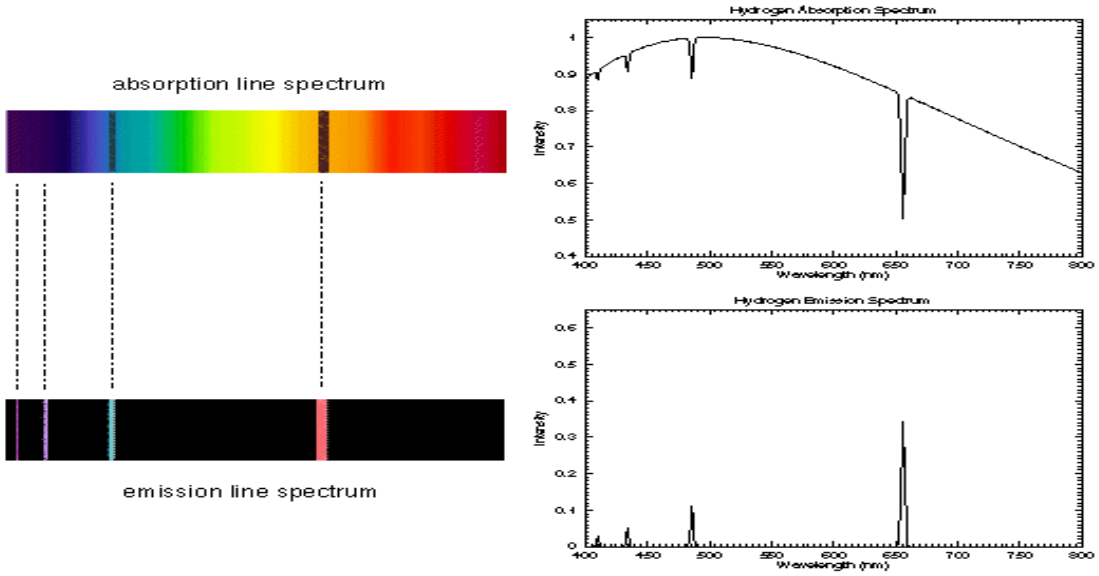

Two ways of showing the same spectra: on the **left** are pictures of the dispersed light and on the **right** are plots of the intensity vs. wavelength. Notice that the pattern of spectral lines in the absorption and emission line spectra are the **same** since the gas is the same.

Atomová absorpční spektrometrie

Roztoková analýza

destruktivní

V plameni

V kyvetě

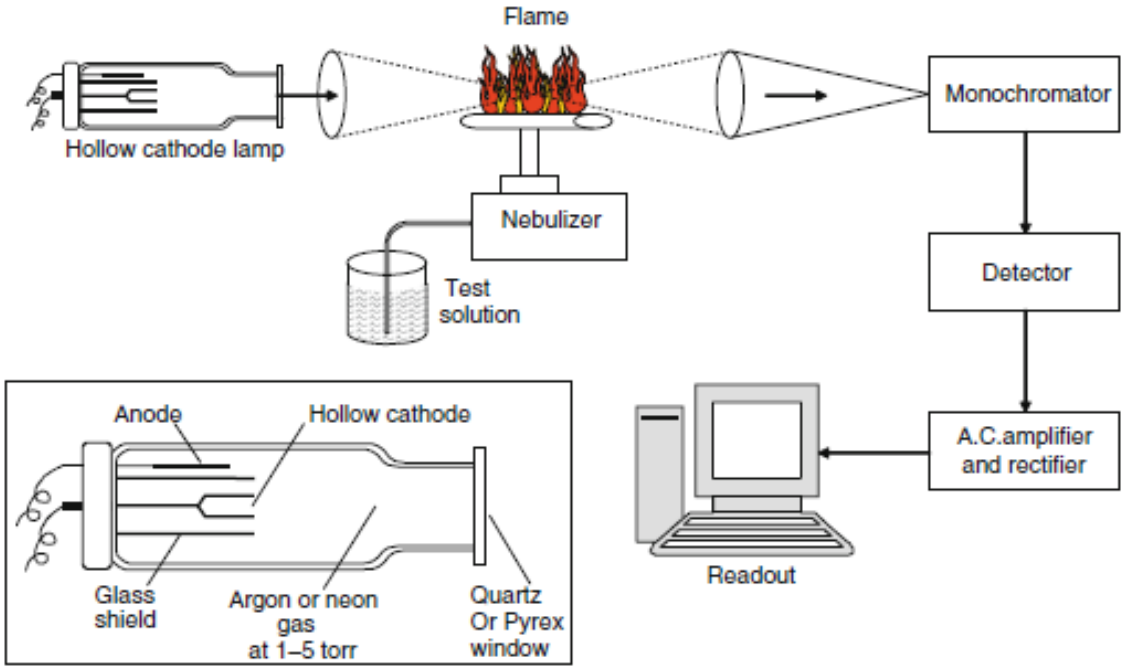

Fig. 34.1 Atomic absorption with hollow cathode lamp (From SKOOG. Principles of Instrumental Analysis, 5E. © 1998 Brooks/Cole, a part of Cengage Learning, Inc. Reproduced by permission. www.cengage.com/permissions)

Atomová emisní spektrometrie s indukčně vázaným plazmatem (ICP-OES)

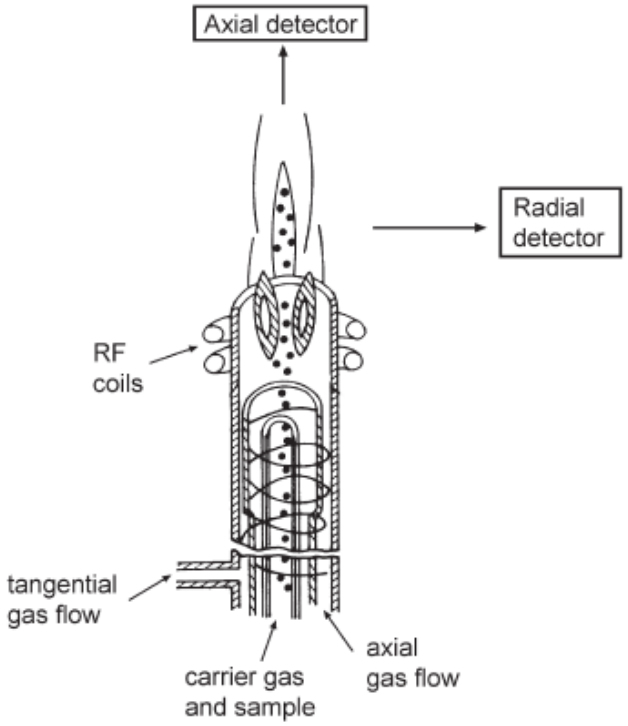

Figure 2.4 Schematic diagram of an ICP torch. The sample is carried into the torch by the carrier argon gas, and is ignited by radio-frequency heating from the RF coils. The tangential argon flow lifts the flame from the burner, preventing melting. The position of the detector in axial or radial mode is shown. (From Pollard *et al.*, 2007; Fig. 3–3, by permission of Cambridge University Press.)

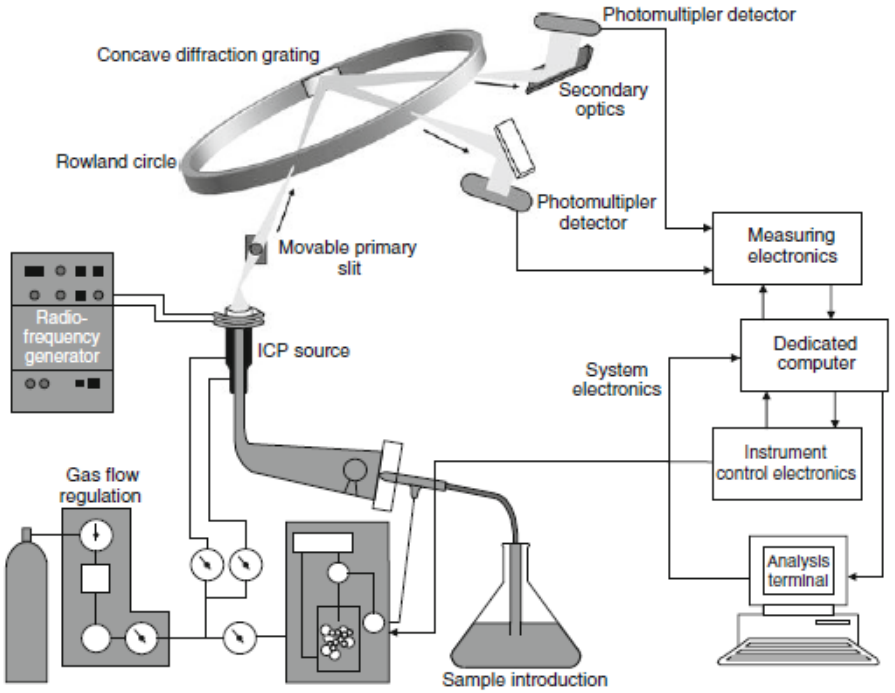

Fig. 34.2 Inductively coupled plasma polychromator (From SKOOG. Principles of Instrumental Analysis, 5E. © 1998 Brooks/Cole, a part of Cengage Learning, Inc. Reproduced by permission. www.cengage.com/permissions)

Roztoková analýza

Destruktivní

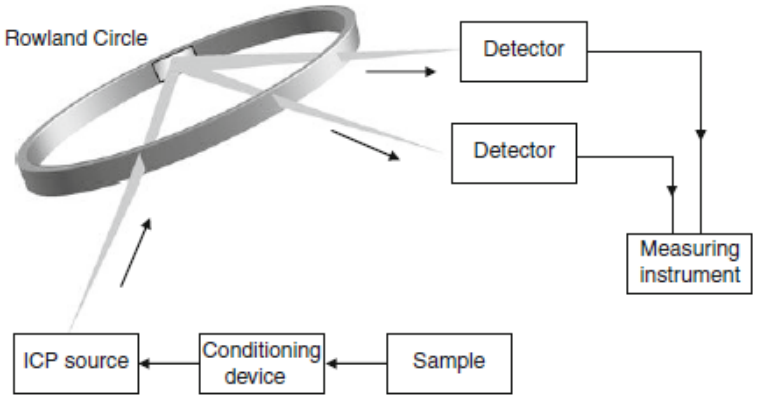

(a) Simultaneous Multichannel Detector

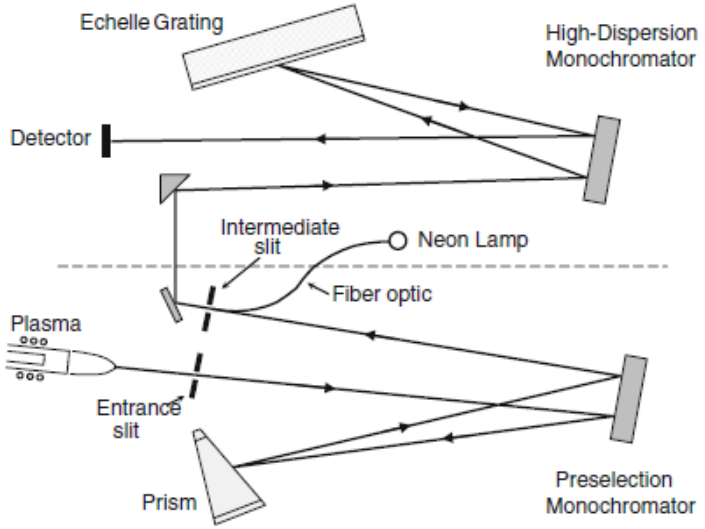

(b) Sequential Detector

Fig. 34.4 Simultaneous multichannel (a) and sequential detectors (b) ((a) Adapted from SKOOG. Principles of Instrumental Analysis, 5E. © 1998 Brooks/Cole, a part of Cengage Learning, Inc. Reproduced by permission. www.cengage.com/permissions (b) Image used with permission from PerkinElmer, Inc., Waltham, MA)

Optická emisní spektrometrie s indukčně vázaným plazmatem (ICP-OES)

Multiprvková analýza

Stanovení fosforu a dalších prvků (Fe, Cu, Pb, K, …)

Reakce pozůstatků s kovy

Strachotín

Langobardské pohřebiště

Vyloupený hrob č. 80

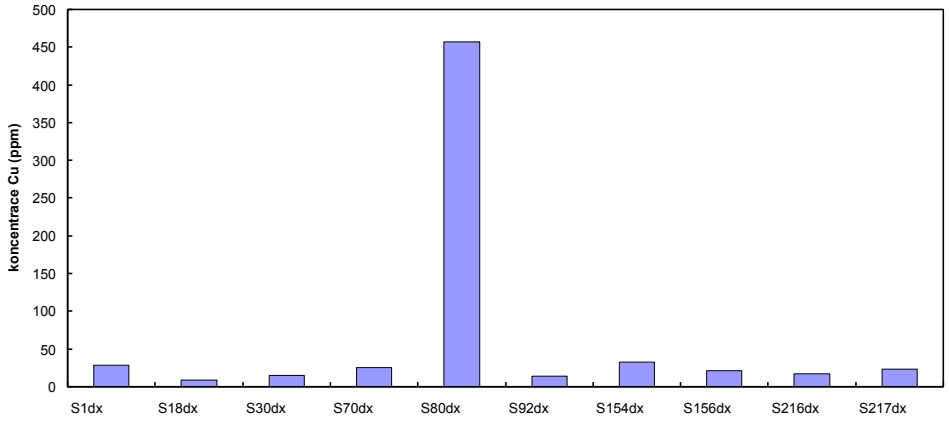

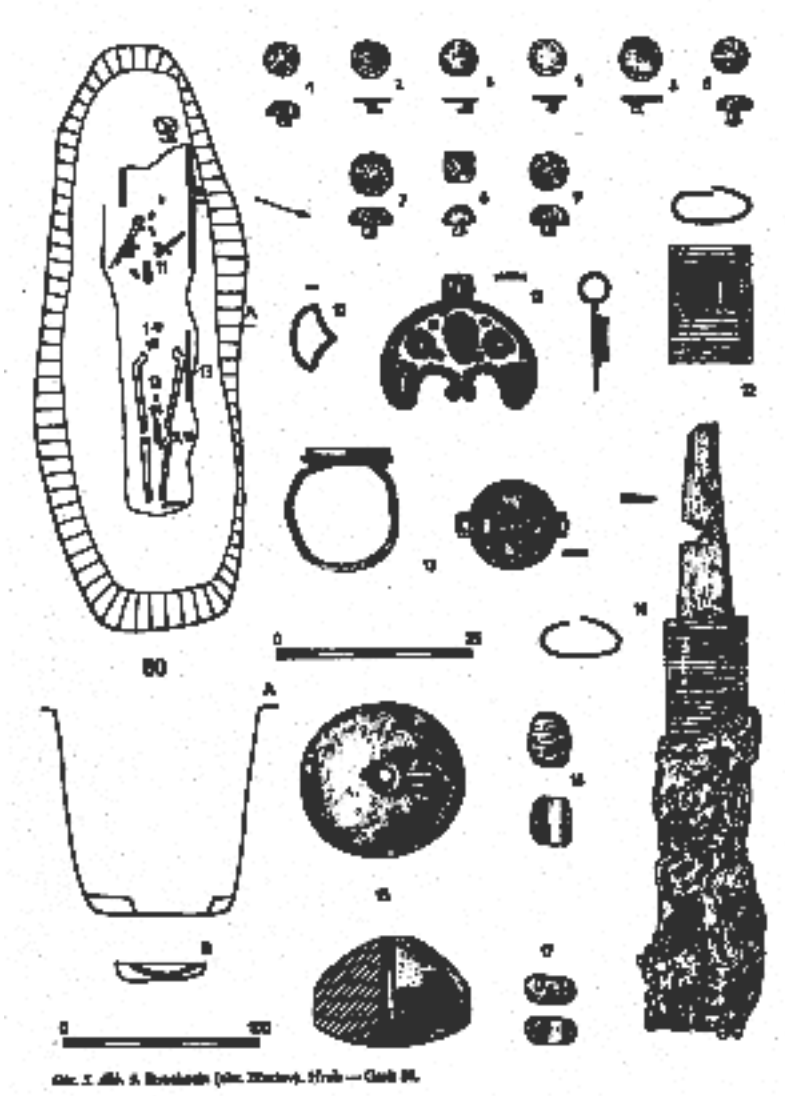

Spektrografie

Semikvantitativní

Semidestruktivní

Jiskra
El. oblouk

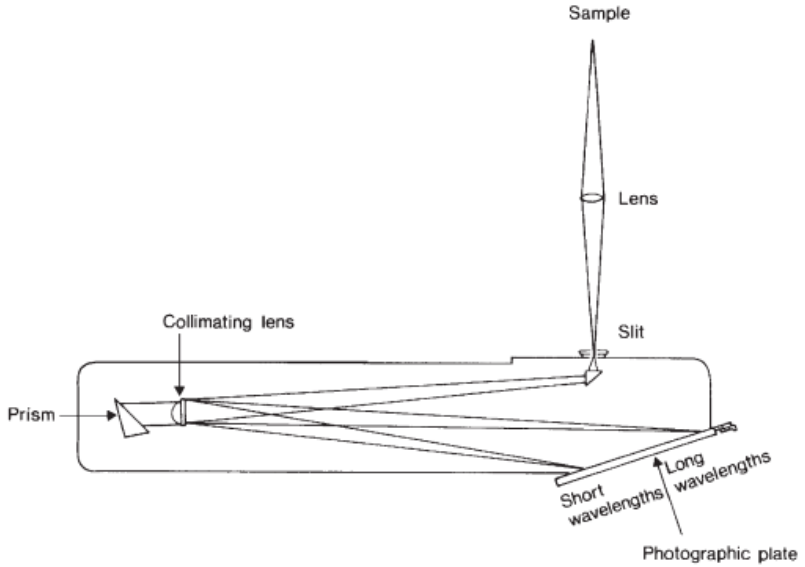

Figure 2.2 Schematic drawing of an optical emission spectrograph. Light from the sample is focused onto the input slit of the spectrograph and is then dispersed via a prism (or diffraction grating) and recorded on a photographic plate. (Adapted from Britton and Richards, 1969; Fig. 108, by permission of Thames and Hudson Ltd.)

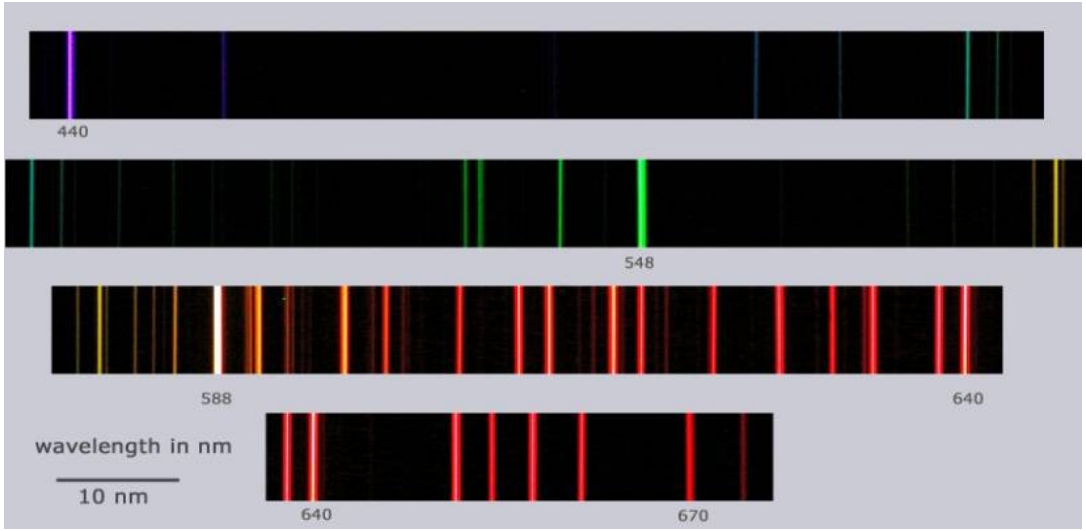

Emisní spektrometie s doutnavým výbojem (GD-OES)

Analýza povrchu

Nedestruktivní

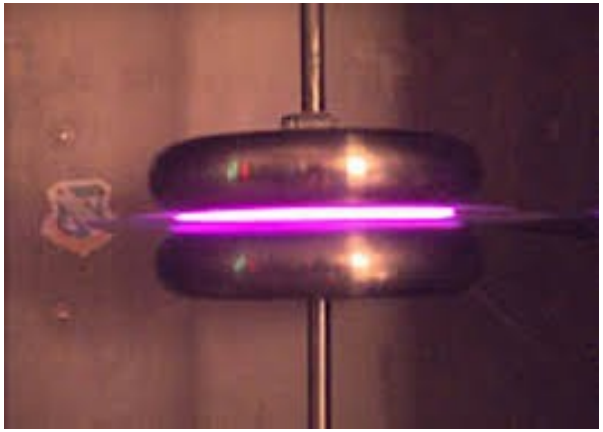

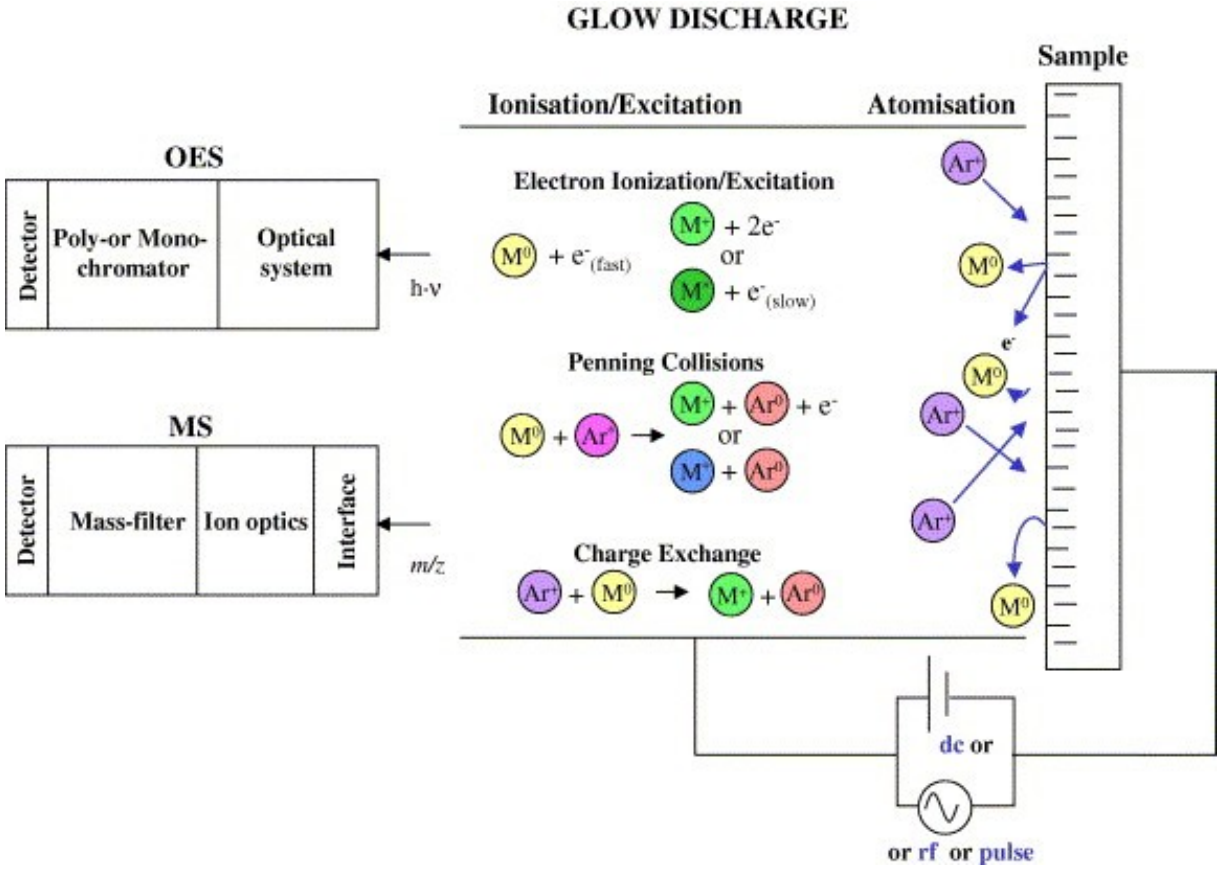

Hmotnostní spektrometrie s indukčně vázaným plazmatem

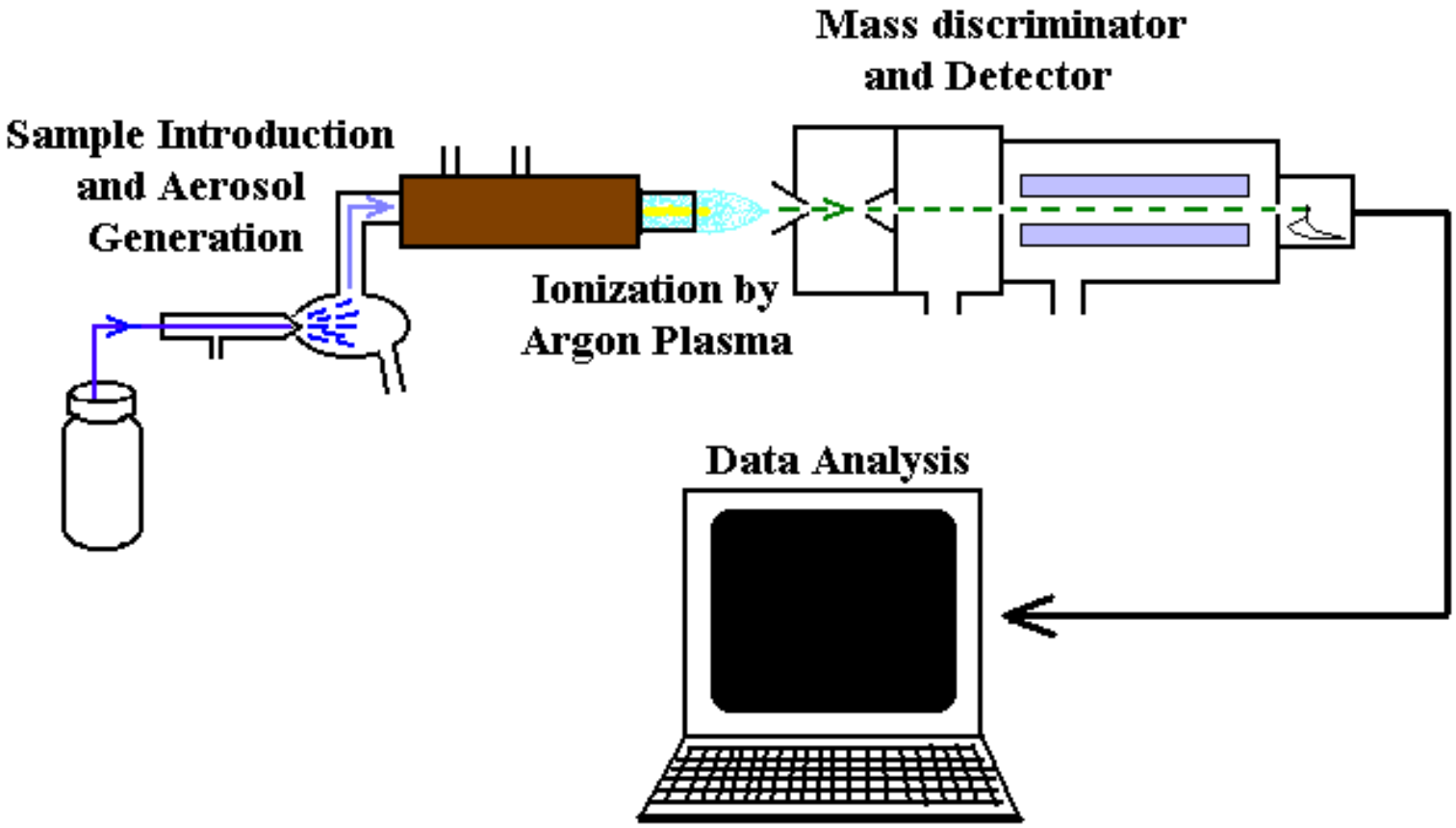

ICP-MS s laserovou ablací (LA-ICP-MS)

Nd:YAG

Excimer

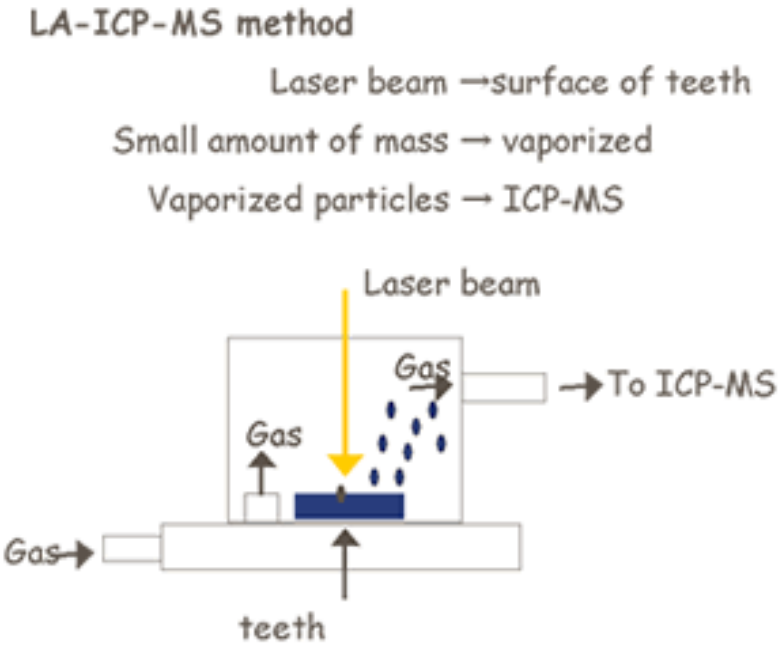

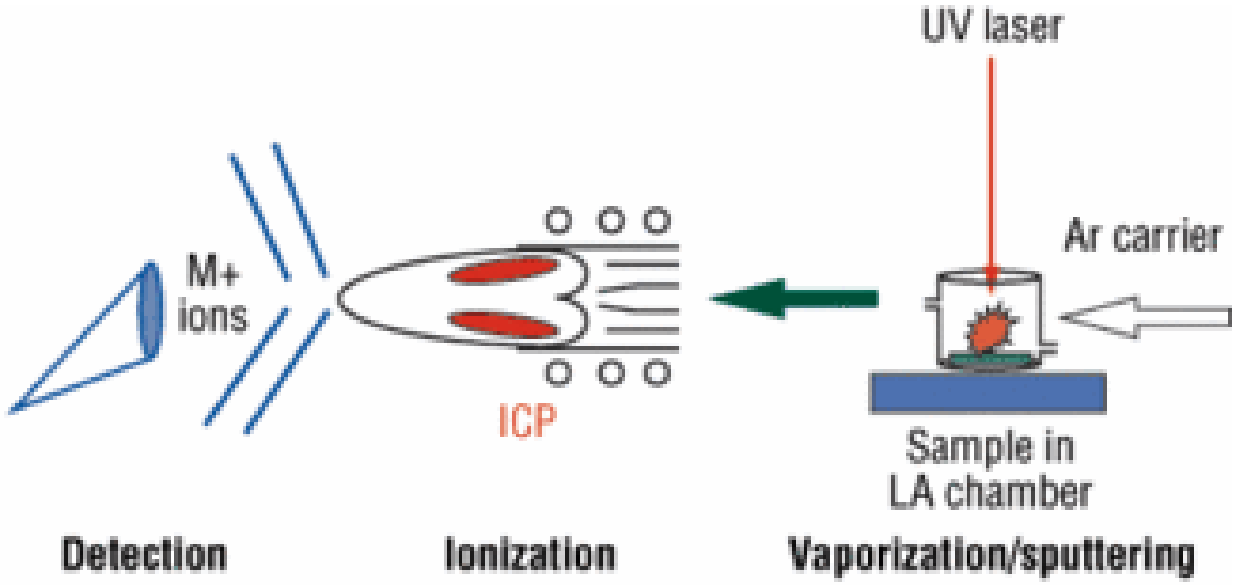

Provenience obsidiánu

Owens Valley,
vých. Kalifornie

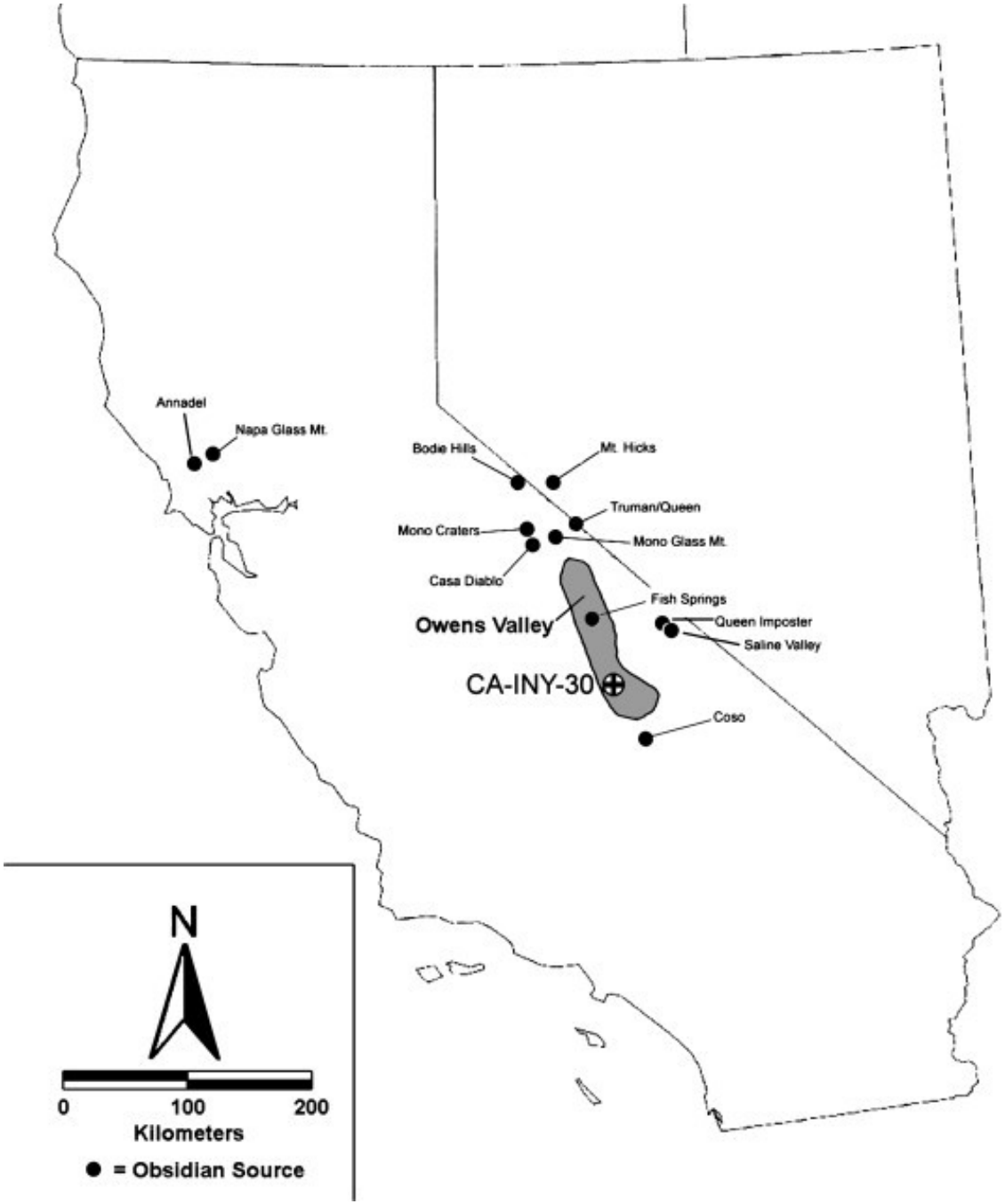

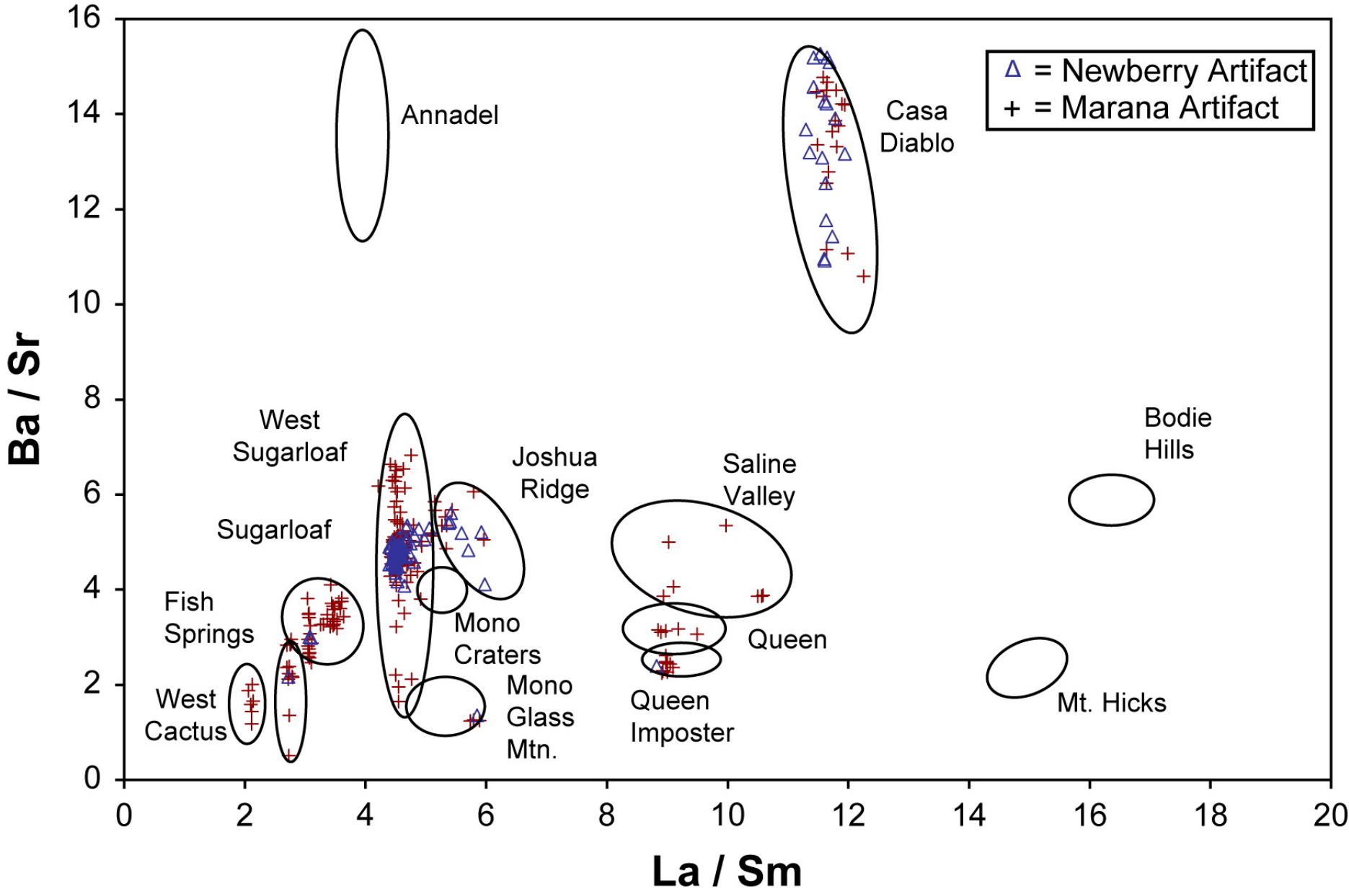
Ba / Sr
La / Sm
△ = Newberry Artifact
+ = Marana Artifact
Annadel
Casa Diablo
West Sugarloaf
Sugarloaf
Fish Springs
West Cactus
Joshua Ridge
Mono Craters
Mono Glass Mtn.
Saline Valley
Queen
Queen Imposter
Bodie Hills
Mt. Hicks
0
2
4
6
8
10
12
14
16
18
20

Provenience železa

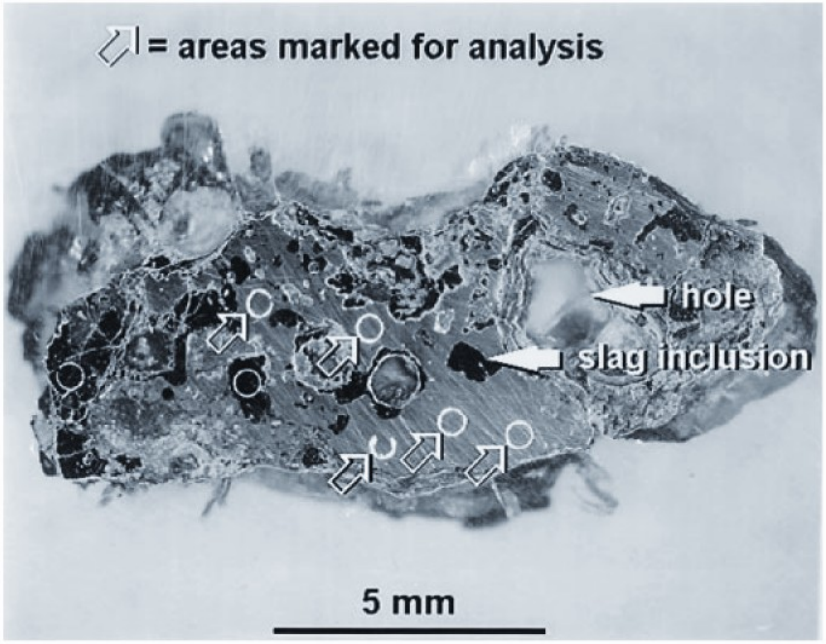

Fig. 1 Optical microscopy view of a cross-section of an iron bloom fragment embedded in a synthetic resin

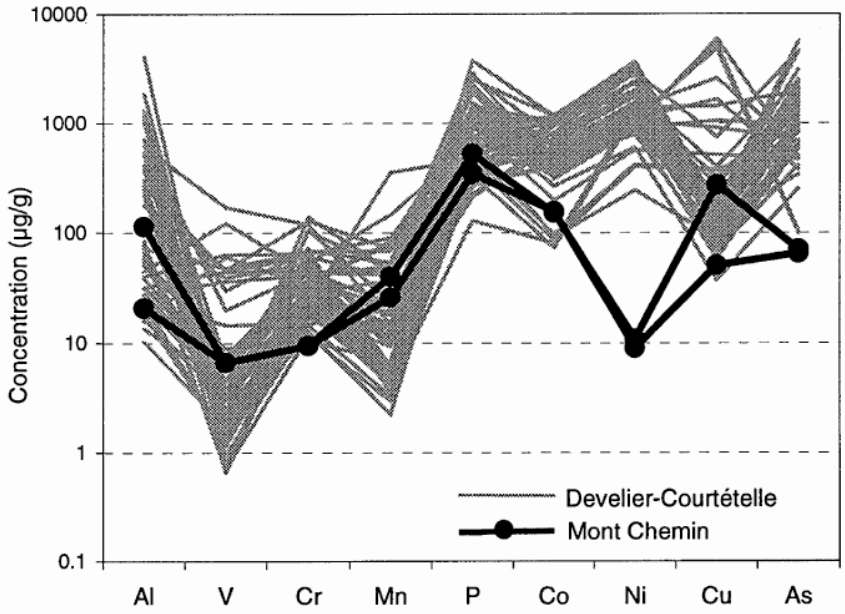

Fig. 9 Concentration profile for an iron bloom sample from Mont Chemin (Switzerland), compared to the concentration profiles in the Develier-Courtételle samples, showing low values for Ni in the Mont-Chemin sample

MC LA-ICP-MS

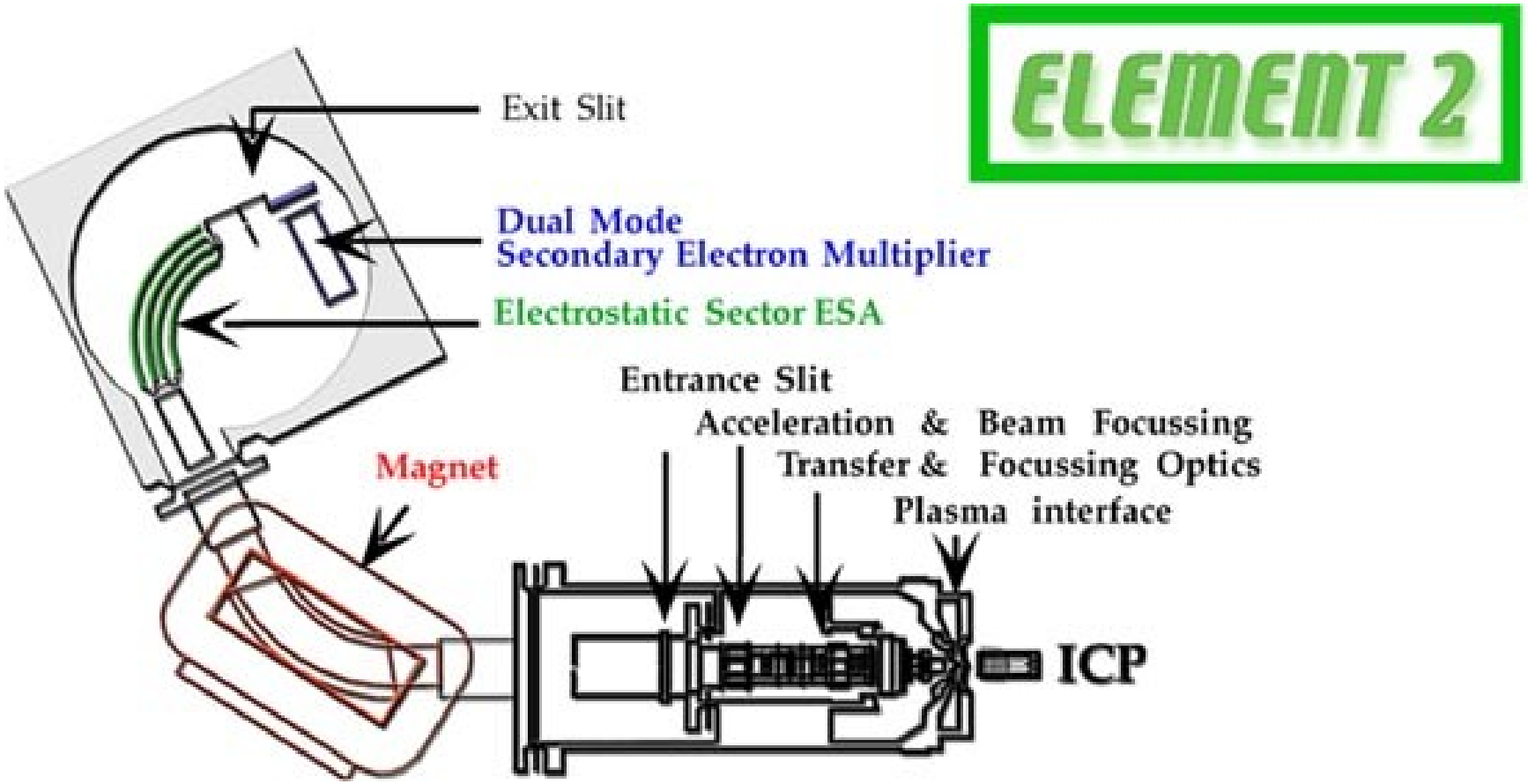
ELEMENT 2
Exit Slit
Dual Mode
Secondary Electron Multiplier
Electrostatic Sector ESA
Entrance Slit
Acceleration & Beam Focussing
Transfer & Focussing Optics
Plasma interface
Magnet
ICP

IUPAC Periodic Table of the Isotopes

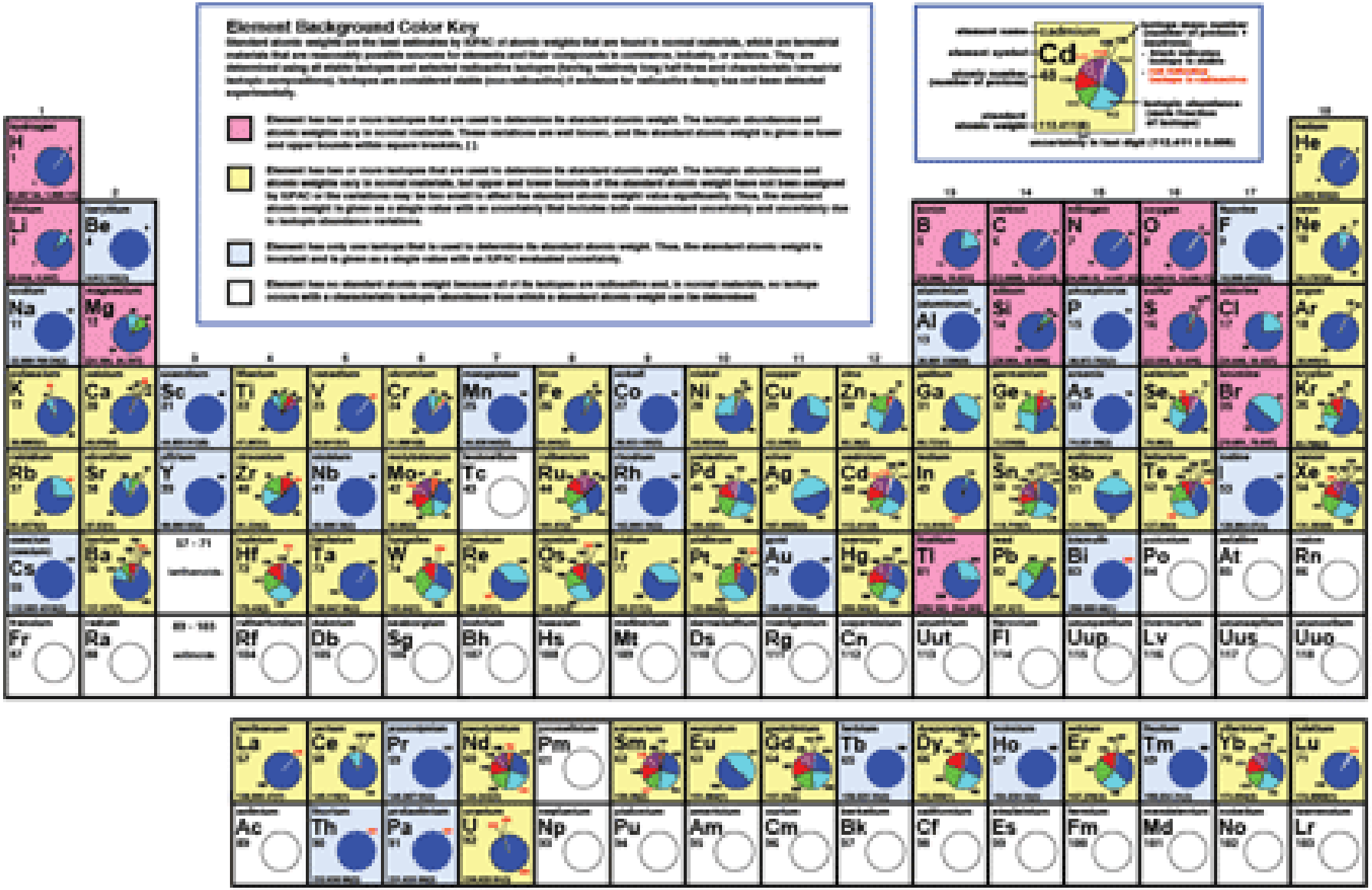

Analýza izotopových poměrů

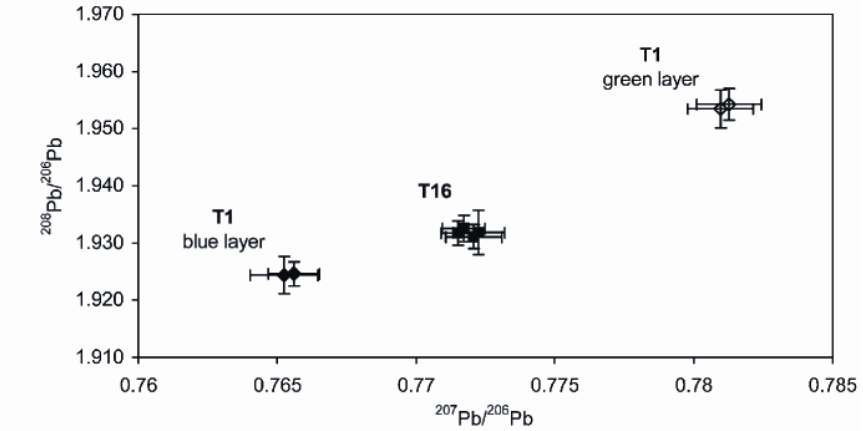

Fig. 2 Lead isotope ratio distribution of the two iridescent Art Nouveau glasses. Glass T1 consists of two layers of approximately equal thickness (coloured green and blue, respectively). Error bars represent total combined uncertainties ($k = 1$).

Sklo „Art nouveau“

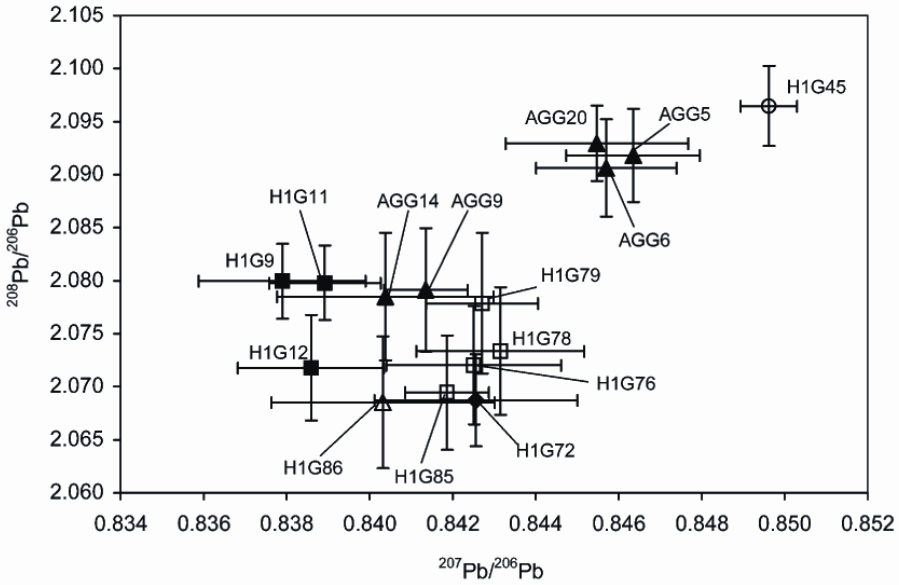

Fig. 3 Lead isotope ratios of Ephesos glass samples after external mass bias correction *via* the NIST SRM 610 glass reference material. Error bars represent total combined uncertainties ($k = 1$). For sample description see Table 1.

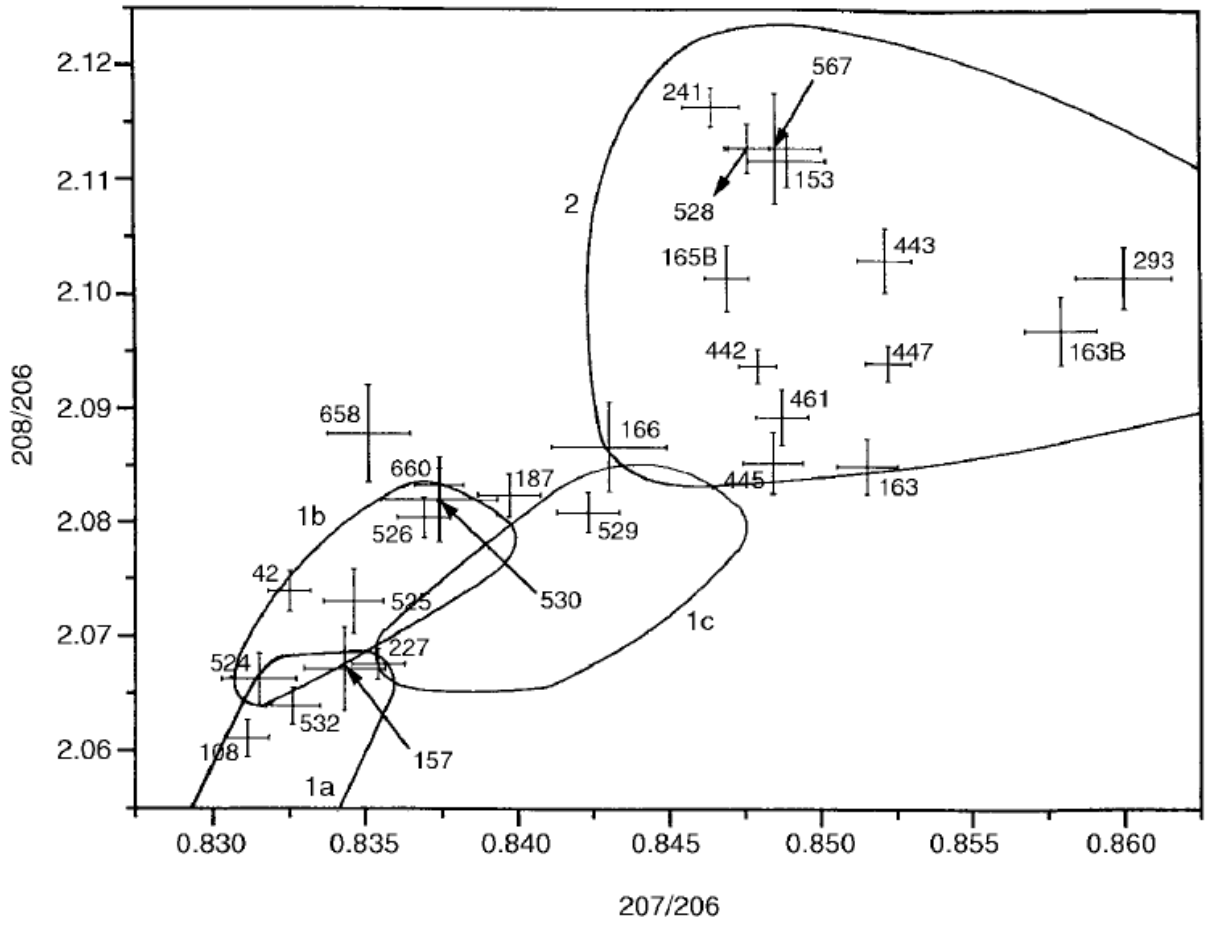

Fig. 1 $^{208}Pb/^{206}Pb$ *versus* $^{207}Pb/^{206}Pb$ plot for the statuettes investigated and for the possible lead ore sources: 1a, Laurion mining district (Greece); 1b, Kythnian mining district (Greece); 1c, Cypriotic field; and 2, British Islands field.

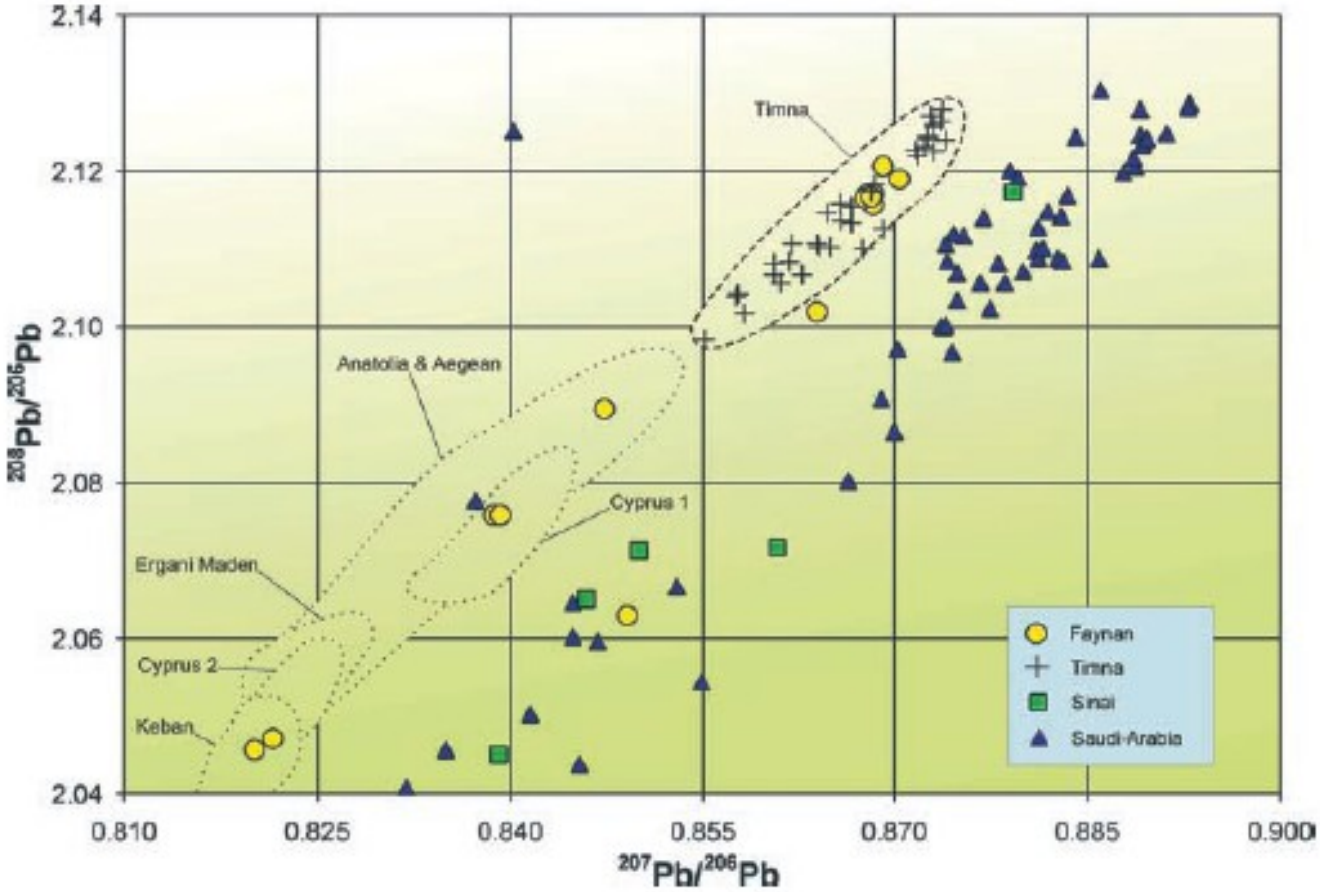

Fig. 4.14. Comparison of lead isotope abundance ratios of Arabah copper ores with ores from around the Eastern Mediterranean and the Arabian Shield. Evidence of ancient mining and smelting is known from Anatolia, the Aegean and from Cyprus (Stos-Gale 1993; Pernicka 1995) but is missing in detail from the Arabian Shield. The graph shows that the main copper mineralizations in the Arabah are among the oldest geological ages. Notice that the "Faynan/Timna field" contains only the data from the DLS and the Amir/Avrona Formation! Similarly old copper ores also occur in Saudi Arabia (Stacey et al. 1980; Bokhari and Kramers 1982; Brill and Barnes 1988) and on the Sinai Peninsula (Hauptmann et al. 1999; Segal et al. 2000)

Laser Induced Breakdown Spectroscopy

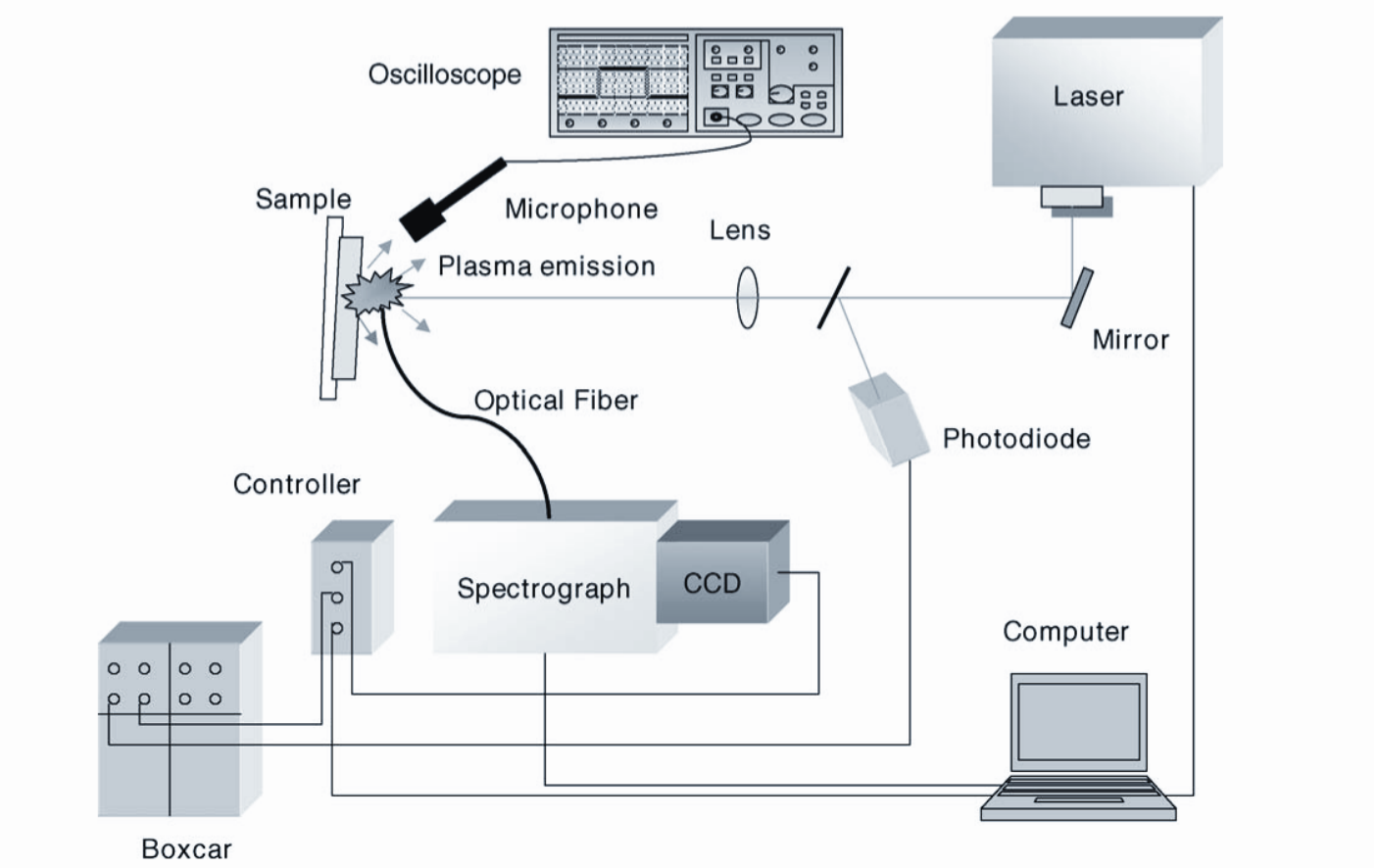

Schematic diagram of the experimental set-up used for the LIBS experiments and for the photoacoustic measurements.

LIBS

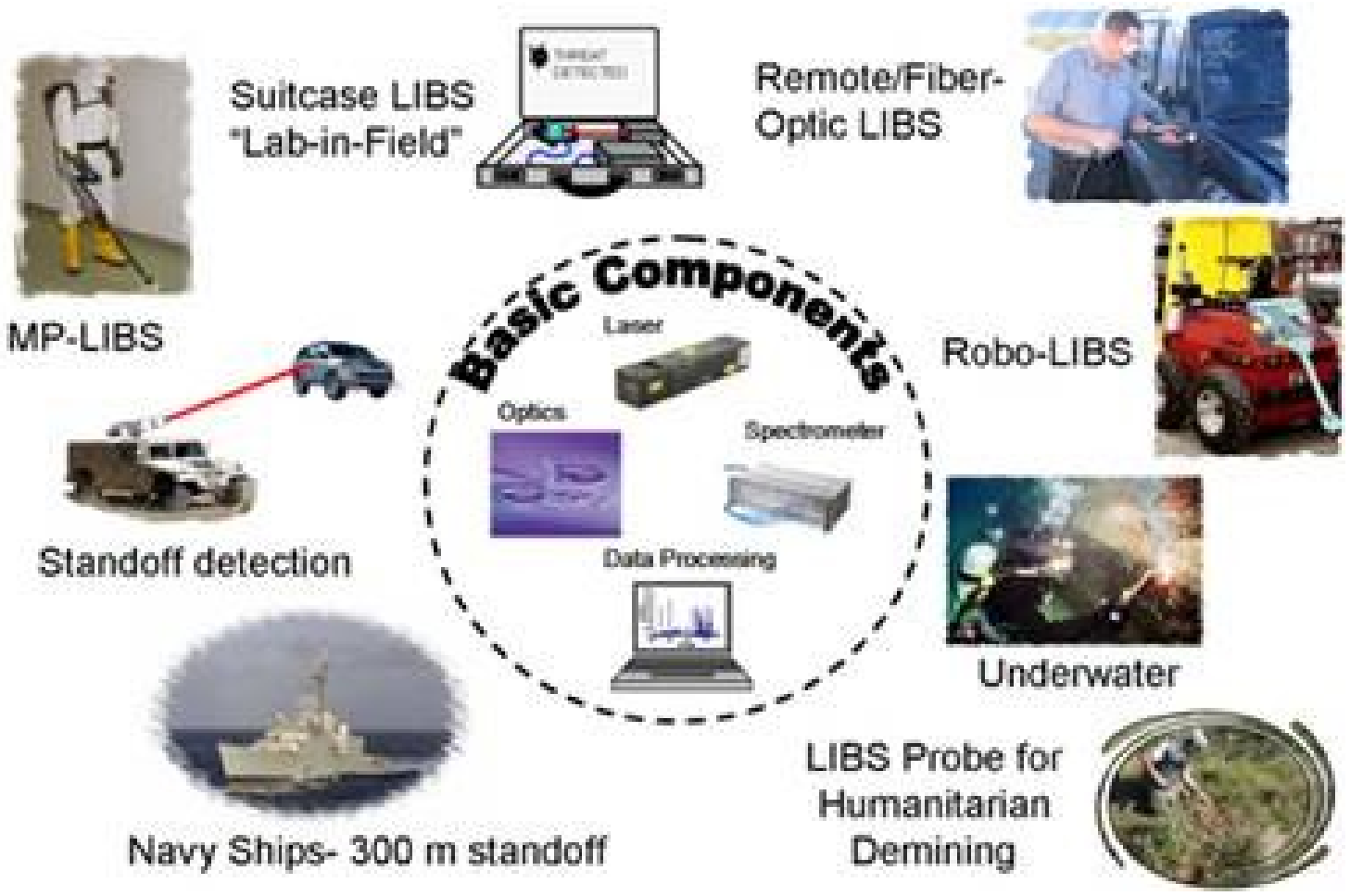
Suitcase LIBS
"Lab-in-Field"
Remote/Fiber-
Optic LIBS
MP-LIBS
Basic Components
Laser
Optics
Spectrometer
Data Processing
Robo-LIBS
Standoff detection
Underwater
Navy Ships- 300 m standoff
LIBS Probe for
Humanitarian
Demining

LIBS

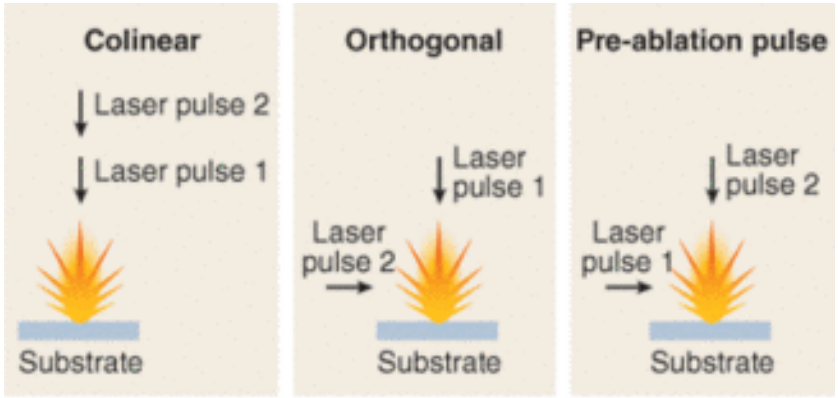

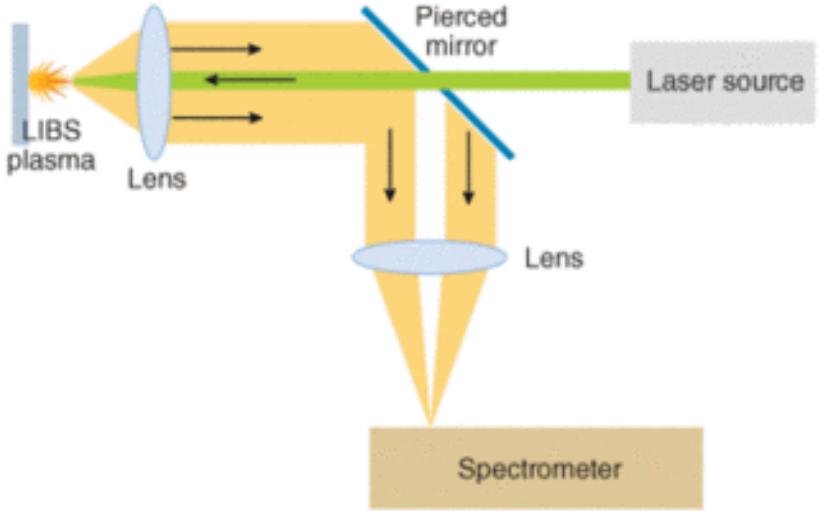

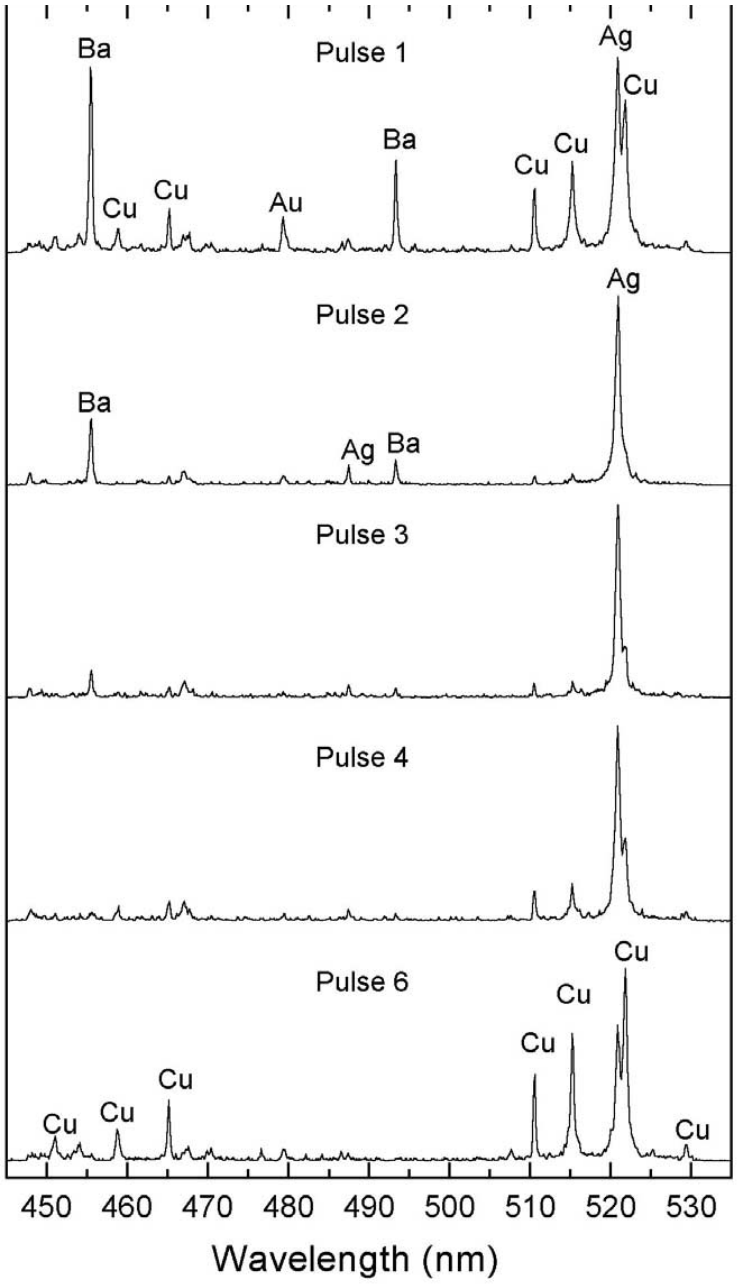

Daguerrotypie, 19. stol.

LIBS

Molekulové pásy →

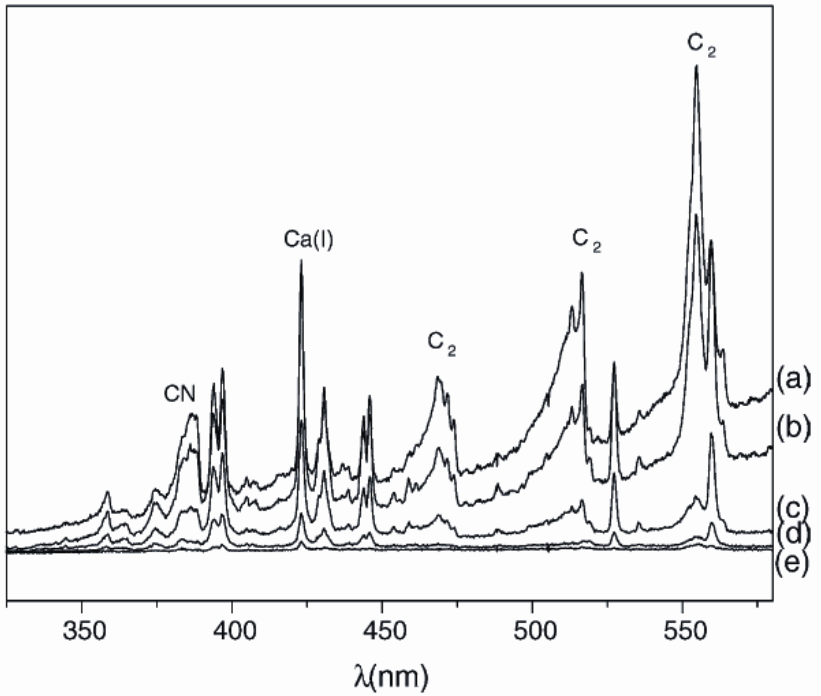

Fig. 6. Evolution of LIBS spectrum with the number of pulses during the removal of black paint on wood: (a) pulse 1, (b) pulse 2, (c) pulse 4, (d) pulse 7 and (e) pulse 9. Irradiation wavelength: 308 nm.

Spojení s Ramanovou spektrometrií

Monitoring odstraňování starých nátěrů

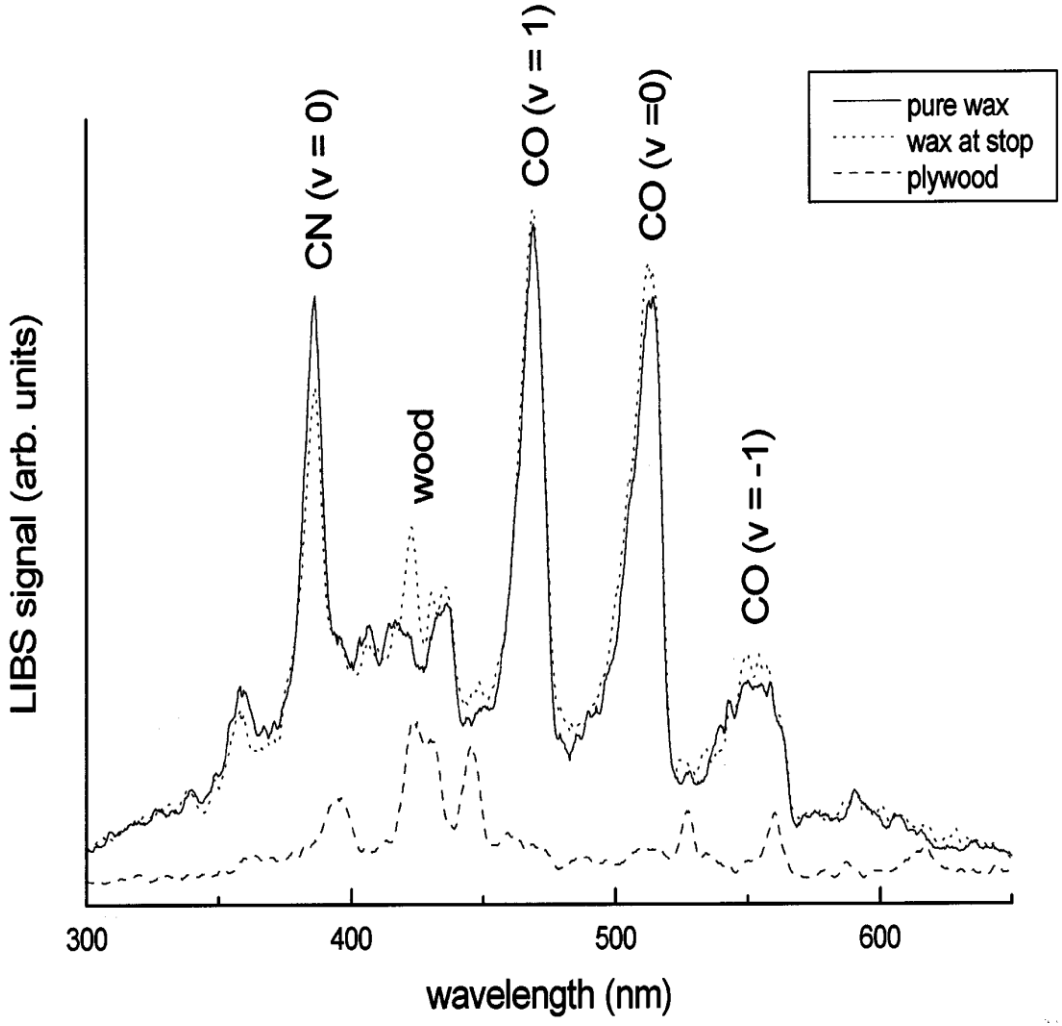

Odstraňování vosku z pláten nebo dřeva (překližka) je časově náročné. Proces lze snadno automatizovat použitím laseru a detekce LIBS.

LIBS spektra vosku vykazují zřetelné pásy CO a CN. Po dosažení spodní vrstvy se objevuje pík 423 nm a čištění je ukončeno.

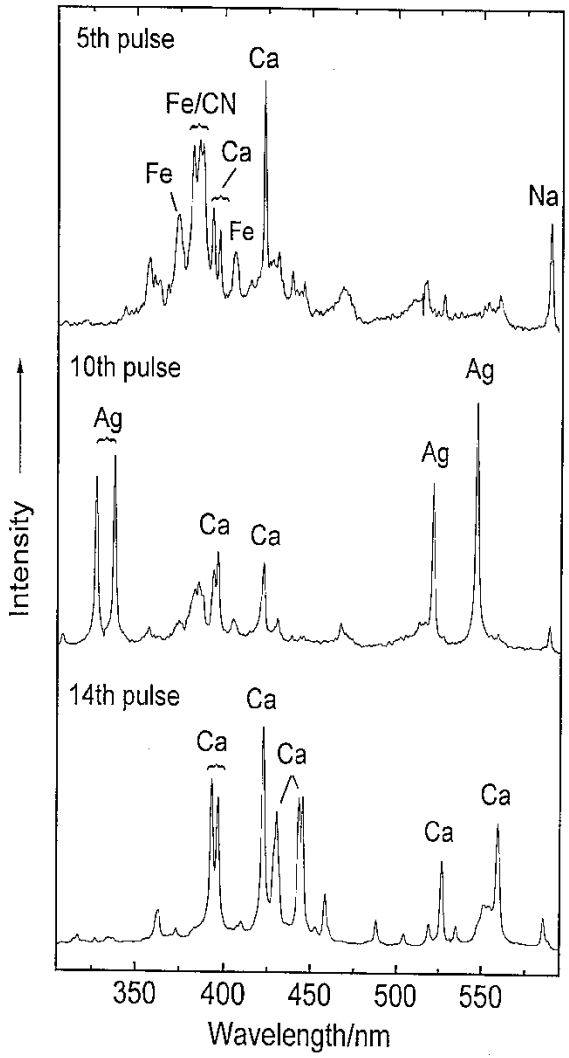

19th c. Russian icon of St. Nicholas.

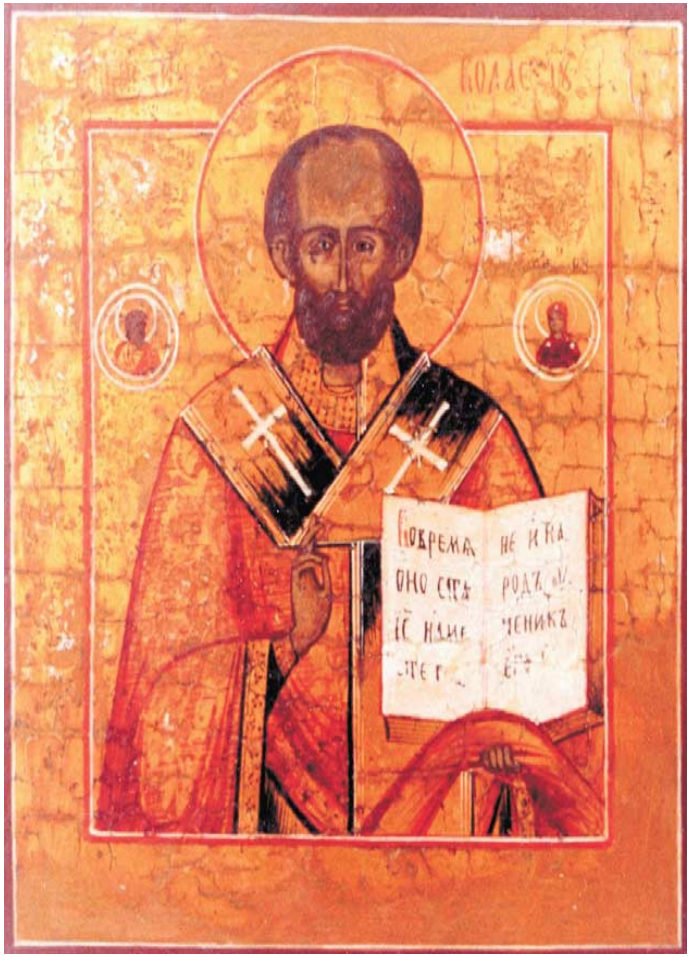

LIBS spektra malby (horní spektrum), stříbrné folie (střední spektrum) a podkladové vrstvy (dolní spektrum). Malba obsahuje pigment obsahující Fe (hnědý, pravděpodobně FeO), podklad je síran vápenatý.

Sledování restaurátorských zásahů

LIBS spektra originální malby a restaurovaných částí olejomalby.

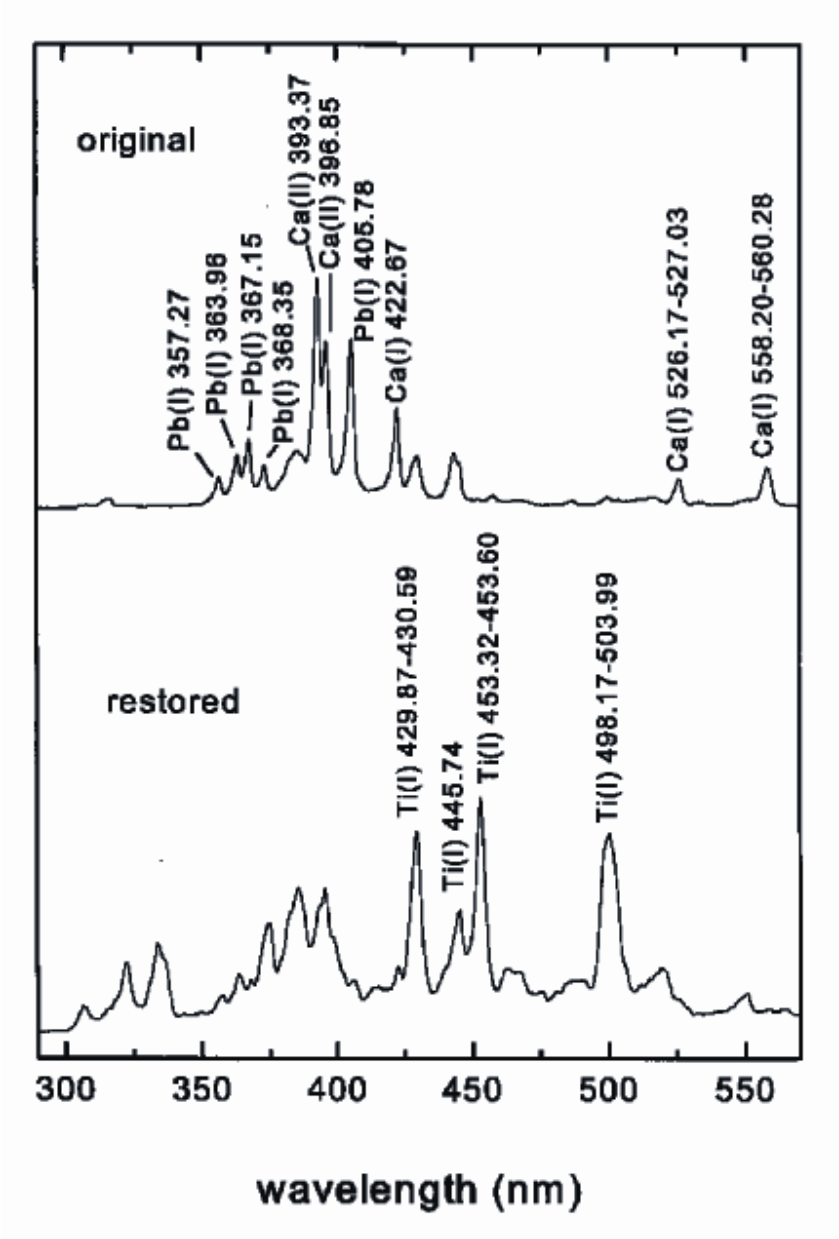

Keramika

Neolitická malovaná keramika (Itálie)

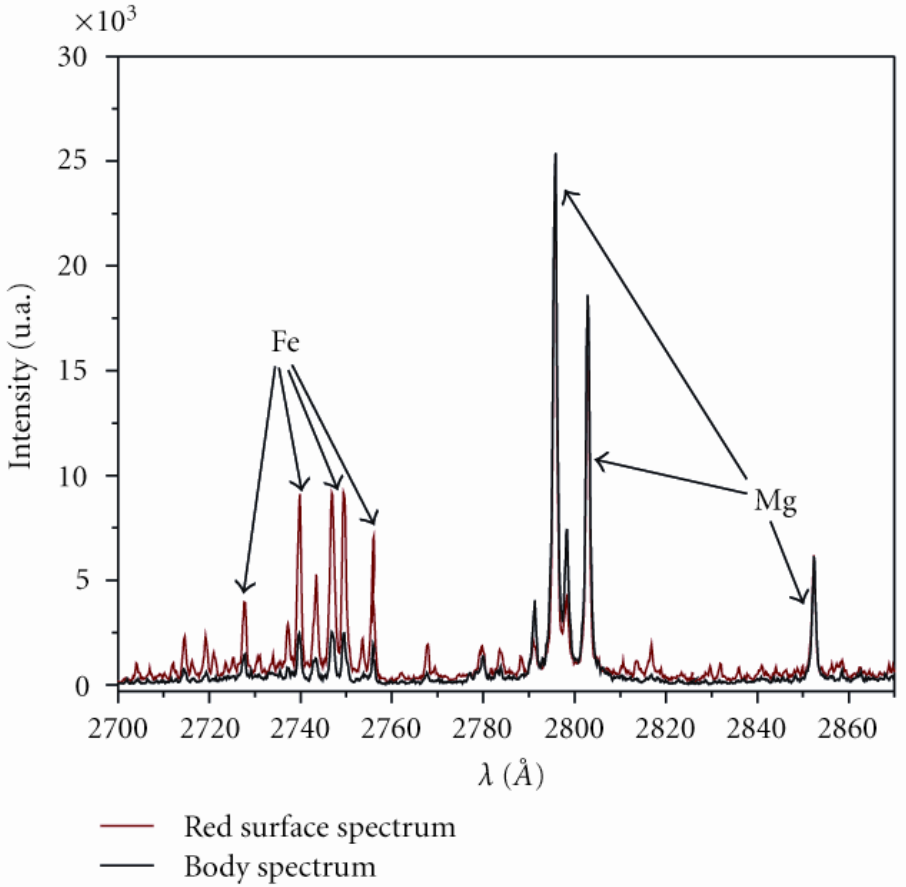

FIGURE 15: LIBS spectrum of the red region (TR13 sample).

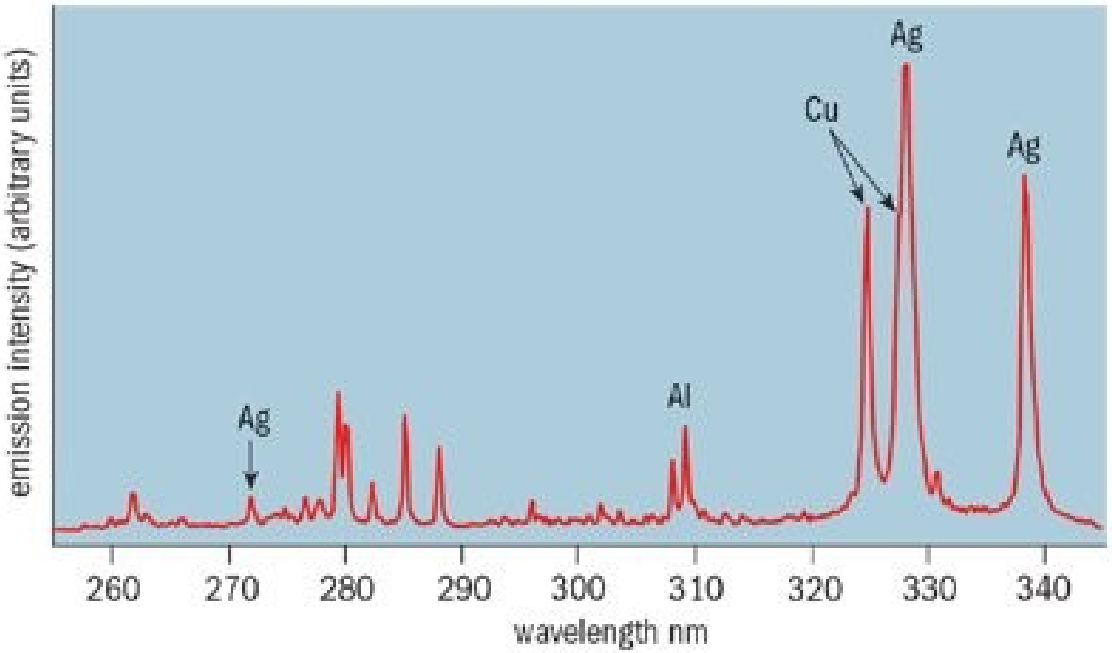

LIBS rukojeti dýky z ostrova Pseira (late-Minoan period, cca 1600 BC).

LIBS prokázal stopy stříbra na dřevěné rukojeti bronzové dýky (Nd:YAG laser, 1064 nm, 15 ns puls, 3-5 mJ per pulse).

Výrobní technologie bronzu

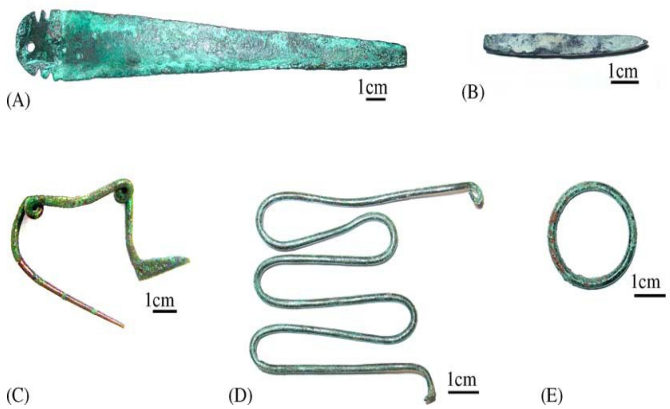

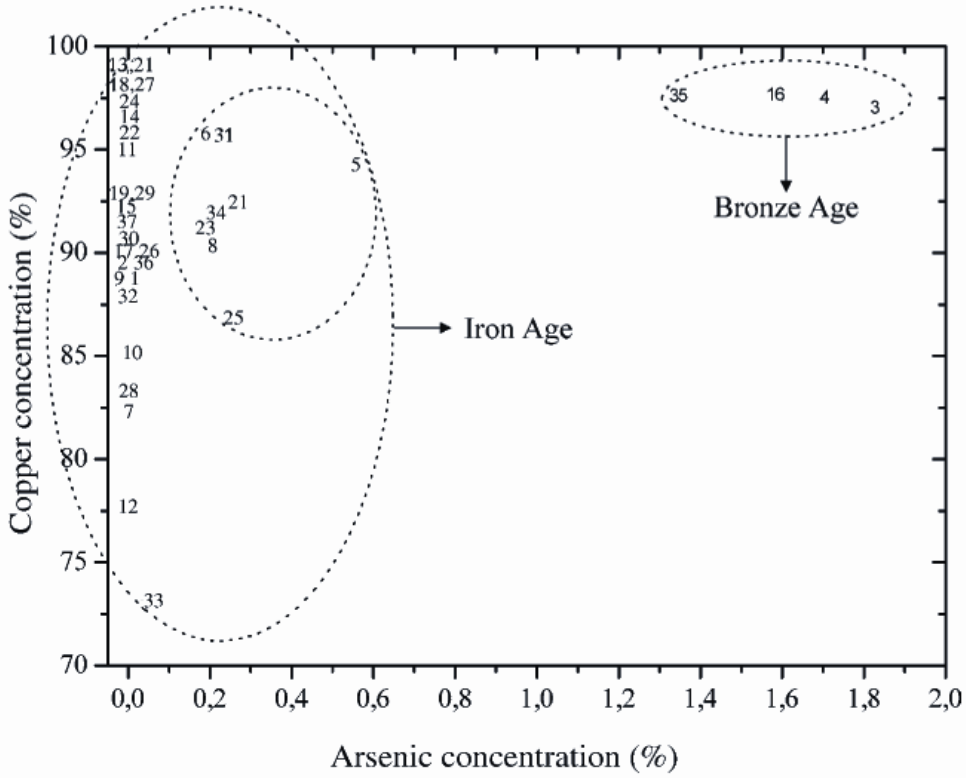

Fig. 7. Comparison of copper and arsenic concentration obtained by LIBS for the set of 37 archaeological samples.

Kosti a zuby

Obsah Mg a Ca v zubní tkáni poškozené kazem. Zvýšená koncentrace Mg zřetelně indikuje postižené partie.

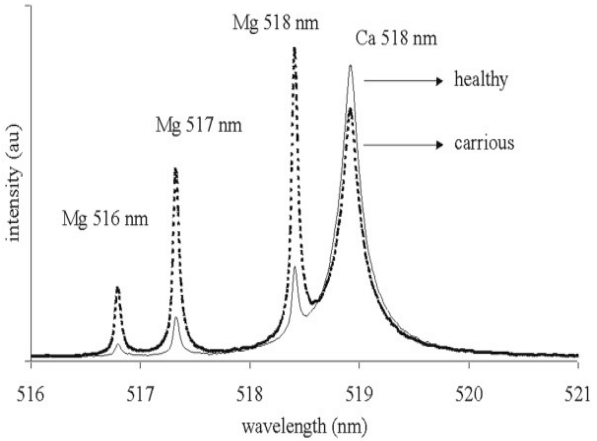

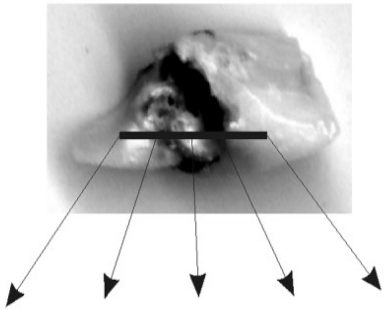

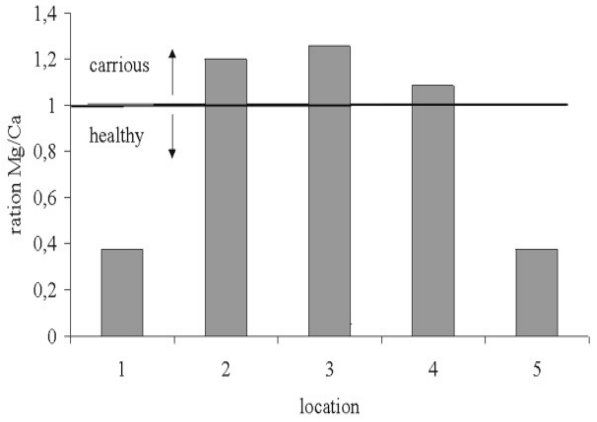

Čištění kamene

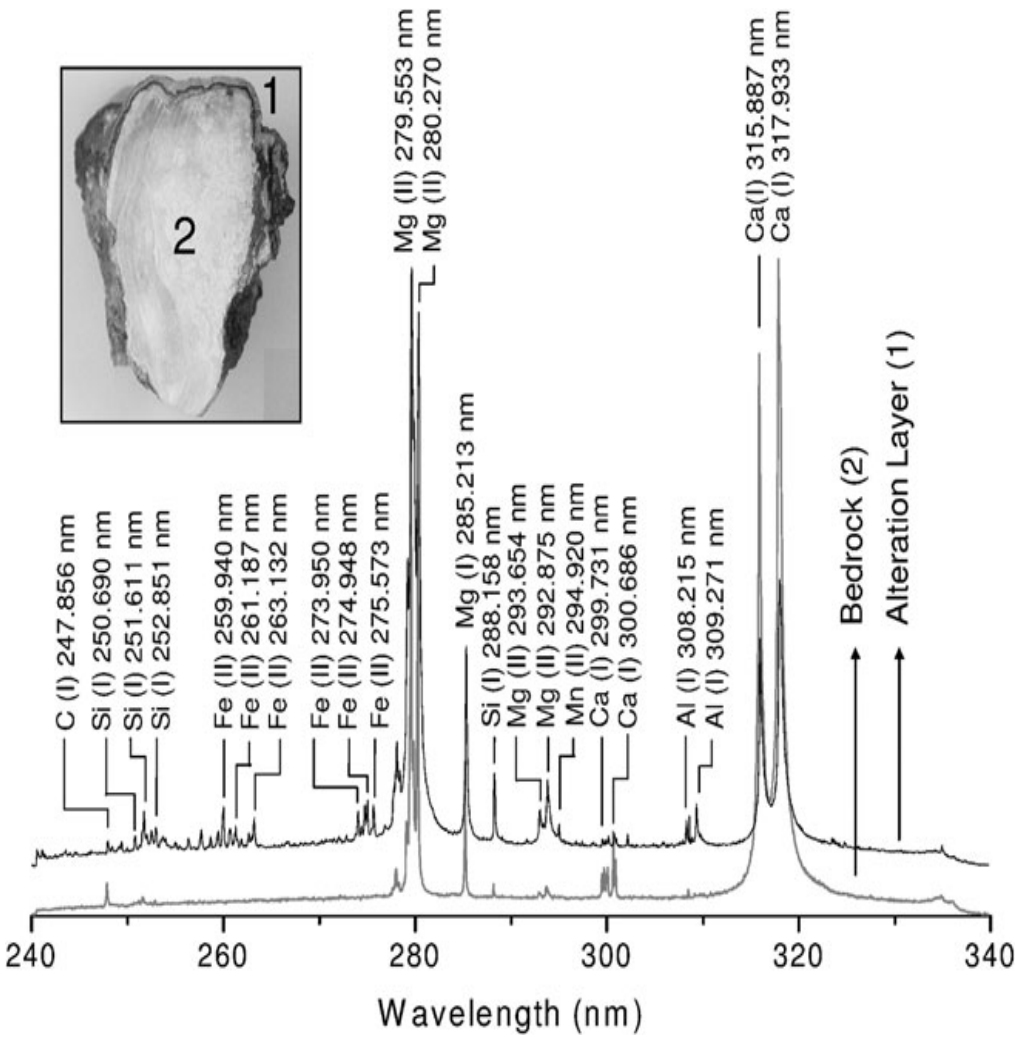

LIBS řezu krápníkem (znečištěný povrch)

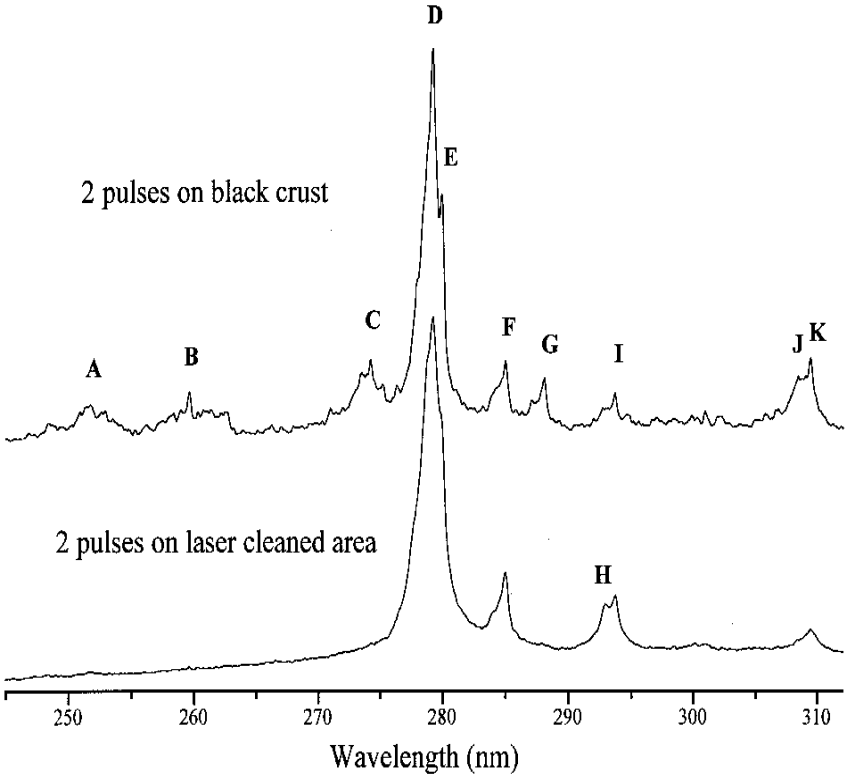

LIBS spectra in the spectral region from 245 to 310 nm obtained by two laser pulses each on the black crust and the laser-cleaned region.

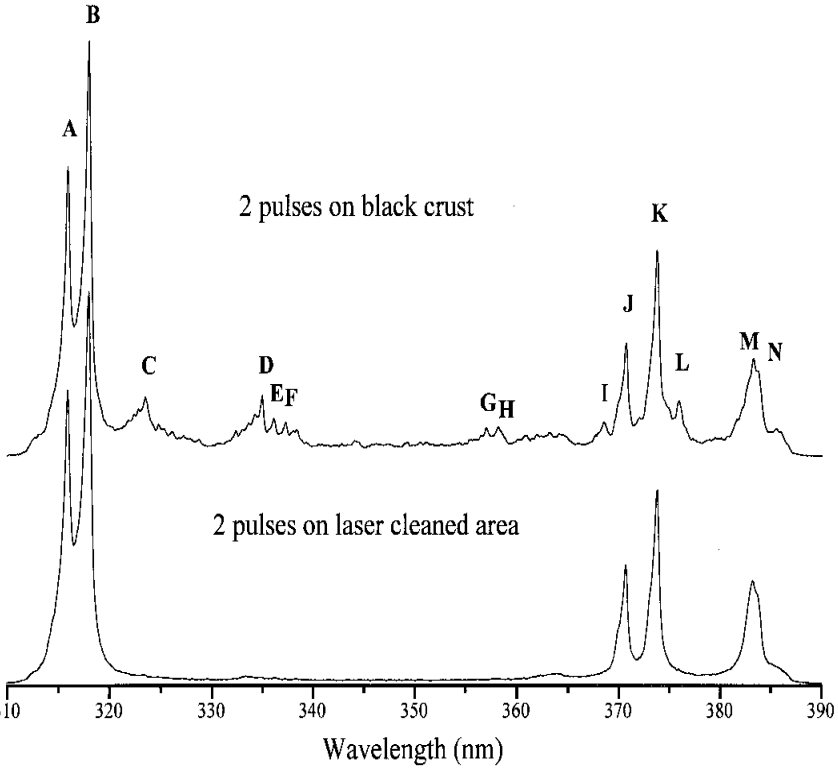

LIBS spectra in the spectral region from 310 to 385 nm obtained by two laser pulses each on the black crust and the laser-cleaned region.

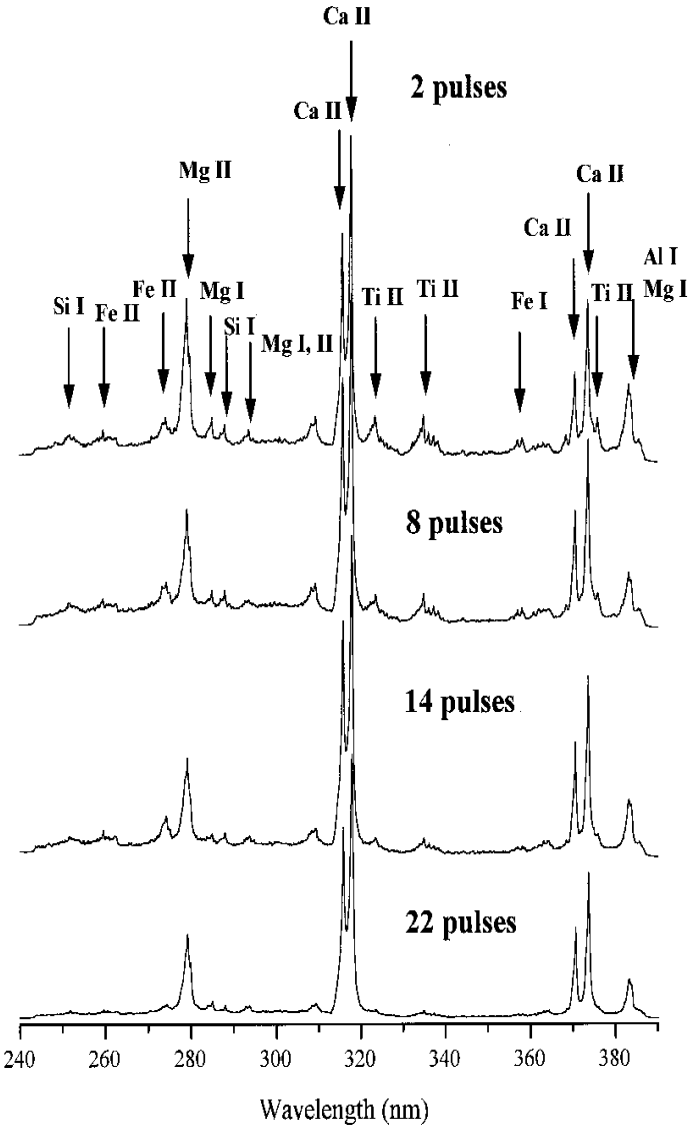

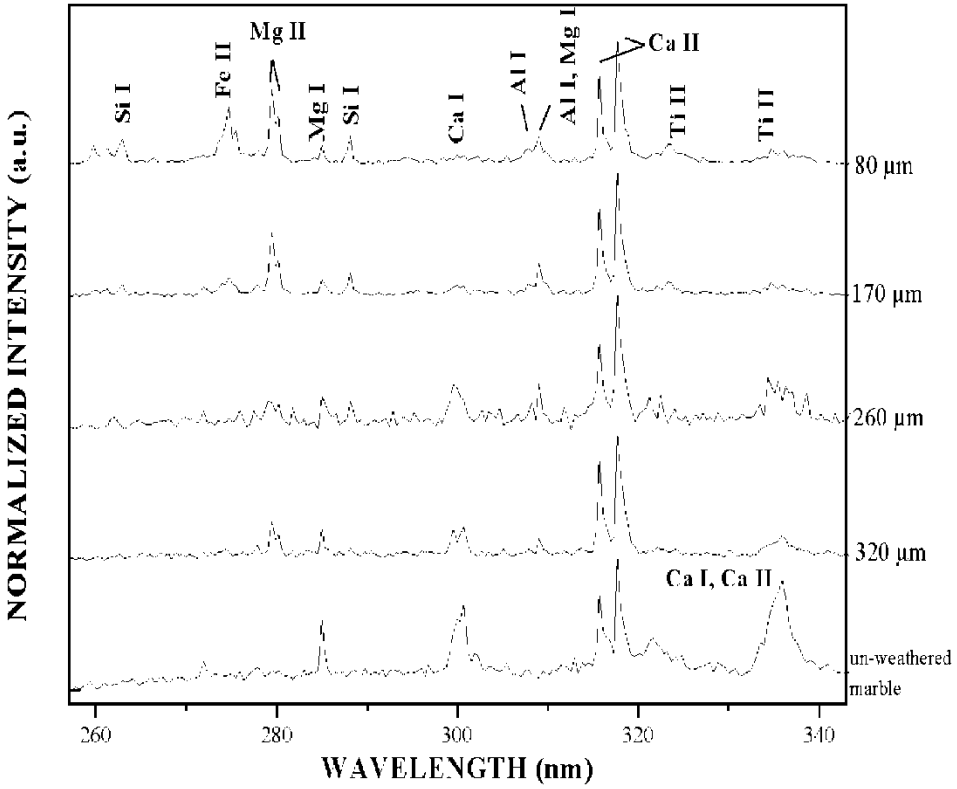

LIBS ablatovaného materiálu z různé hloubky dendritické krusty (Pentelický mramor, normalizováno na Ca II 317.93 nm).

LIBS spektra 2., 8., 14. a 22. pulsu, ablace tmavé krusty.

Malaga

Analýza portálu katedrály.

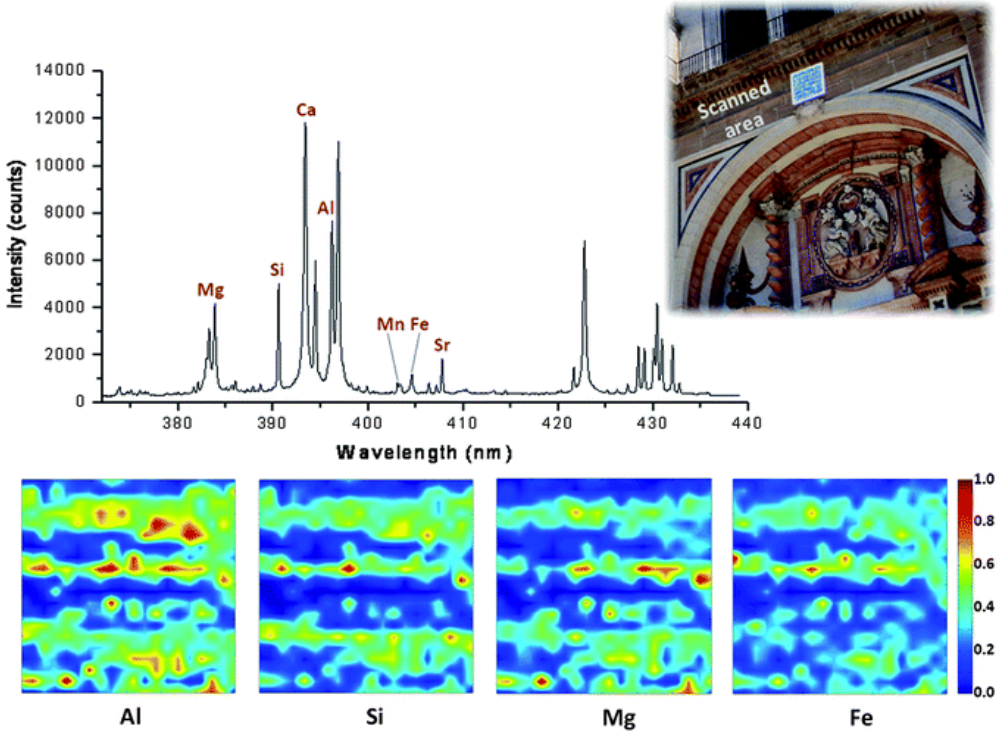

Autenticita výrobků z korálu

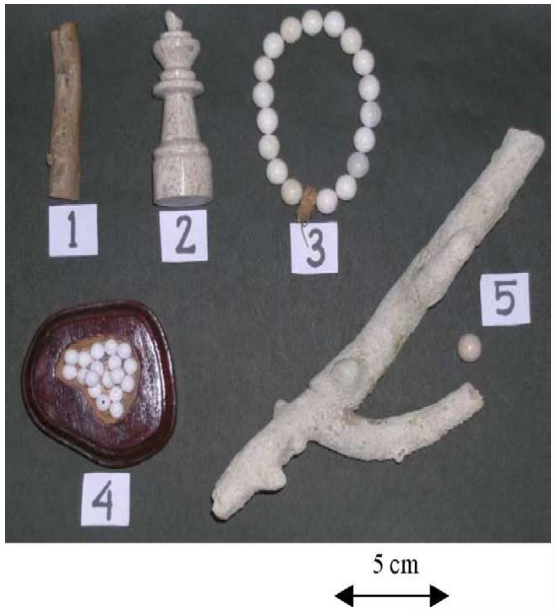

korál vs. vápenec

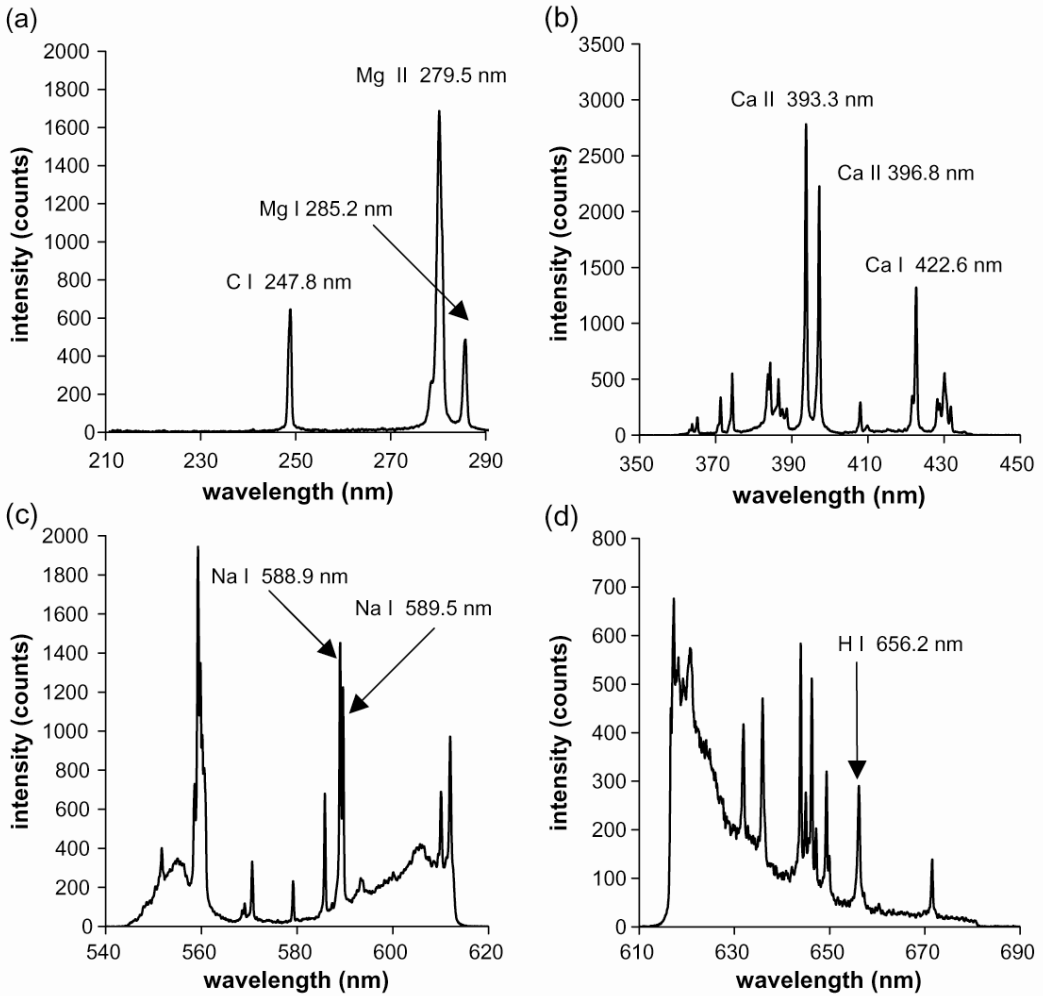

Fig. 5. Emission spectra of a fresh white coral sample in a low pressure plasma of 1.3 kPa in the wavelength region between (a) 220 and 290 nm, (b) 370 and 440 nm, (c) 550 and 620 nm and (d) 620 and 680 nm.

Stand-off LIBS

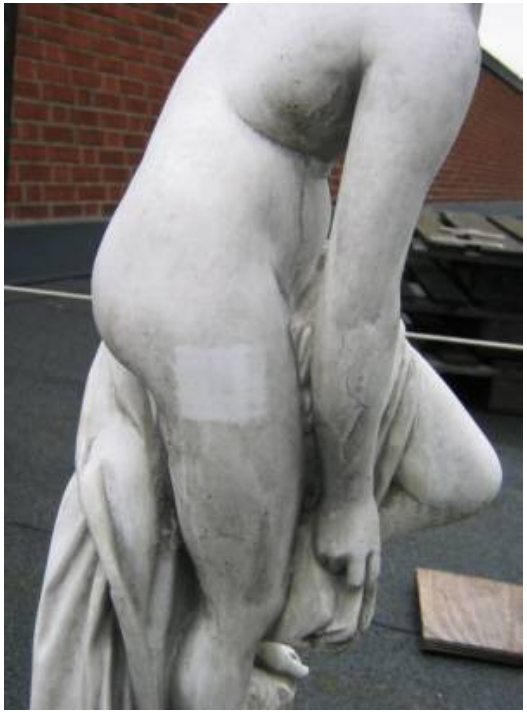

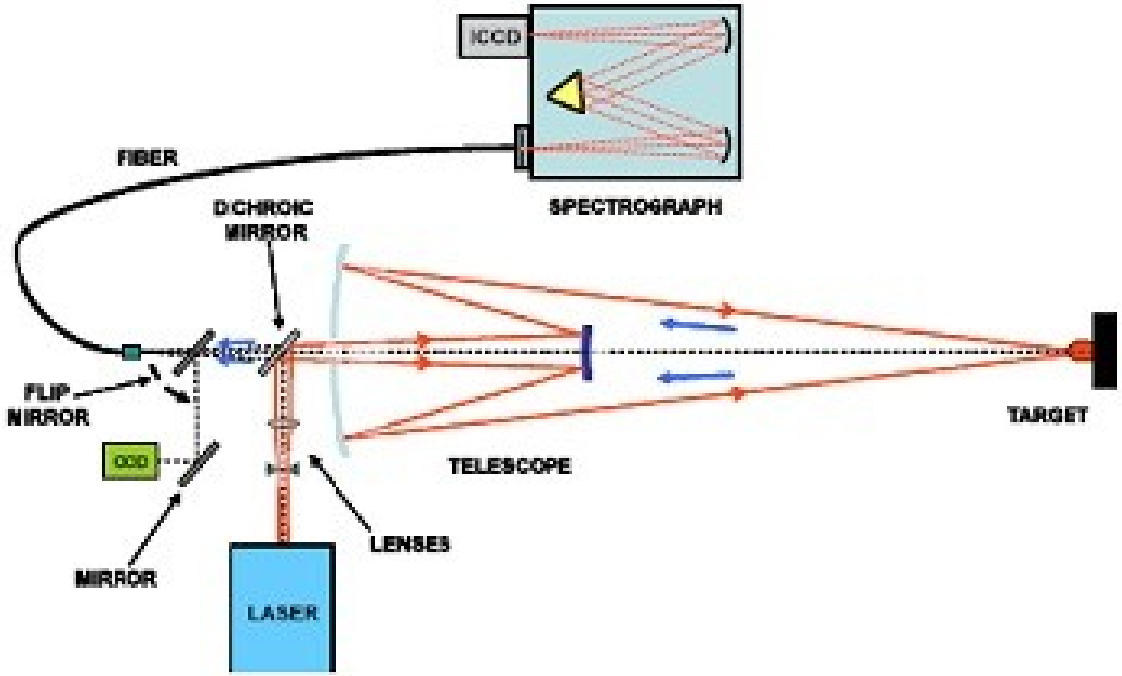

ChemCam

Stand-off LIBS

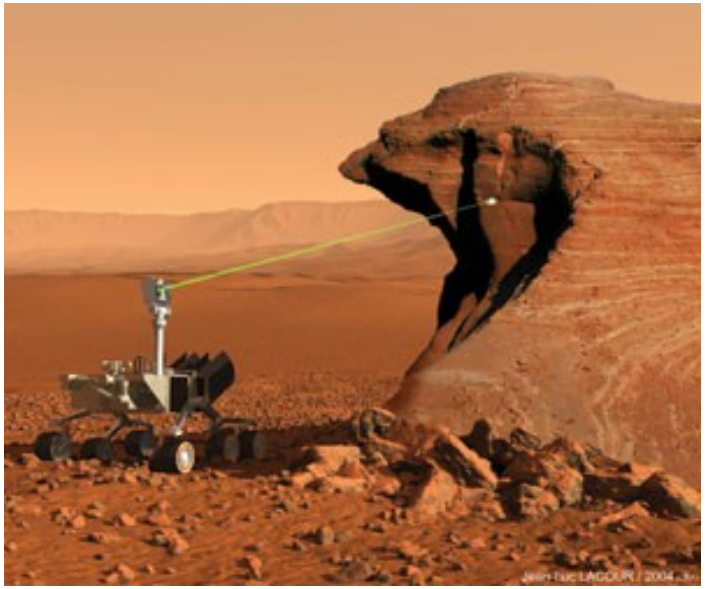

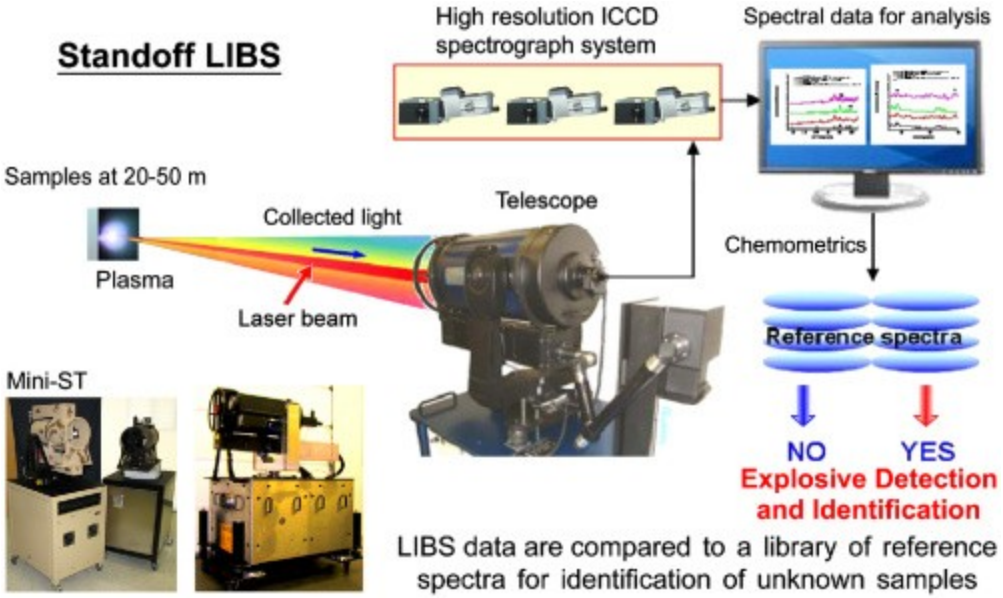

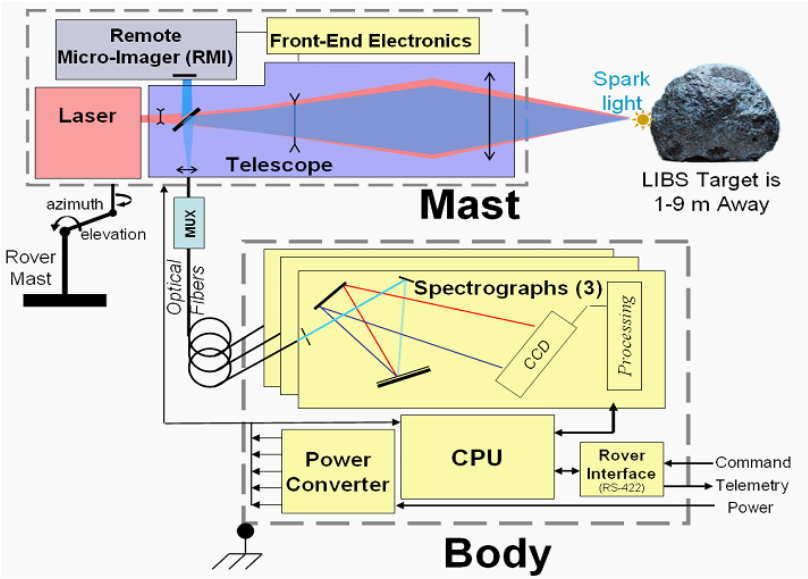

remote LIBS

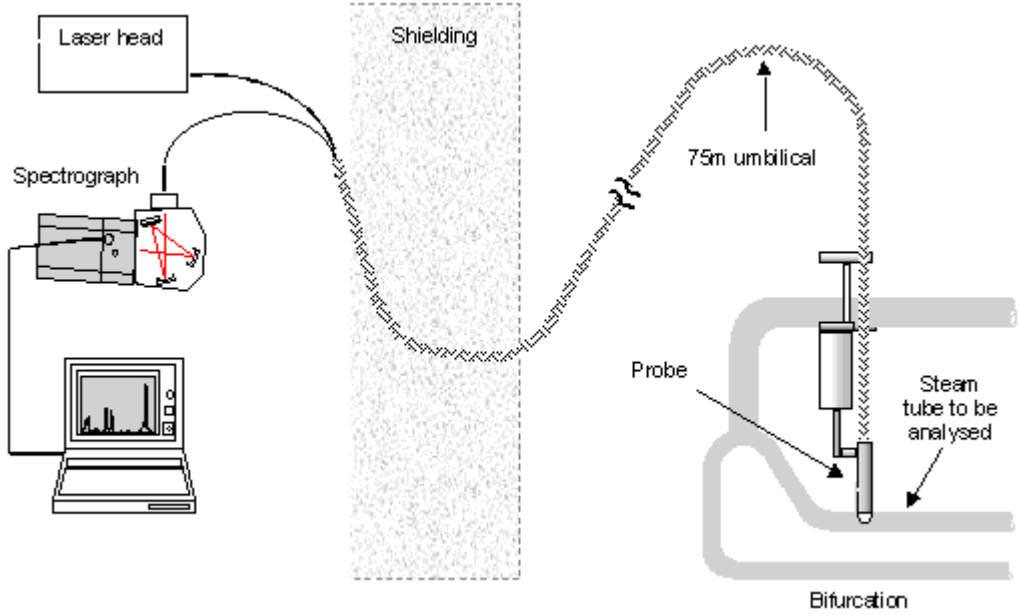

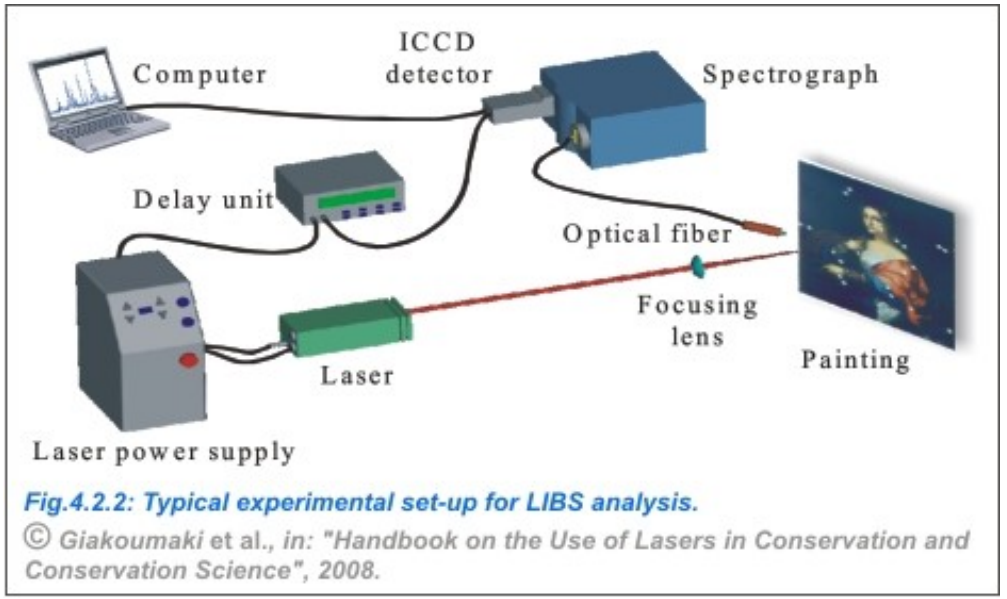

Fig.4.2.2: Typical experimental set-up for LIBS analysis.

© *Giakoumaki* et al., *in: "Handbook on the Use of Lasers in Conservation and Conservation Science", 2008.*

Emisní spektrometrie laserem indukovaného plazmatu (LIBS)

Prvková analýza

Neutronová aktivační analýza

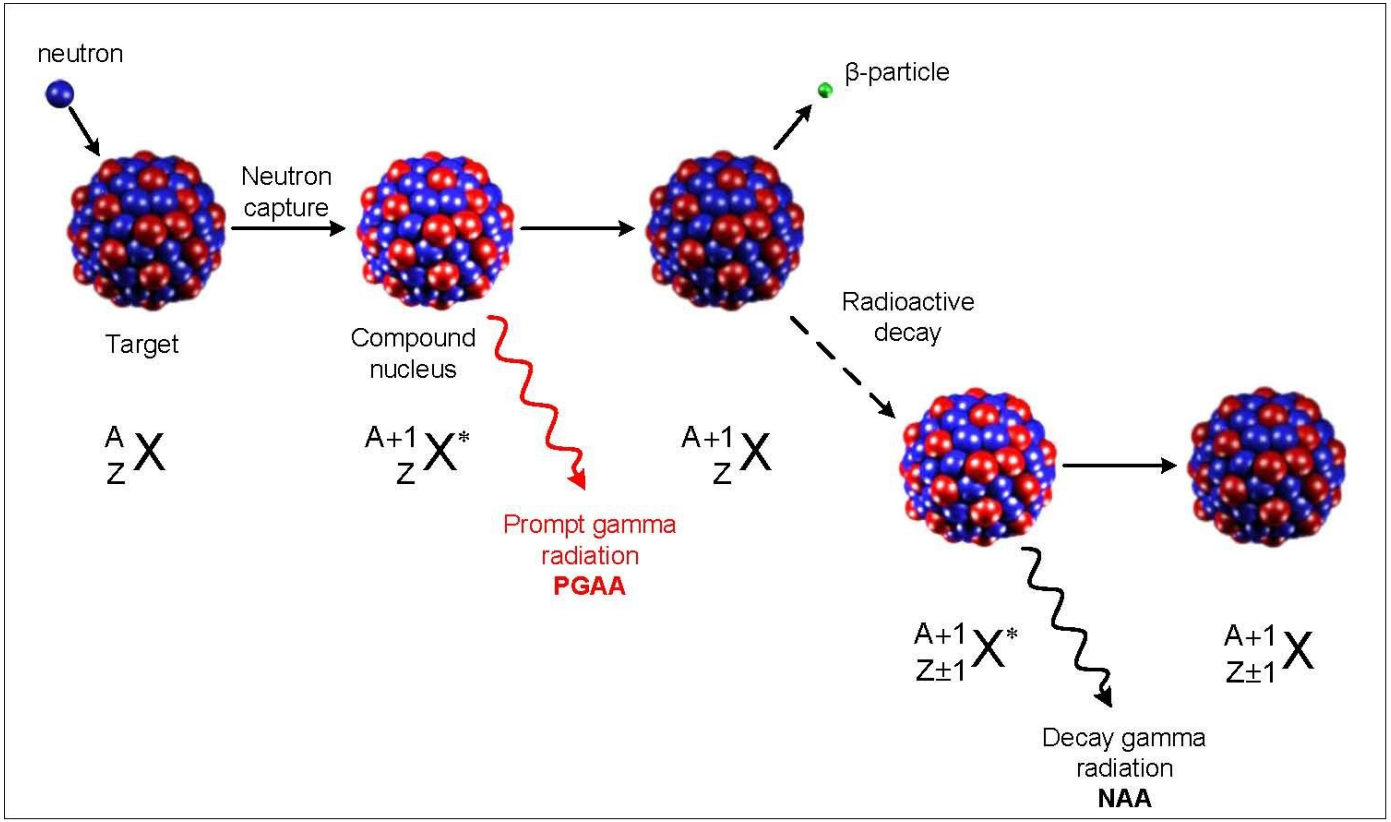

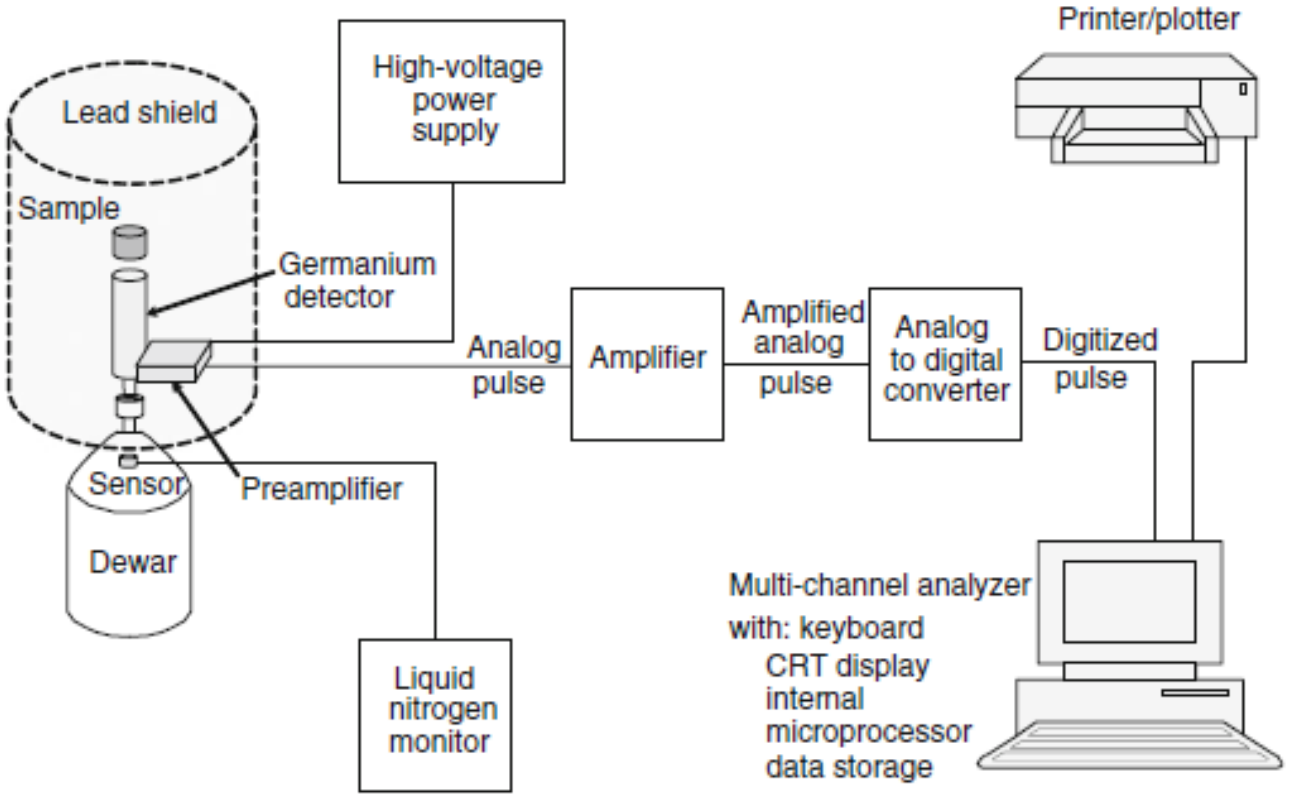

Fig. 32.1 Germanium–lithium detector (From SKOOG. Principles of Instrumental Analysis, 5E. © 1998 Brooks/Cole, a part of Cengage Learning, Inc. Reproduced by permission. www.cengage.com/permissions)

Rentgenová fluorescenční analýza (XRF)

Rentgenová

Radionuklidová

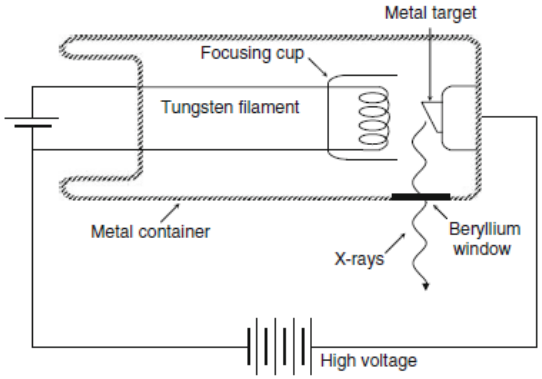

Fig. 37.1 X-ray tube ("Fundamentals of Physics", Second Edition Extended, David Halliday and Robert Resnick, copyright 1981, Reproduced with permission of John Wiley & Sons, Inc.)

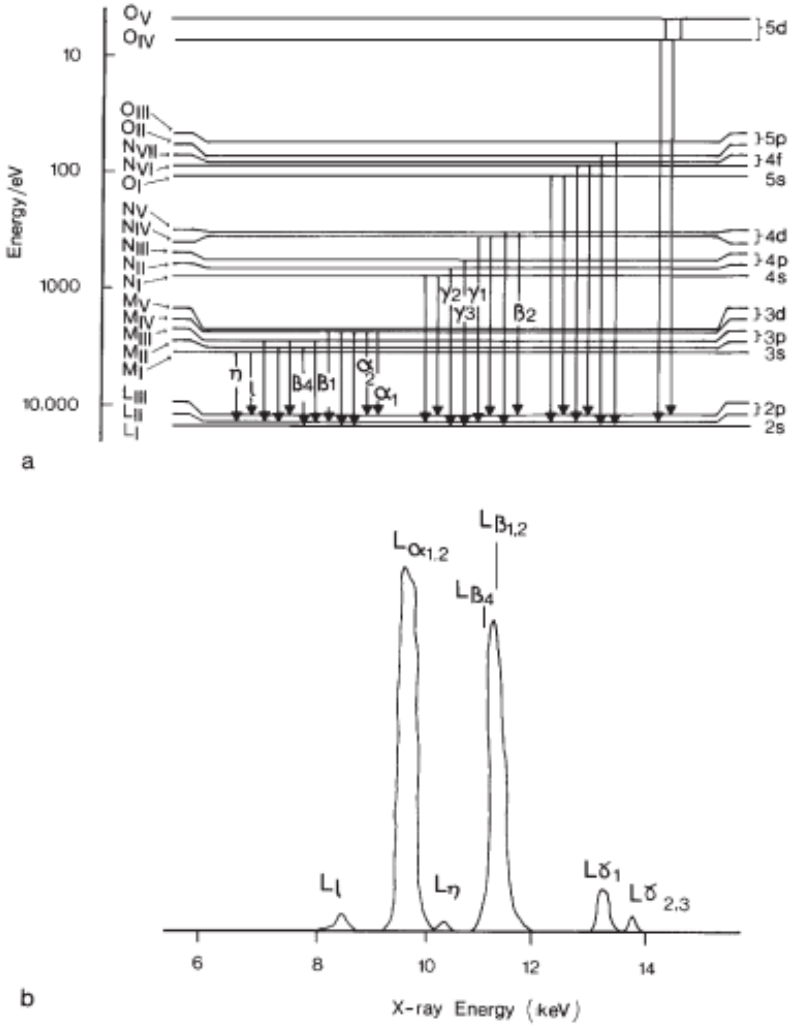

Figure 2.8 Electronic transitions giving rise to the L spectrum of gold. The L spectrum is considerably more complicated with three main lines normally resolved as shown in the accompanying spectrum – L_α (arising from two transitions), L_β (with up to 17 contributing transitions) and L_γ (up to 8 transitions), plus a number of 'forbidden' transitions. (After Jenkins, 1974; Fig. 2–11. © John Wiley & Sons Limited. Reproduced with permission.)

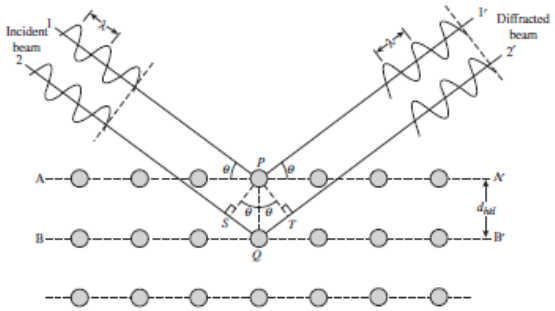

Figure 2.6 Bragg diffraction by crystal planes. The path difference between beams 1 and 2 is $SQ + QT = 2\,PQ \sin\theta$. (Reproduced with permission from W.J. Callister Jr., *Materials Science and Engineering: An Introduction*, 7th ed., John Wiley & Sons Inc., New York. © 2006 John Wiley & Sons Inc.)

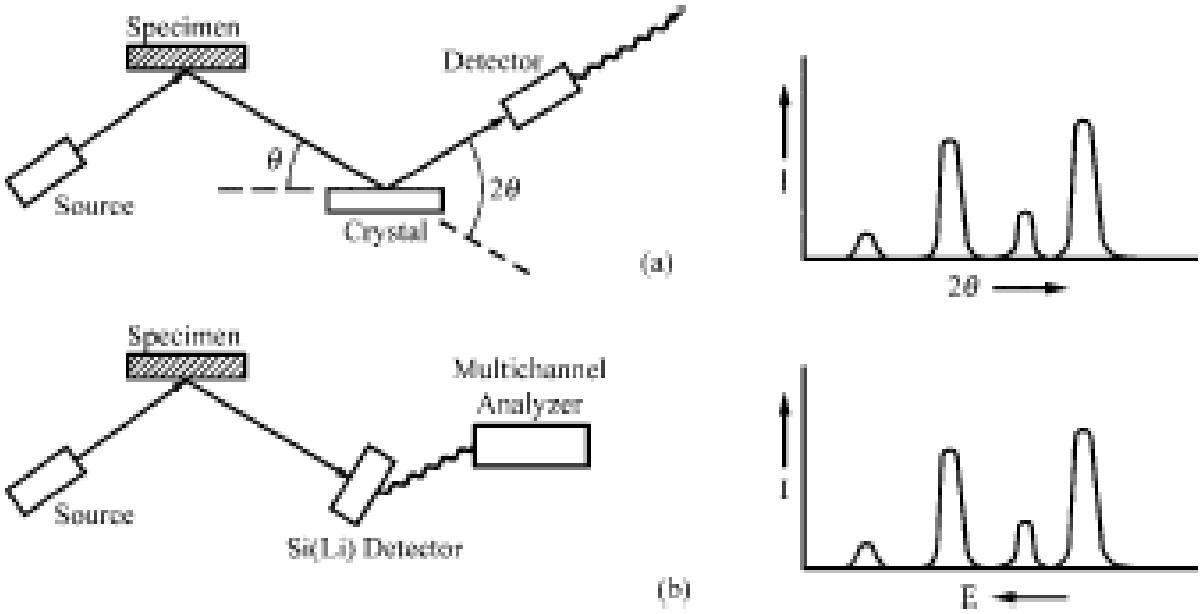

Figure 6.6 Main components and dispersive spectra of: (a) WDS; and (b) EDS.

Portable X-Ray Fluorescence (PXRF)

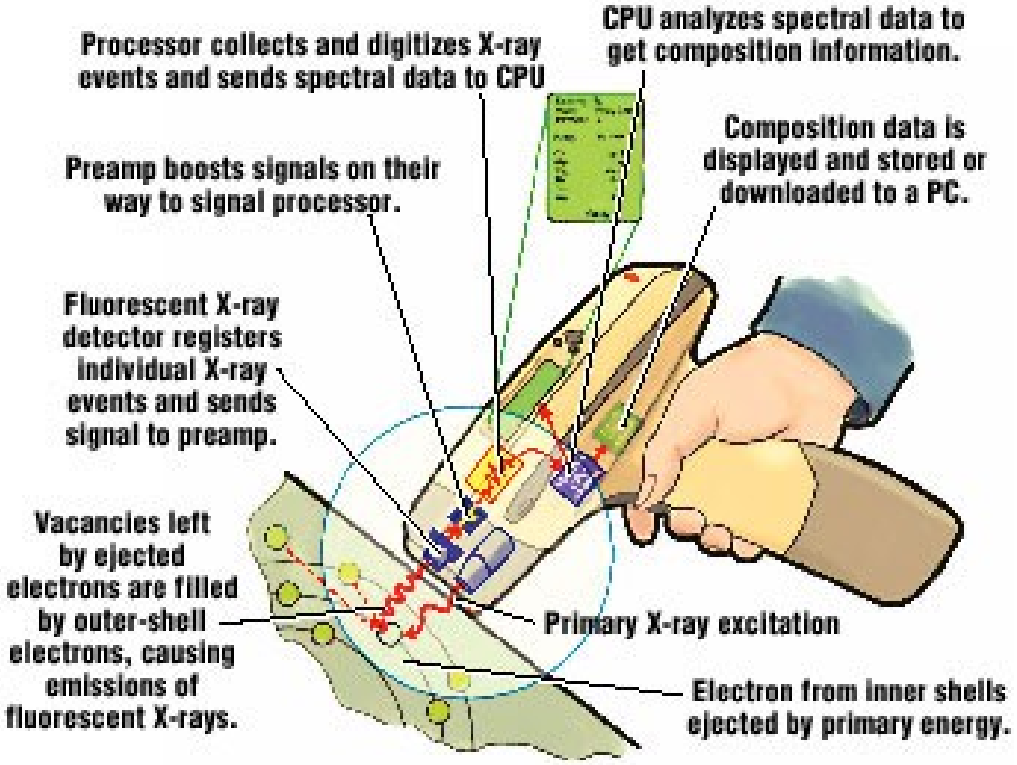

Rentgenofluorescenční analýza

Prvková analýza, zejm. těžké kovy

UV-VIS Spektrofotometrie

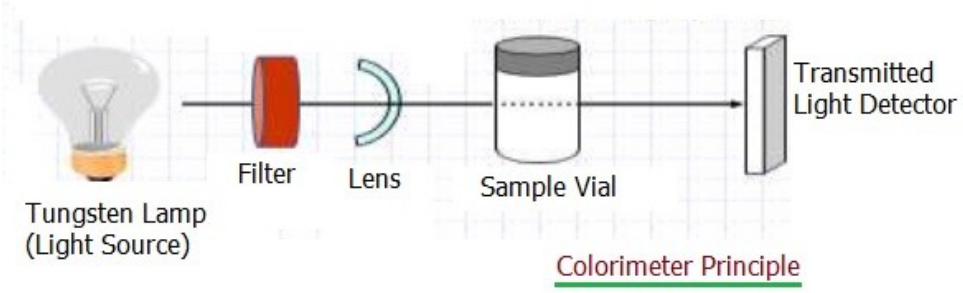

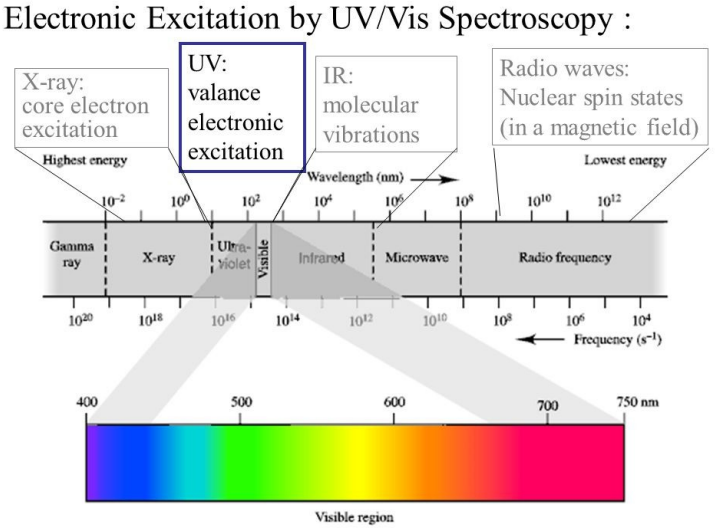

Barva sloučeniny je dána selektivní absorpcí světelného záření různých vlnočtů. Pokud látka absorbuje v celém rozsahu tj. 13000 - 25000 cm^{-1} jeví se jako **černá**. Zbarvení je totožné s barvou propuštěného nebo odraženého světla.

V případě, že látka absorbuje přibližně monochromatické světlo, je zabarvení látky v komplementární barvě

Spektrální barva	indigová	modrá	modro-zelená	zelená	žlutá	červená
Vlnočet /10^3 cm^{-1}	25	23	21	19	17.5	13
Komplementární barva	citronová	žlutá	červená	fialová	modrá	modro-zelená

VIS 400 – 760 nm

CHROMOFOR – „nositel barevnosti“ – funkční skupiny, strukturní prvky - C = C - C = C - - C = O - N = N -  - C ≡ C -

AUXOCHROM – vazba na chromofor – prohloubení barevnosti

- $\overline{\underline{O}}H$ - $\overline{N}H_2$ - $\overline{\underline{Cl}}|$ - $\overline{\underline{Br}}|$ (volné el. páry schopné konjugace s el. systémem chromoforu)

auxochrom → chromofor → posun a změna ε_r

Posun
- k delším λ - BATHOCHROMNÍ (červený)
- ke kratším λ - HYPSOCHROMNÍ (modrý)

ε_r
- vzrůst = HYPERCHROMNÍ posun
- pokles = HYPOCHROMNÍ posun

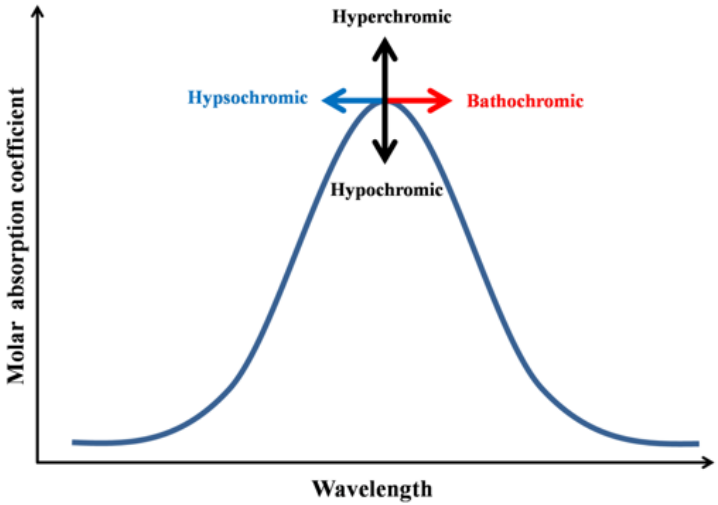

Vliv prostředí

pH

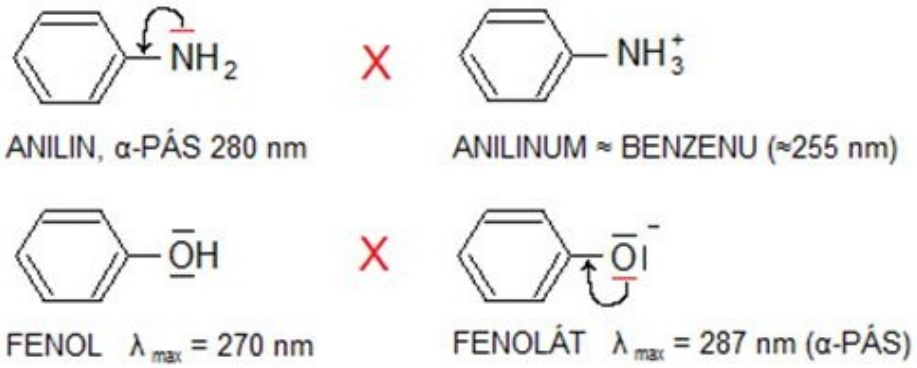

Polarita rozpouštědla

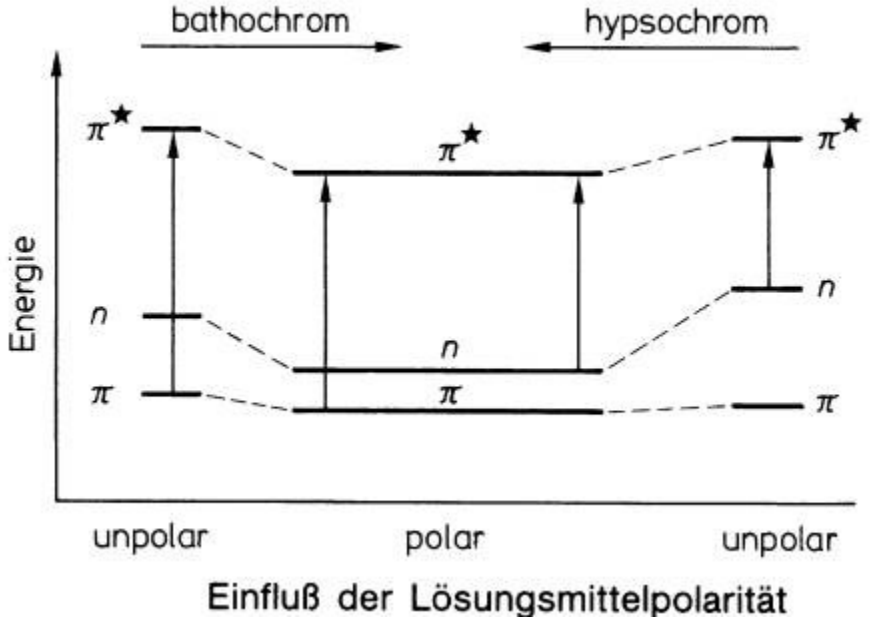

➢ Chromophores are characteristic groups of atoms in molecules that absorb certain wavelengths of uv or visible light

– π-π* transition in nonconjugated double bonds ~ 160 nm, but for molecules with many conjugated double bonds it is the visible region.

– *n*-π* transition in the carbonyl group ~ 280 nm

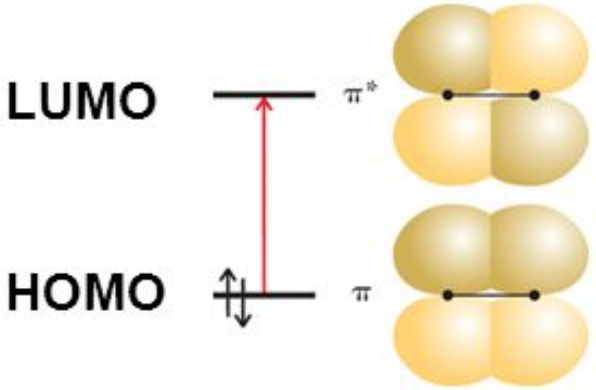

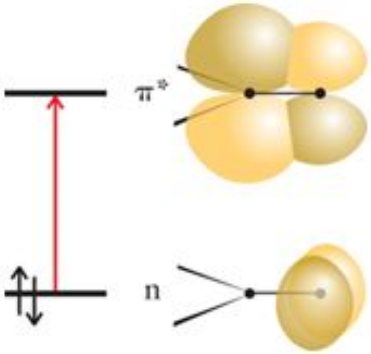

- *d*-to-*d* transition in d-metal complexes in visible ranges

- charge transfer transition in d-metal complexes electrons migrate from the ligands to the metal atom or vice versa.

E.g. deep purple color of MnO_4^-

Aplikace: stanovení fosforu

$$12(NH_4)_2MoO_4 + H_3PO_4 + 21\ HNO_3 \rightarrow \mathbf{(NH_4)_3PMo_{12}O_{40}}\downarrow + 21\ NH_4NO_3 + 12\ H_2O$$

+ red. → molybdenová modř

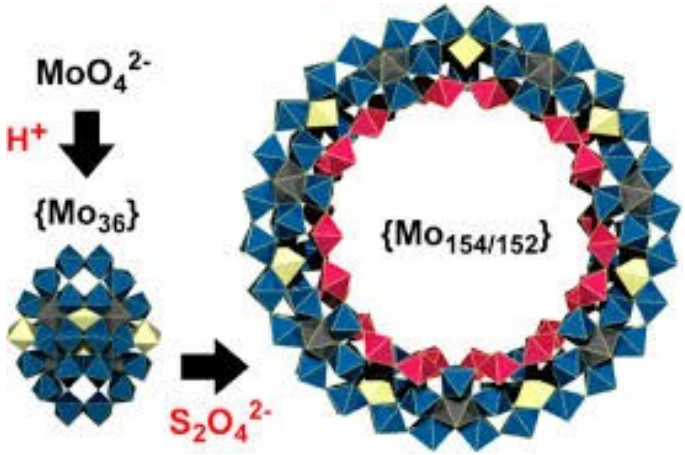

→

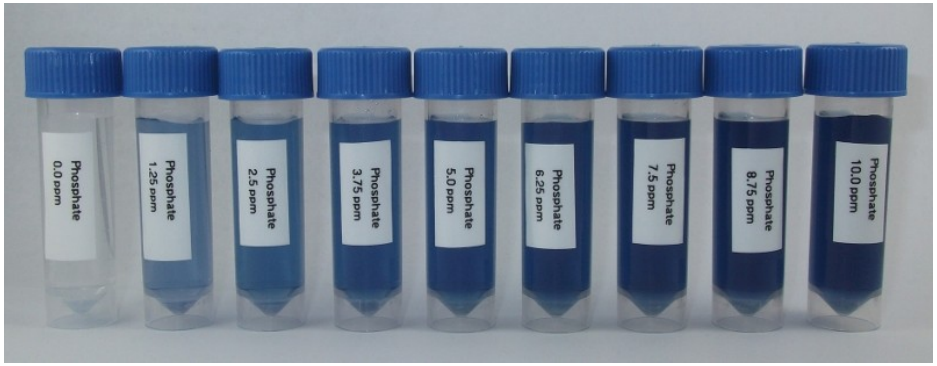

Suchohrdly-Deblínek

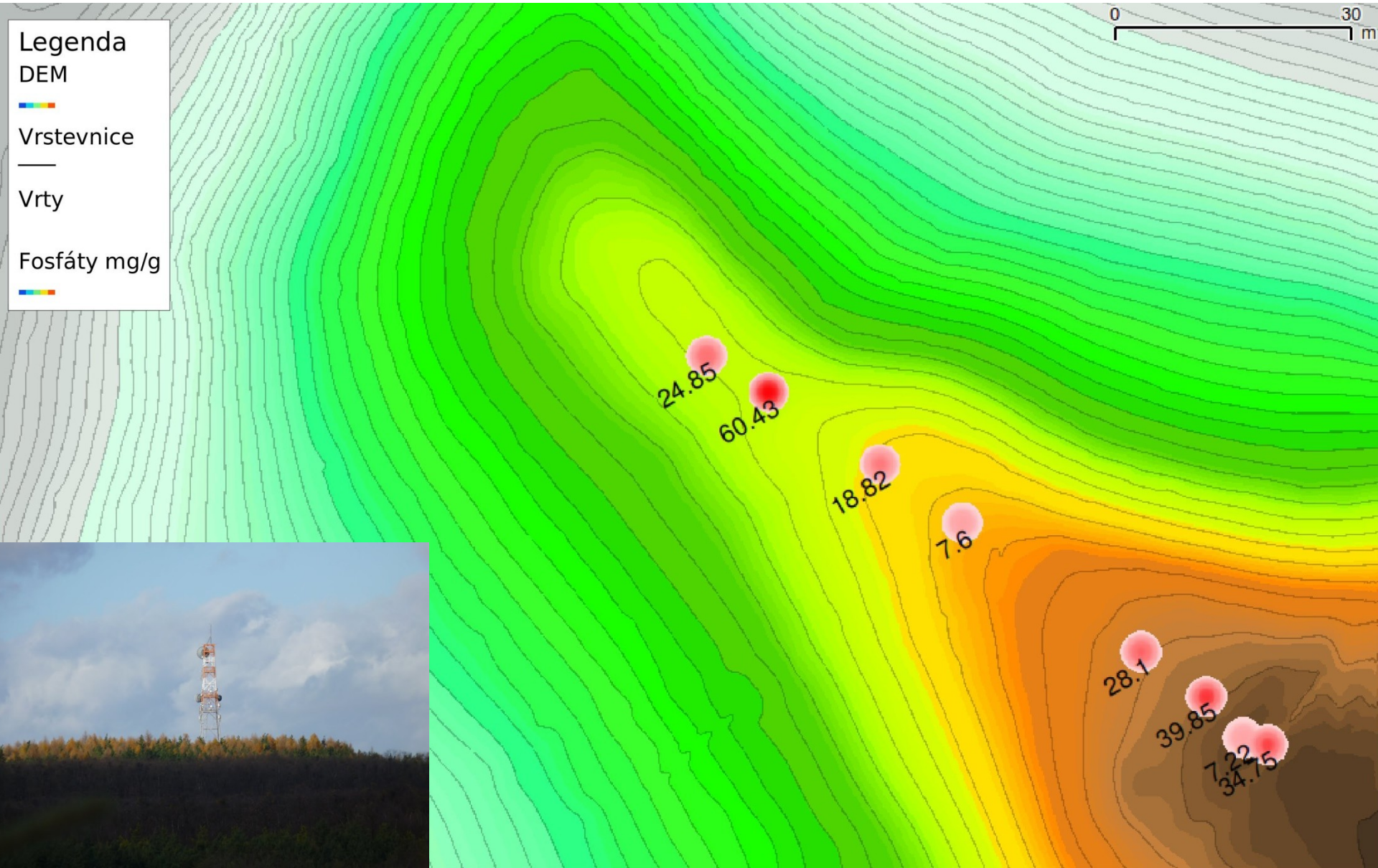

Pohansko u Břeclavi

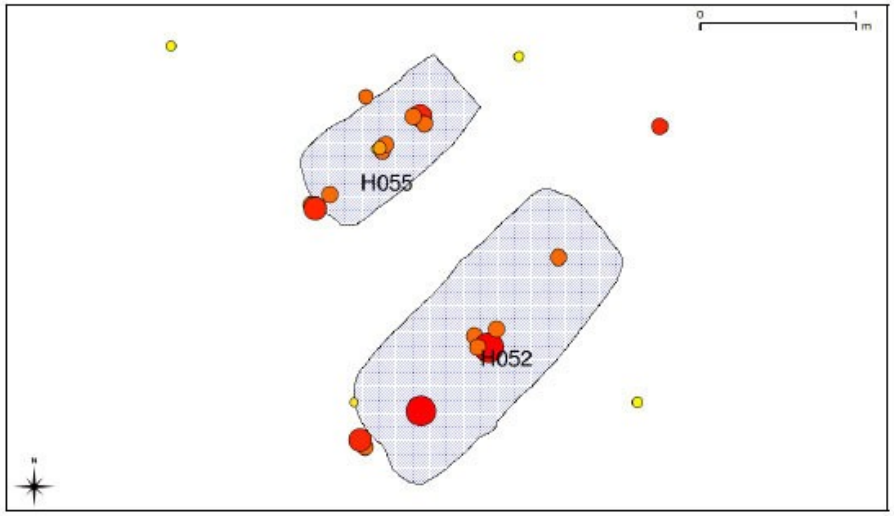

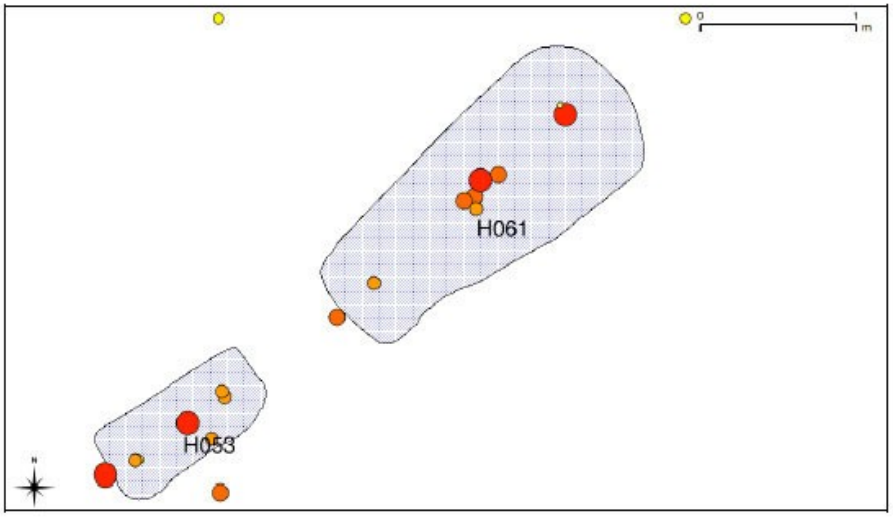

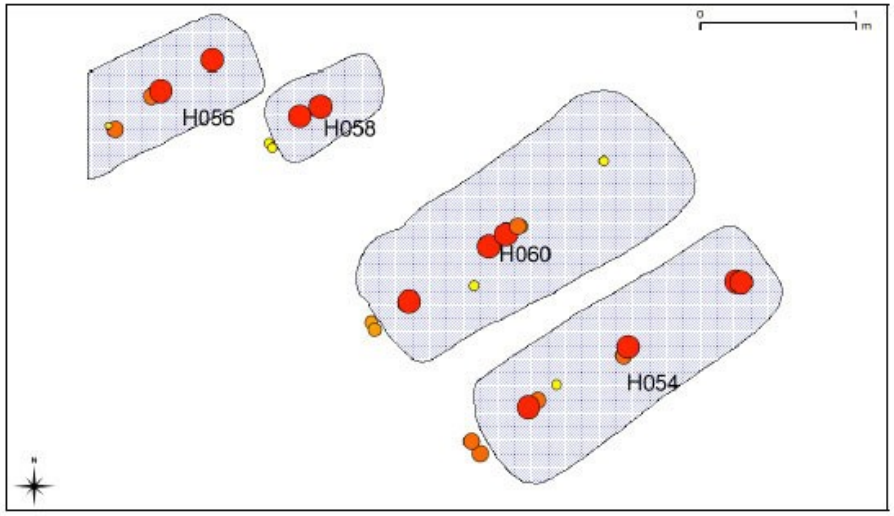

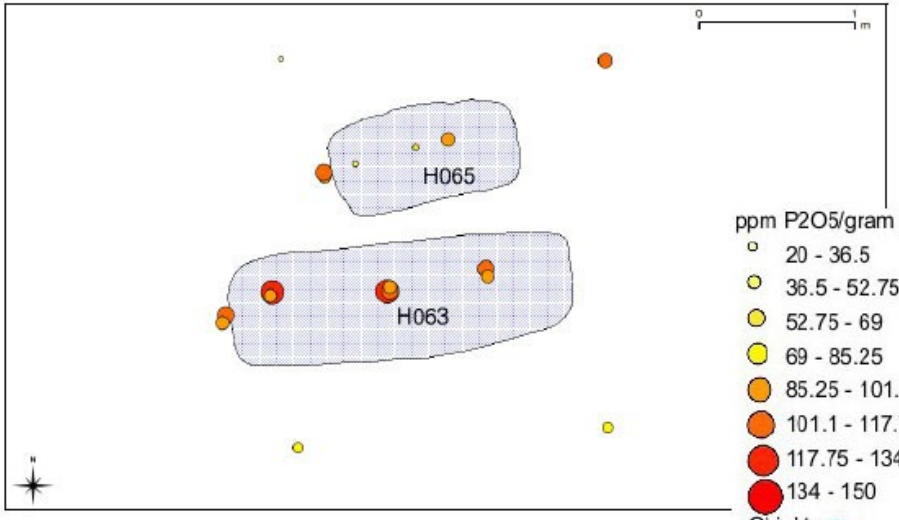

Kyjov

Hrob H 1034

pohřeb je narušen v místech, kde se nacházely hlavy a trupy pohřbených jedinců

dolní končetiny jsou v obou případech sekundárním zásahem prakticky neporušené

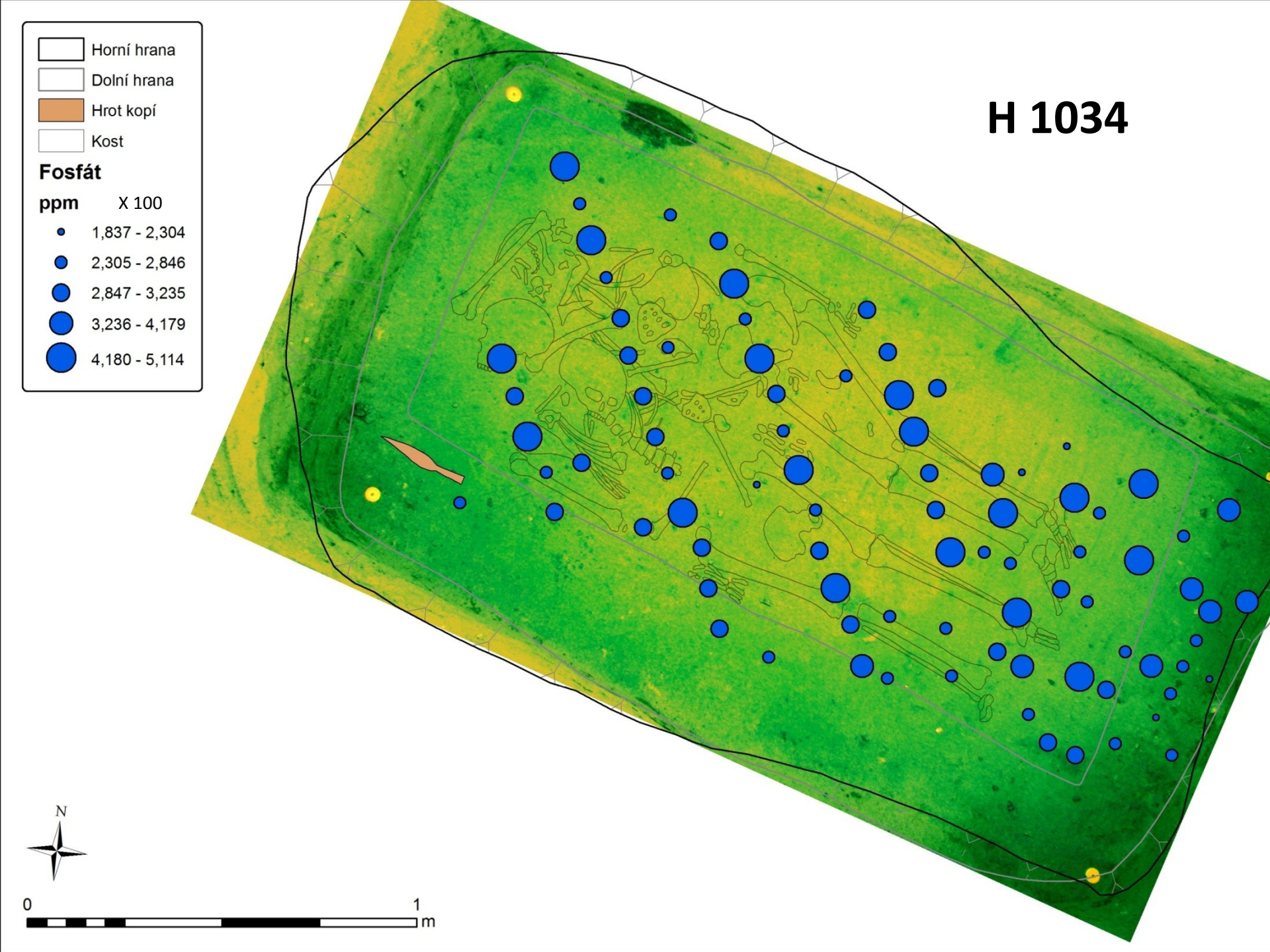
Horní hrana
Dolní hrana
Hrot kopí
Kost
Fosfát
ppm X 100
1,837 - 2,304
2,305 - 2,846
2,847 - 3,235
3,236 - 4,179
4,180 - 5,114
H 1034
N
0
1
m

Rozklad distribuce na gaussovské složky metodou maximální věrohodnosti

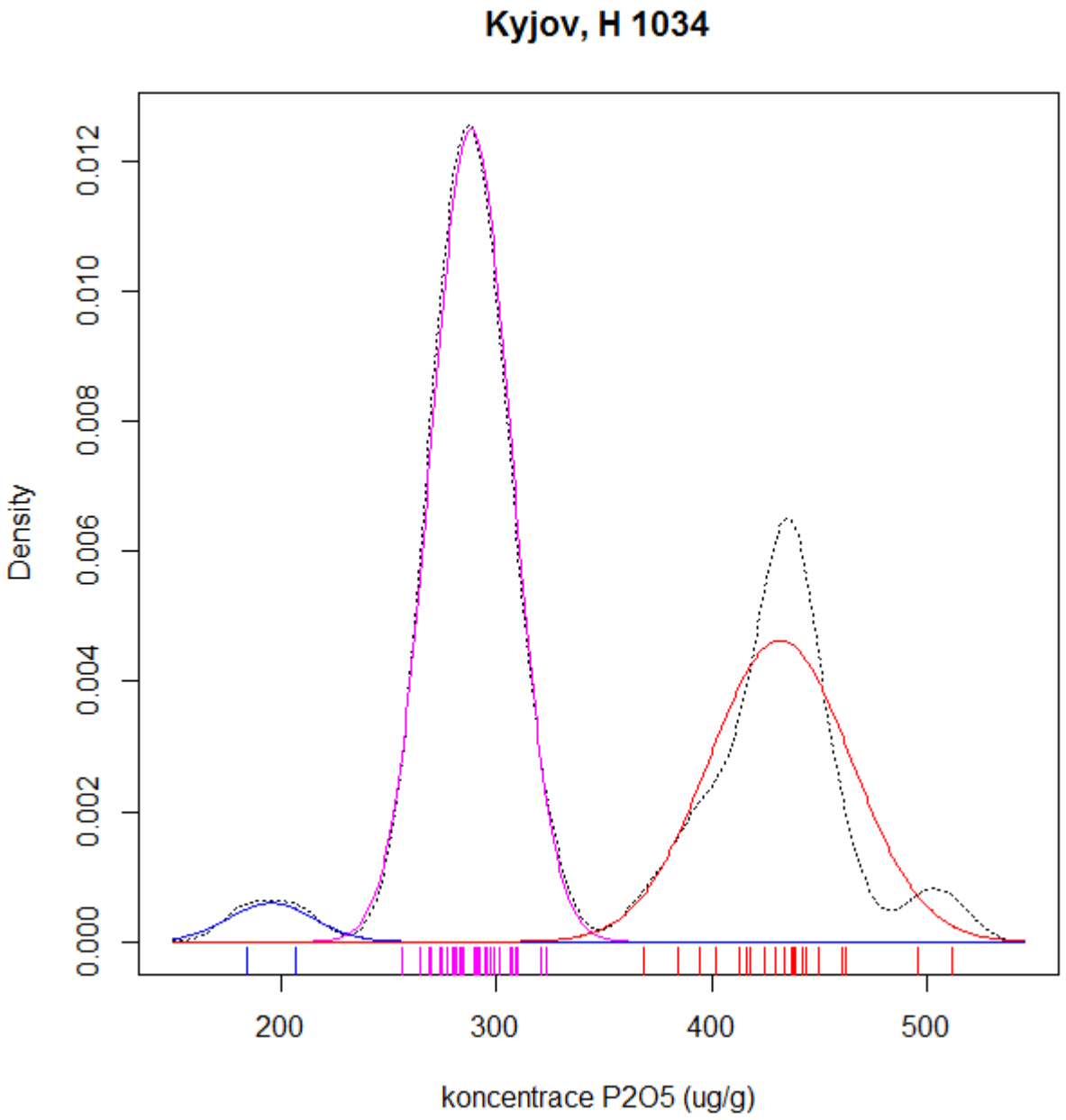

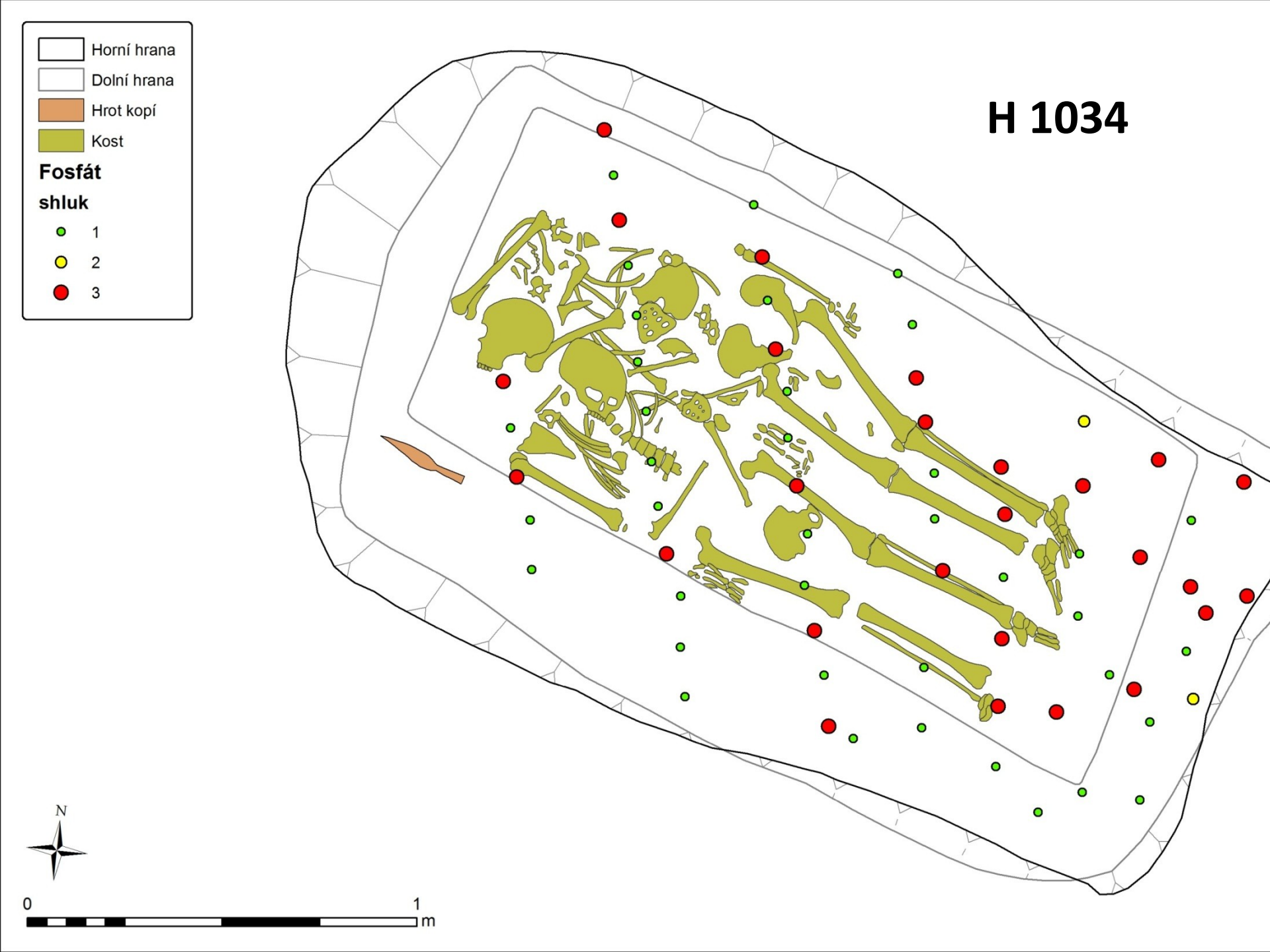
Horní hrana
Dolní hrana
Hrot kopí
Kost
Fosfát
shluk
1
2
3
H 1034
N
0
1
m

Kolorimetrie

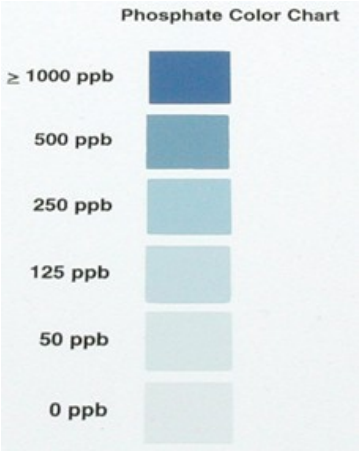

Signal processing

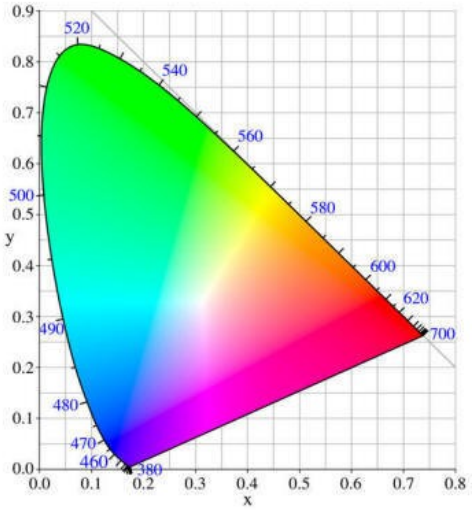

Detekční trubičky na plyny

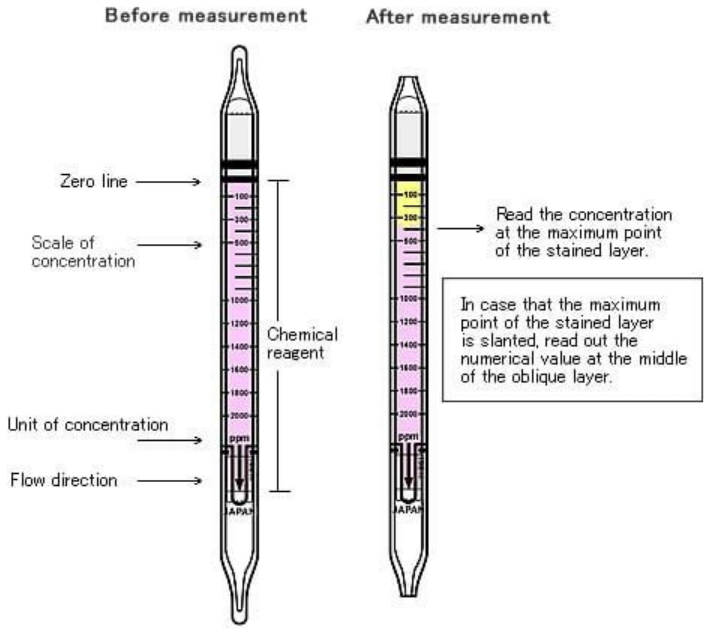

Kolorimetrie

Fosfor

pH

Železo

Dusík (amoniakální, nitrátový)

Kolorimetrie - aplikace mobilního telefonu

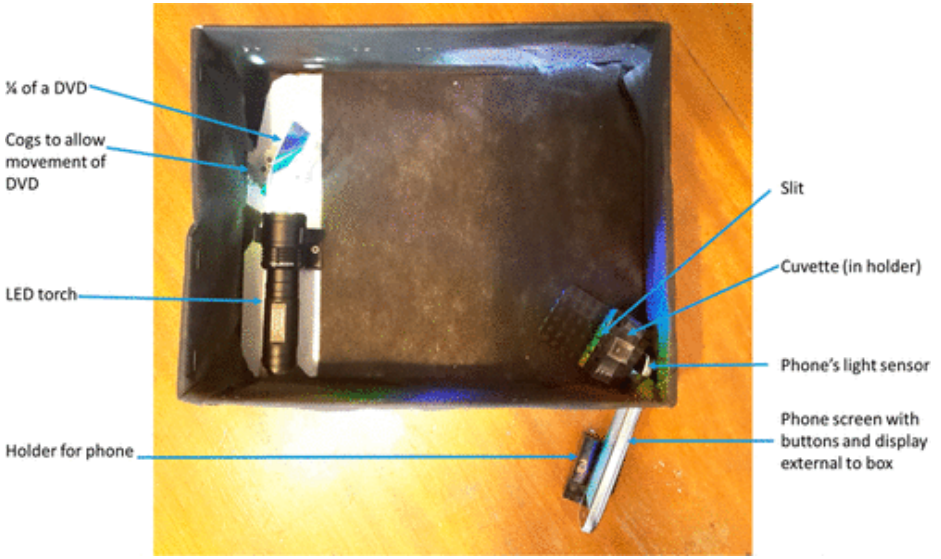

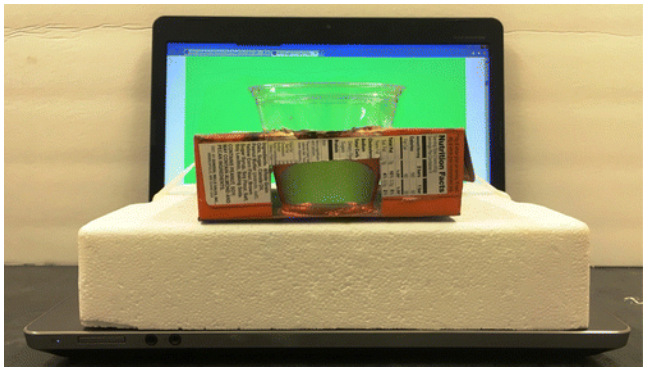

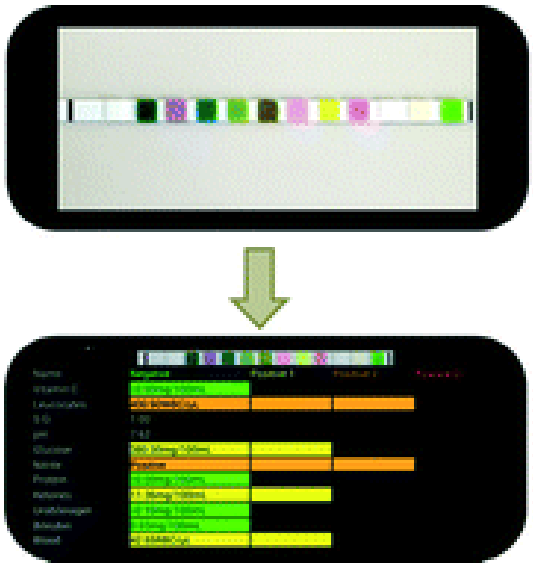

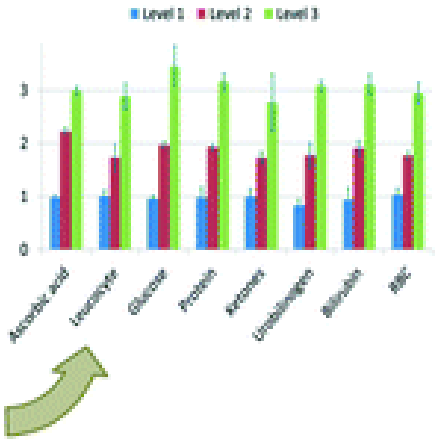

Kolorimetrie

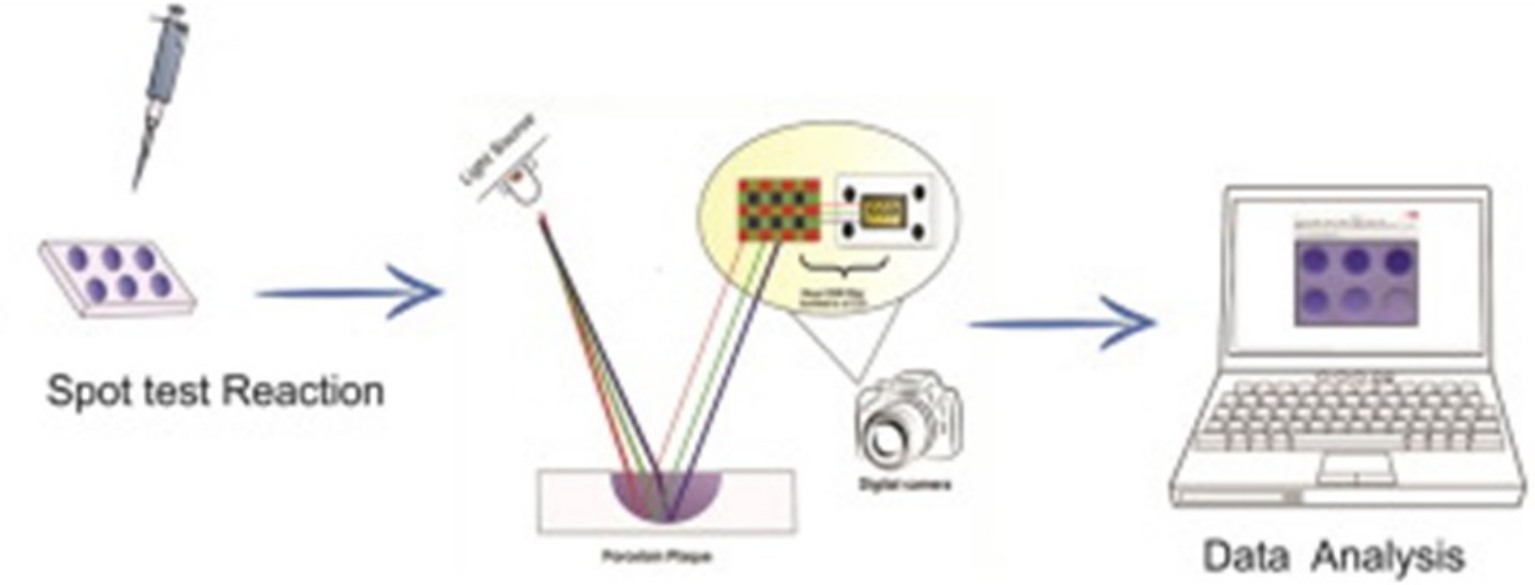

Signal processing

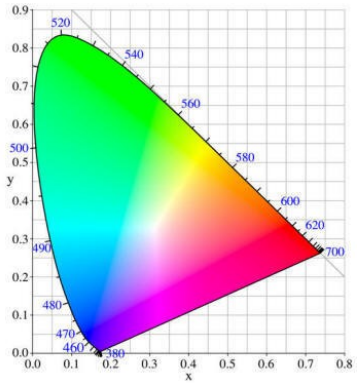

Polní test na fosfáty

Pohansko

(raný středověk)

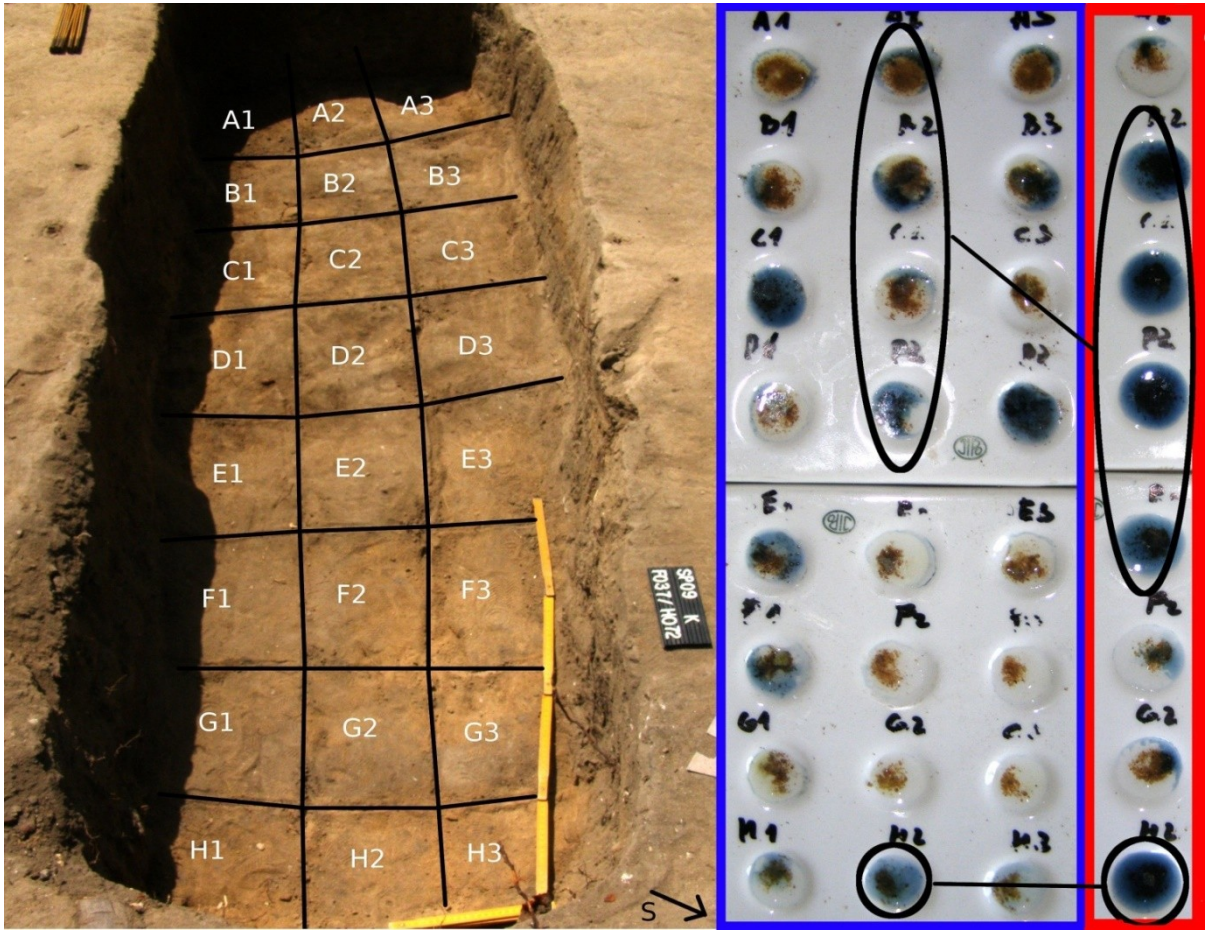

Luminiscenční spektrometrie

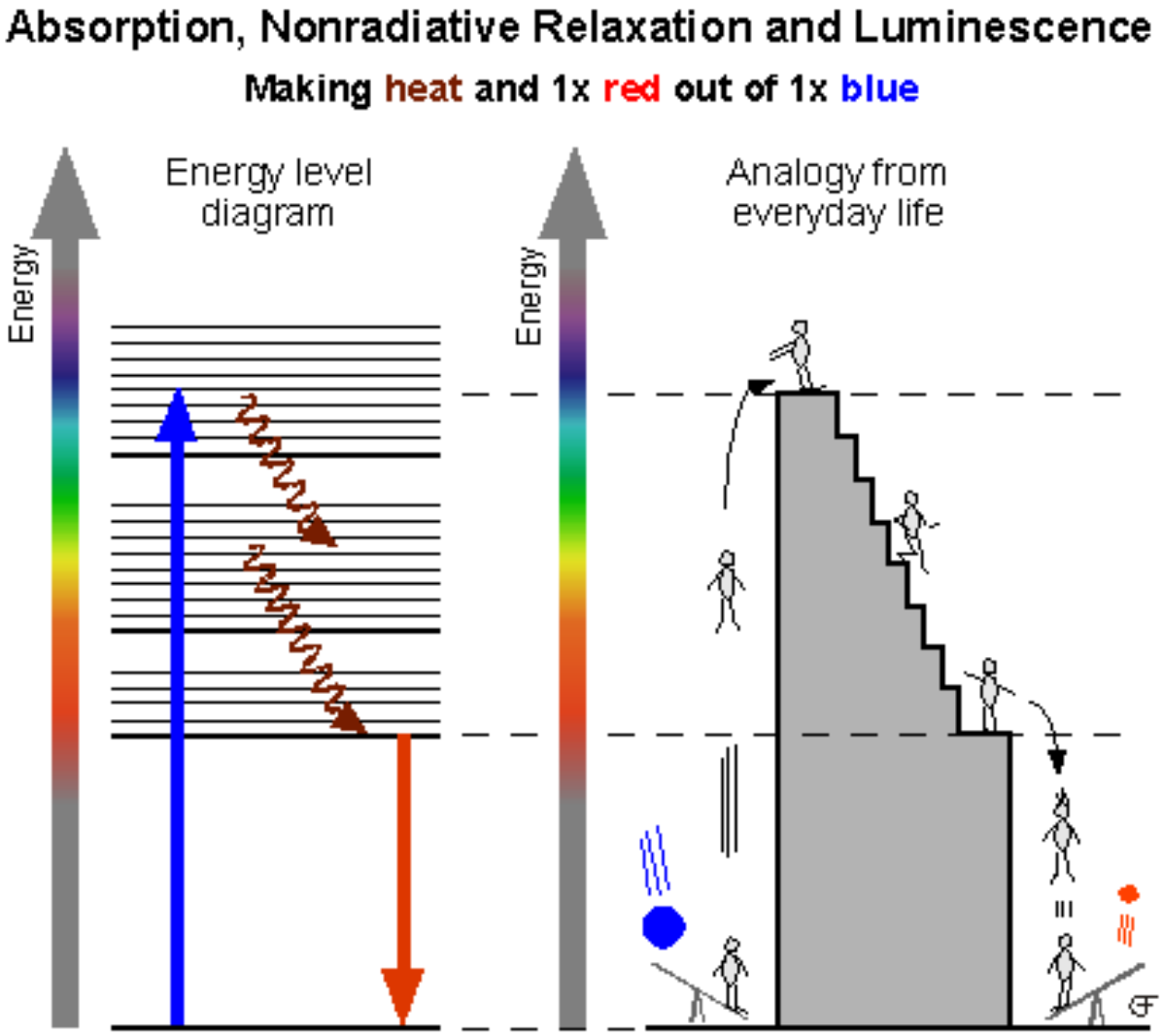

Fluorescence

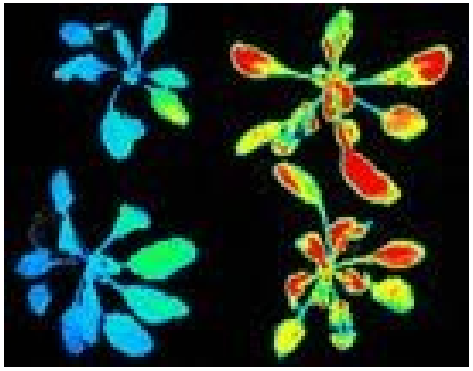

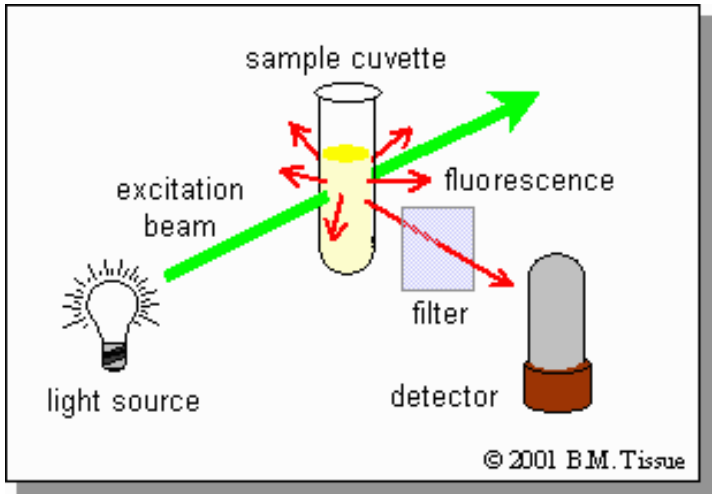

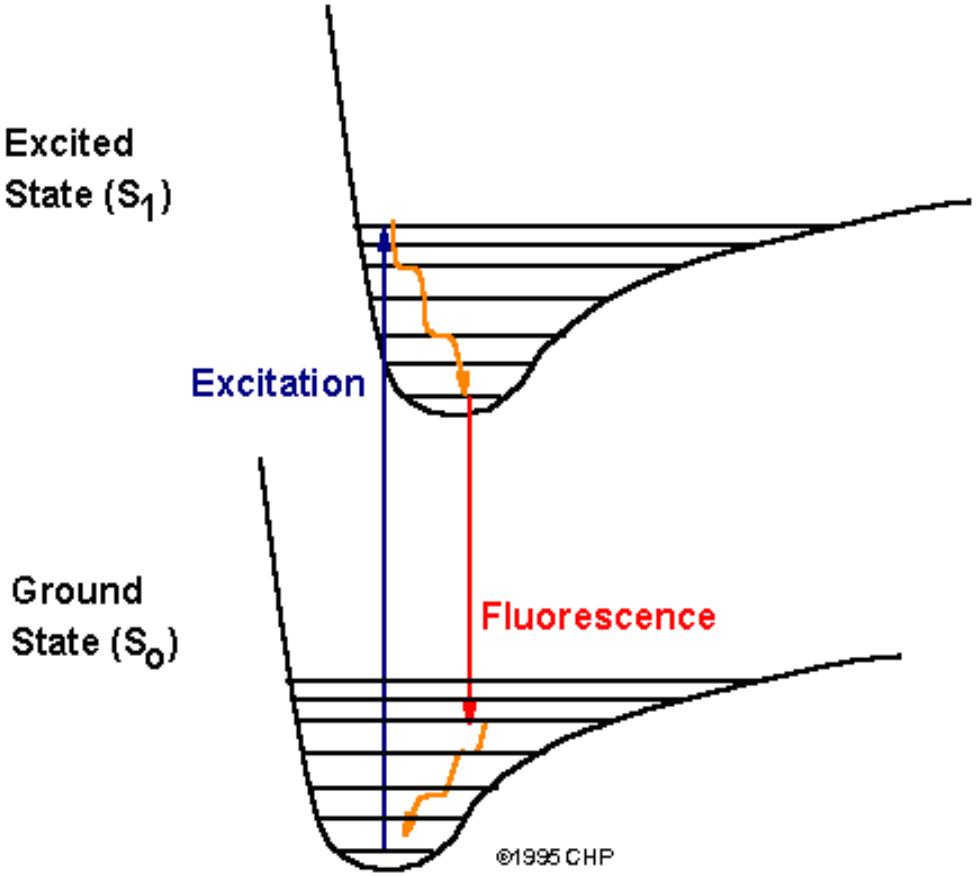

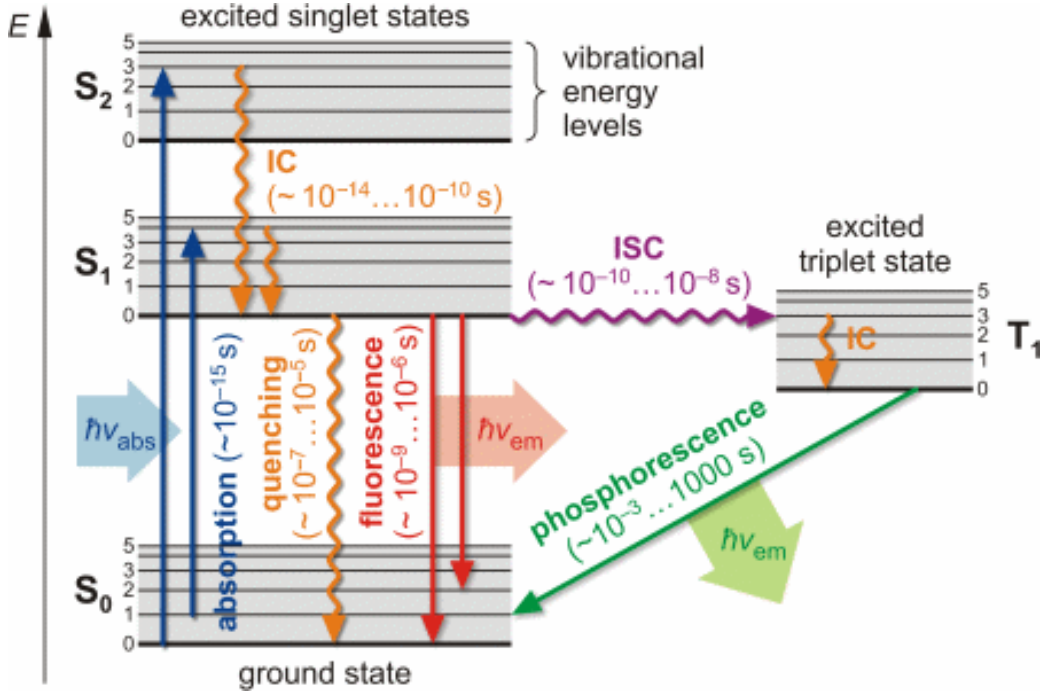
E
excited singlet states
S2
S1
S0
vibrational energy levels
IC
(~ 10−14…10−10 s)
ISC
(~ 10−10…10−8 s)
excited triplet state
T1
IC
hνabs
absorption (~10−15 s)
quenching (~10−7…10−5 s)
fluorescence (~ 10−9…10−6 s)
hνem
phosphorescence (~10−3 …1000 s)
hνem
ground state

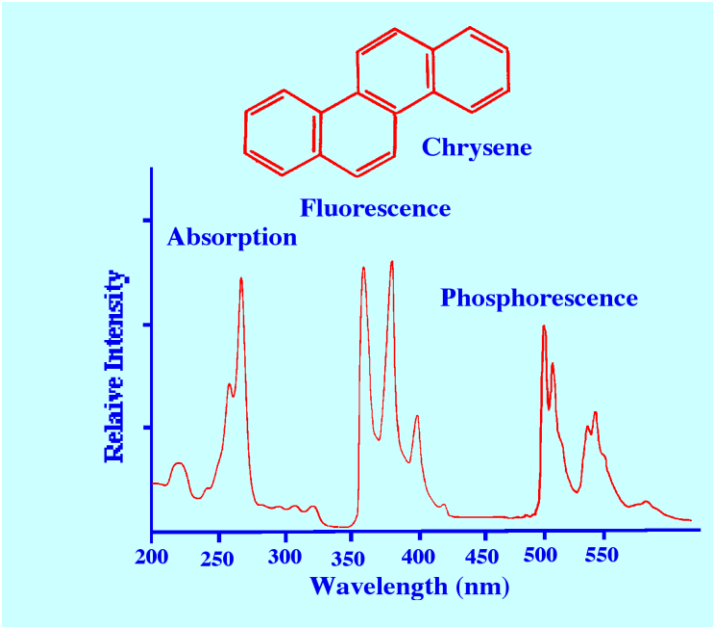
Chrysene
Fluorescence
Absorption
Phosphorescence
Relaive Intensity
200
250
300
350
400
450
500
550
Wavelength (nm)

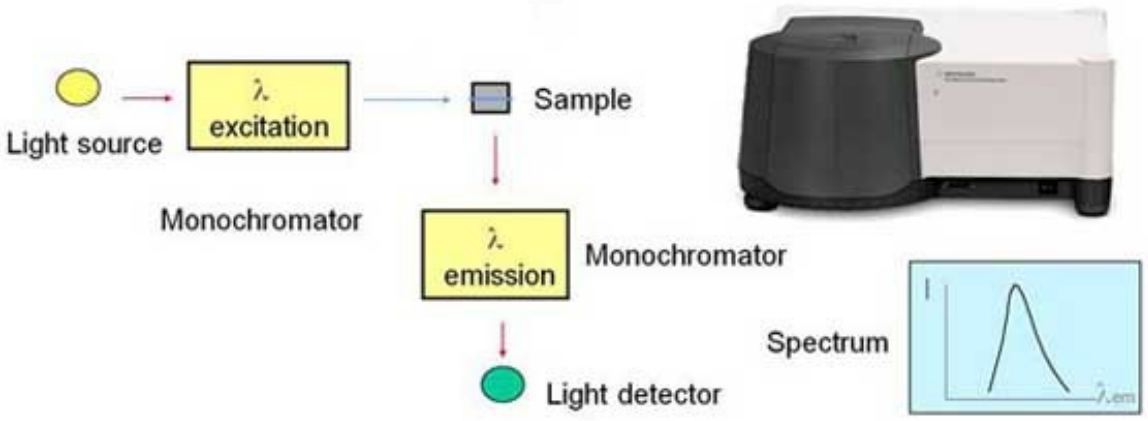
Light source
λ excitation
Sample
Monochromator
λ emission
Monochromator
Light detector
Spectrum
I
λem

Fluorescence

Aplikace ultrafialové fluorescence - zviditelnění časem degradovaného textu

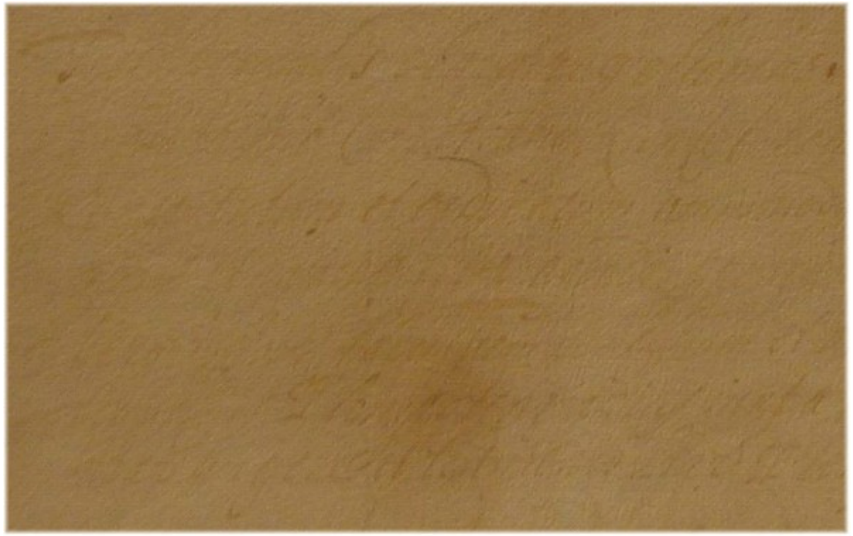

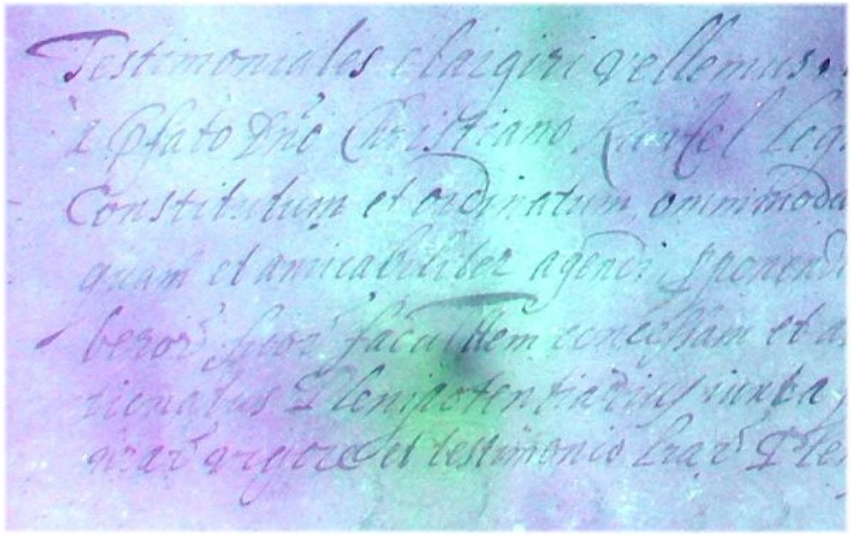

Laser induced fluorescence

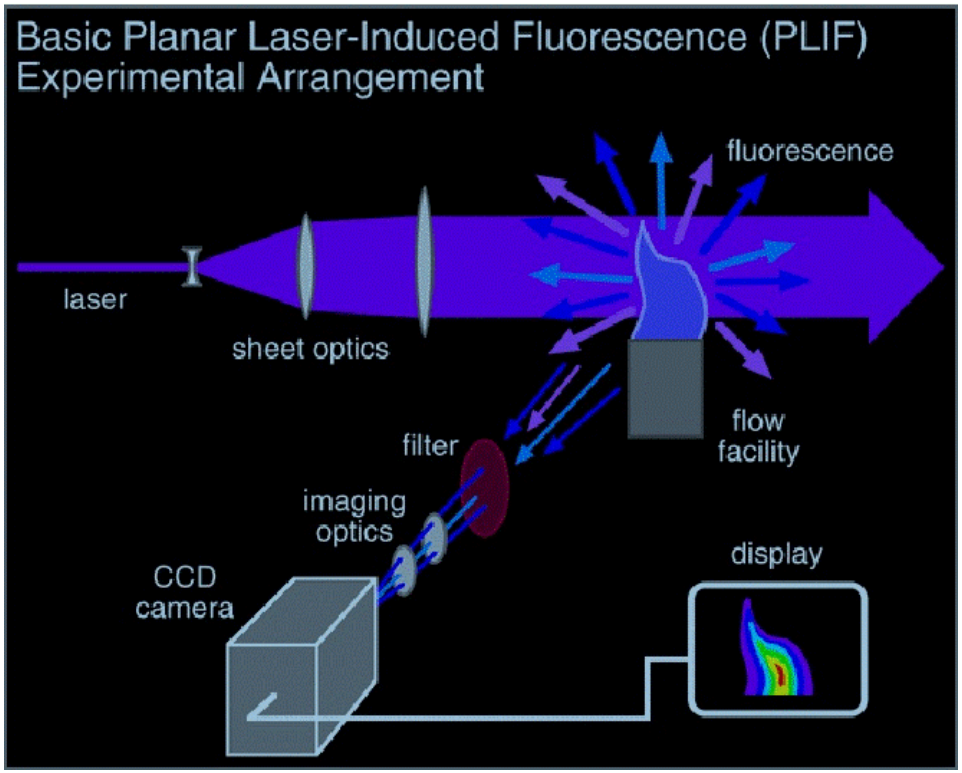

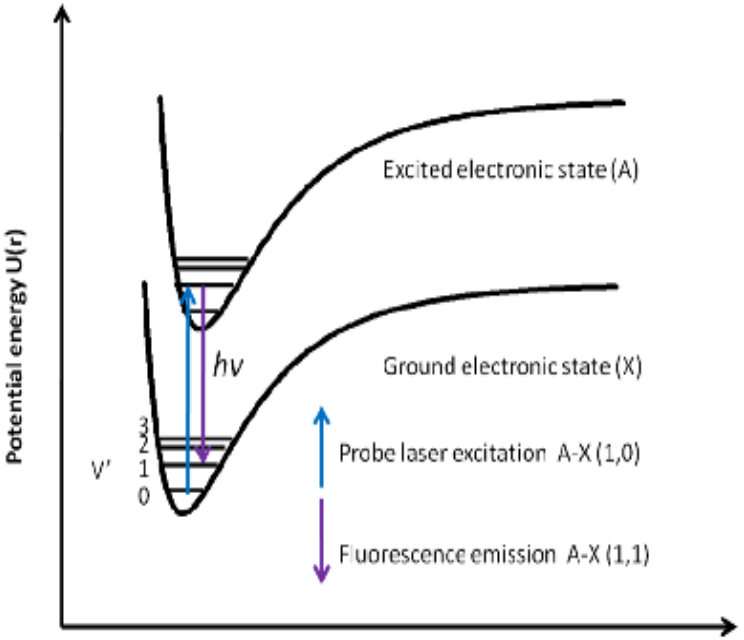

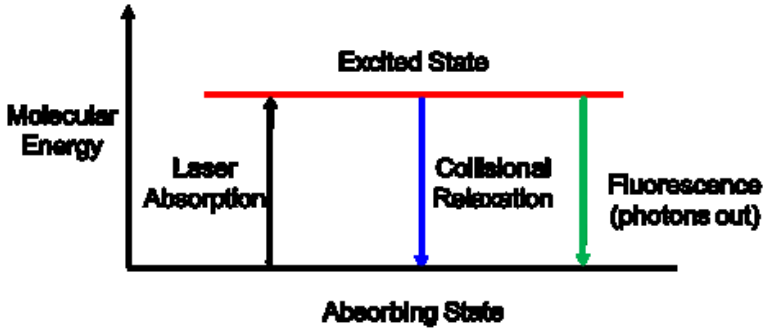

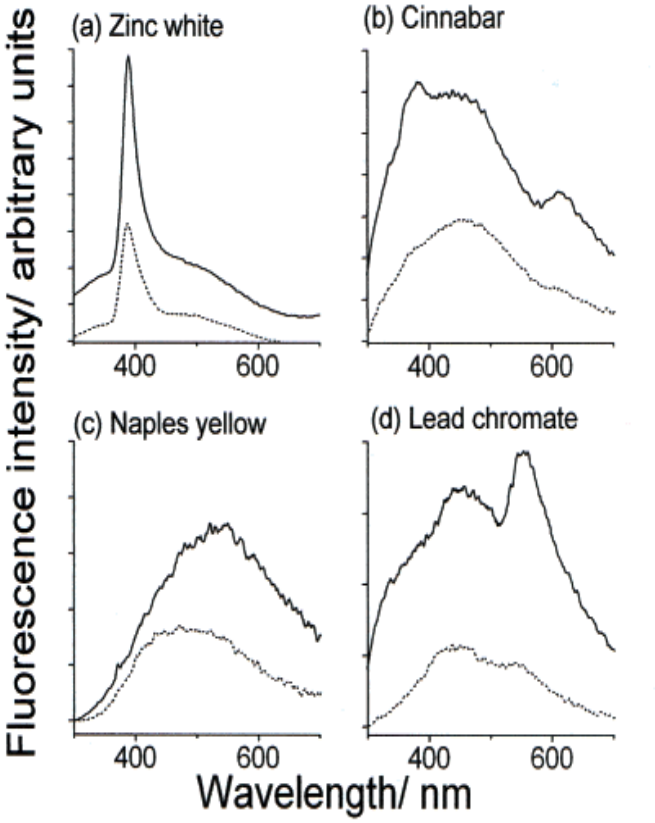

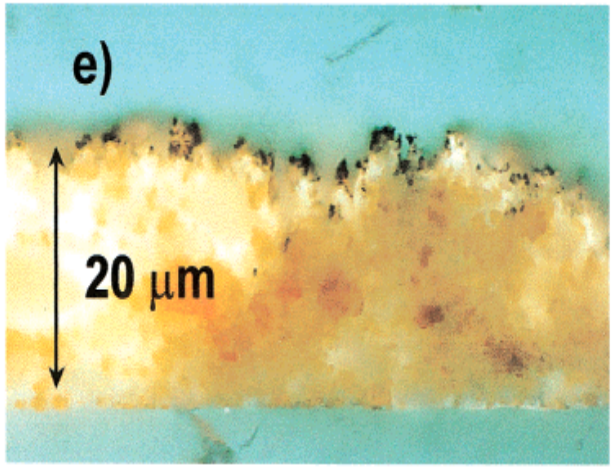

Pigmenty

LIF spectra of unvarnished tempera systems taken at a resolution of 1 nm with a laser fluence of 1.2 mJ cm-2:

(a) zinc white,
(b) cinnabar,
(c) Naples yellow, and
(d) lead chromate.

The exciting laser wavelength is 248 nm.

(e) UV fluorescence image of a cross section of an unvarnished laser-ablated region of a Naples yellow tempera sample. (Magnification is 500).

Detekce mikroorganismů

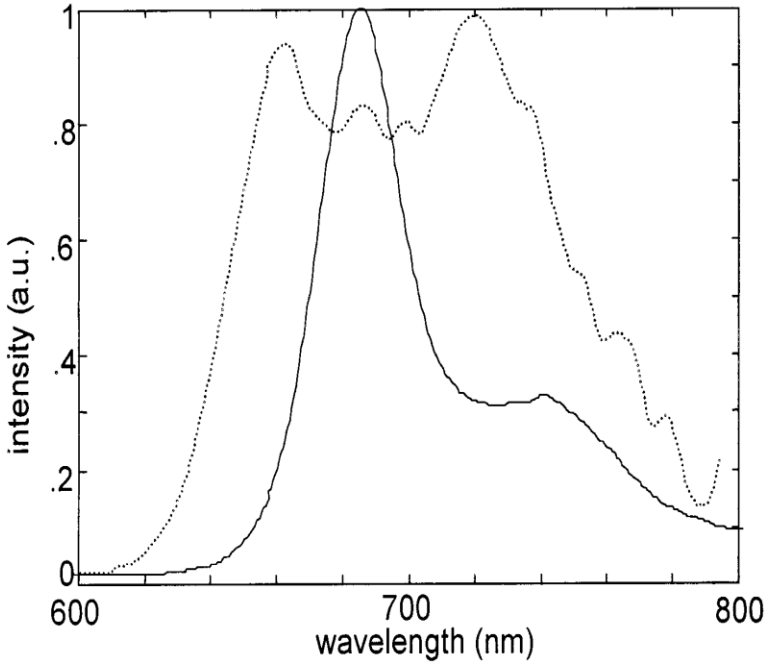

Normalised LIF spectra of green algae (continuous line) and cyanobacteria (dotted line). Excitation 355 nm.

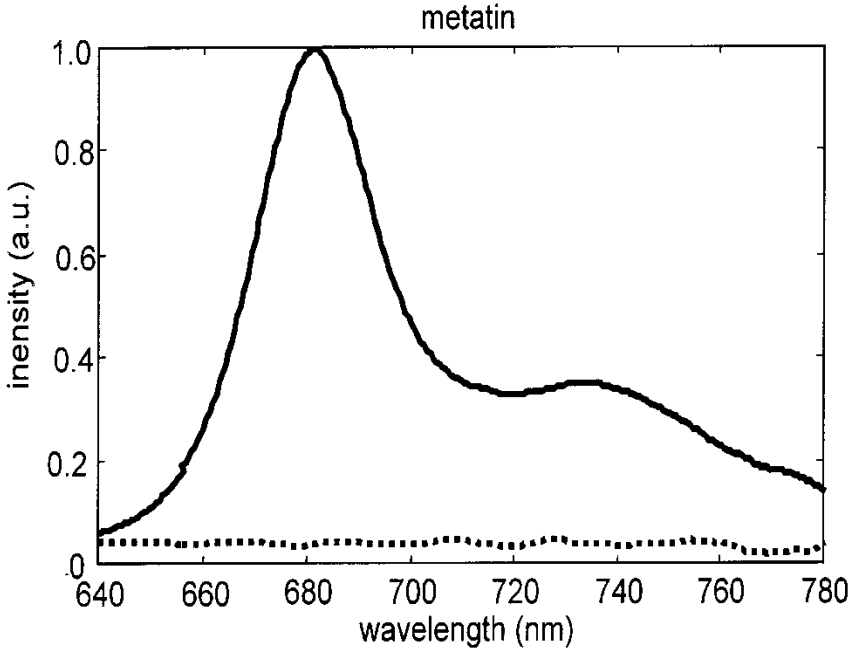

Fluorescence spectra of green algae on a marble substrate. Before a biocidal treatment (continuous line) and after (dotted line). Excitation wavelength 355 nm.

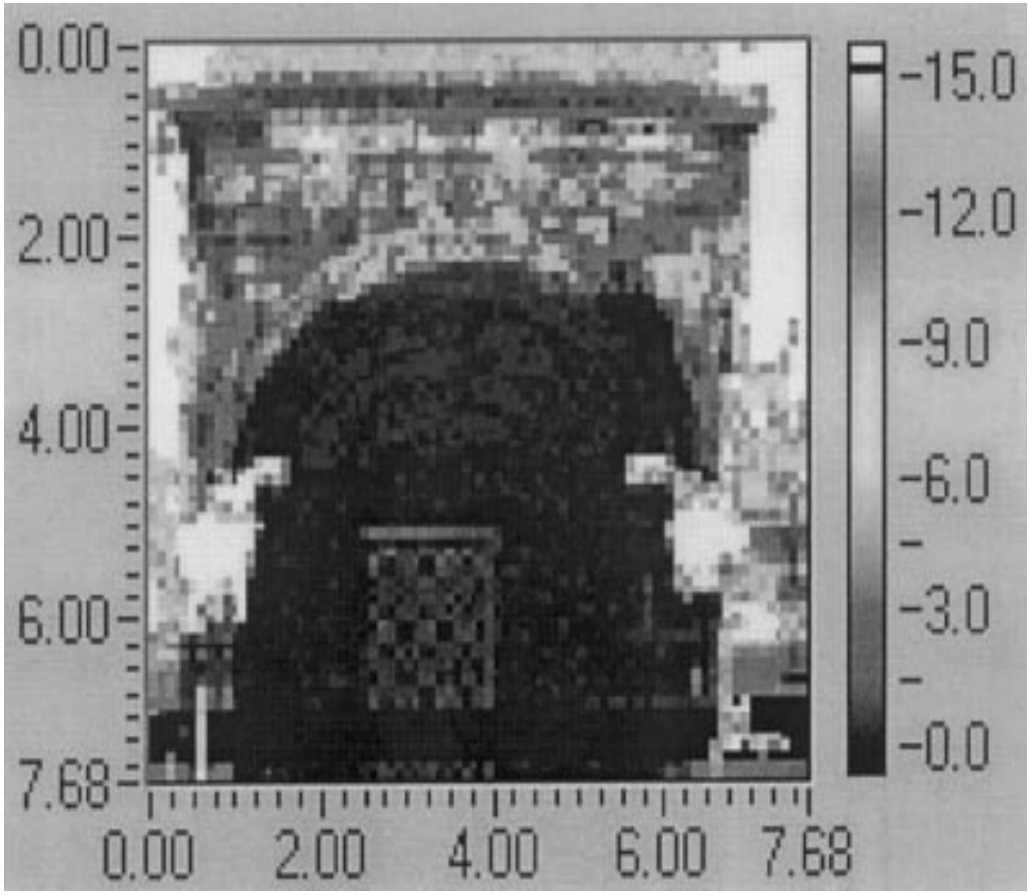

Fluorescence image related to the alga colonisation on the northern portal of **Lund Cathedral**. The intensity of the chlorophyll fluorescence in the band around 685 nm is indicated in grey levels and makes evident the important biodeteriogen colonisation on the stone surface.

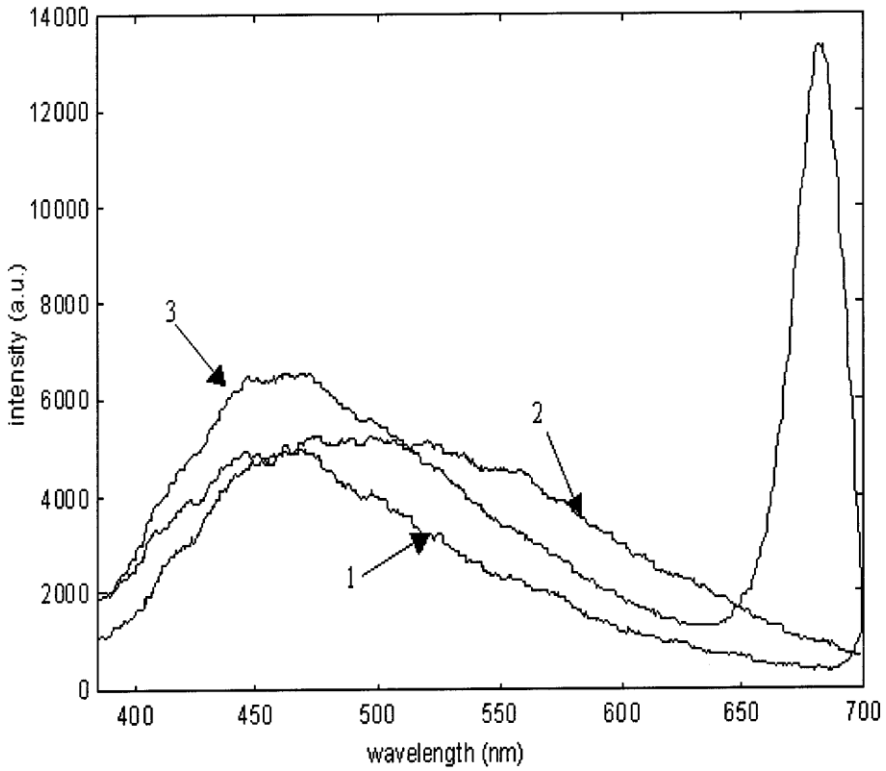

Fluorescence spectra of Ho¨ o¨ r sandstone from the external walls of Lund Cathedral:

1) 12th century stone;
2) 19th century stone;
3) 12th century stone with algae.

Excitation 337.1 nm. The same behaviour was observed in the remote measurements with the excitation at 355 nm.

Infračervená spektrometrie (FTIR)

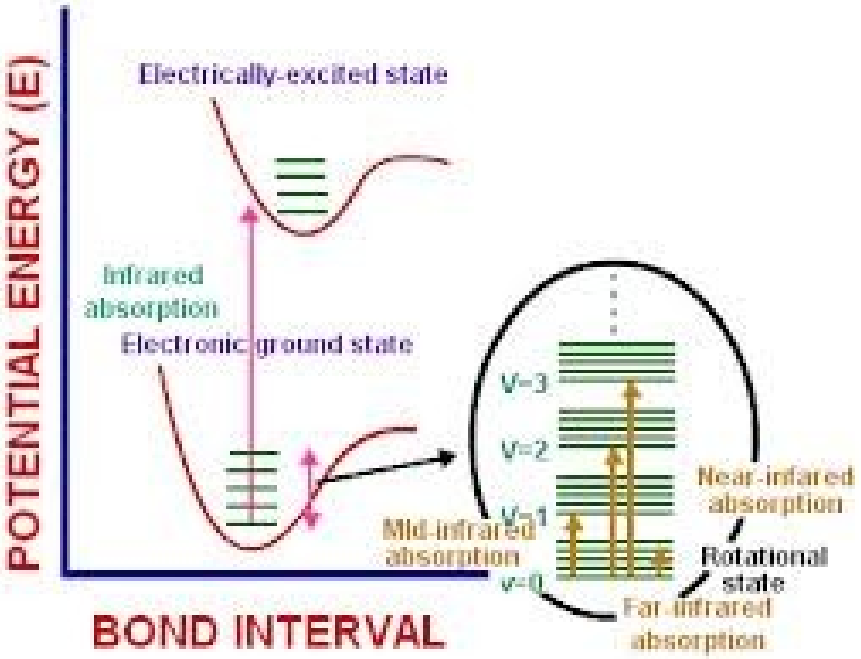

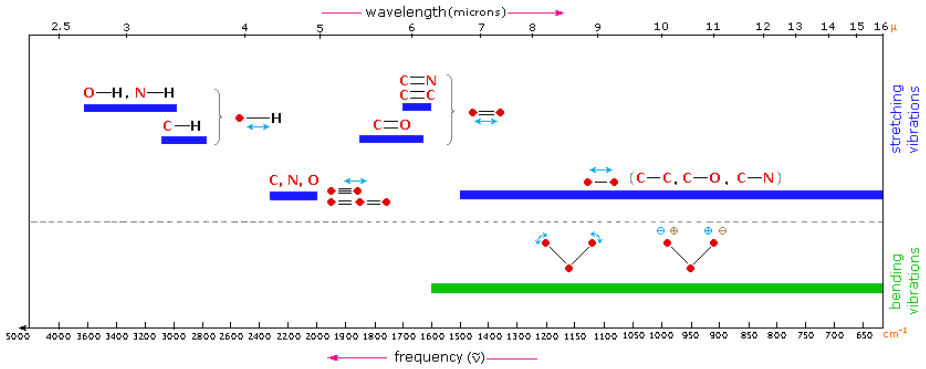

Raman vs. FTIR

FT IR

(FT) Raman

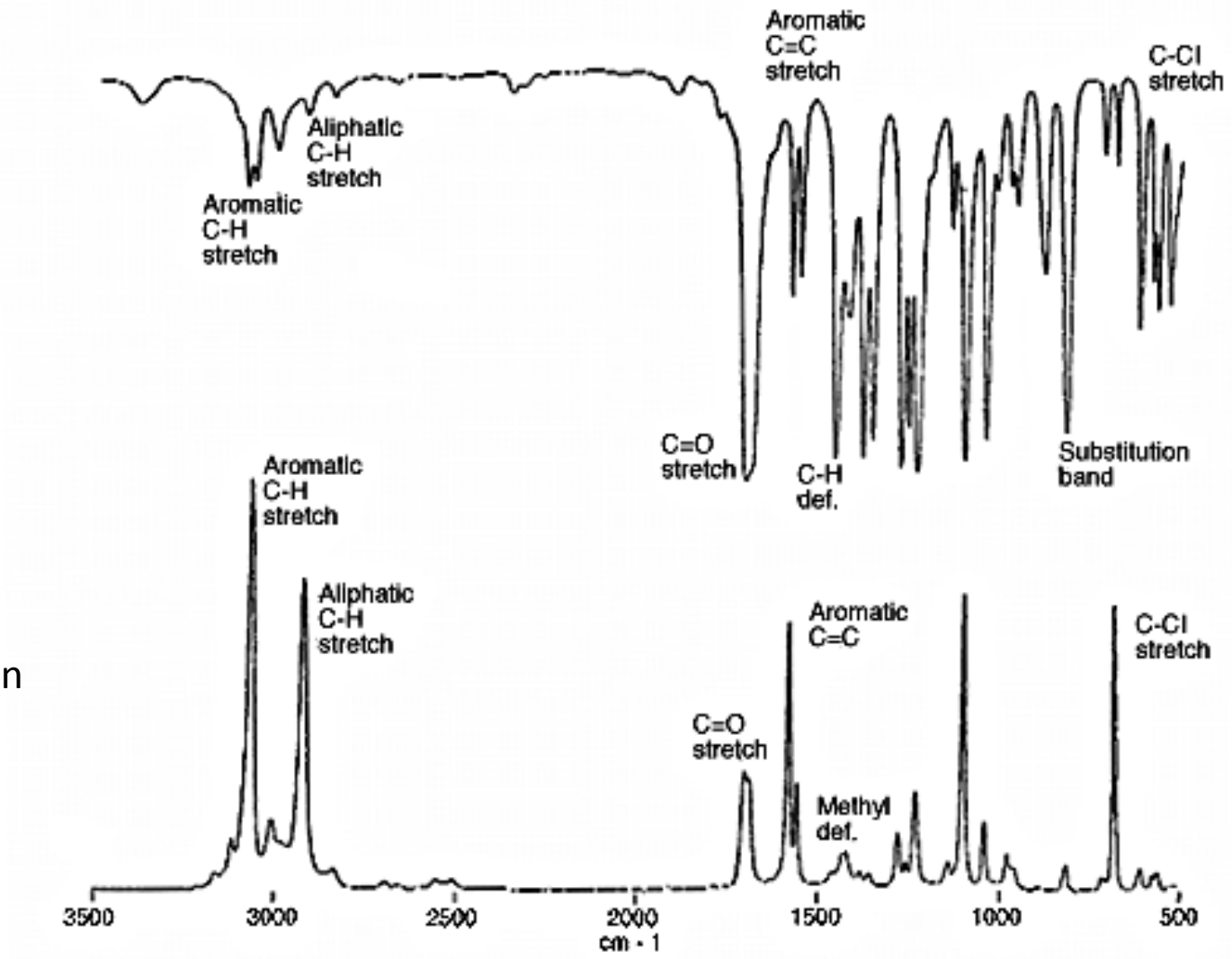

Infračervená spektrometrie (FTIR)

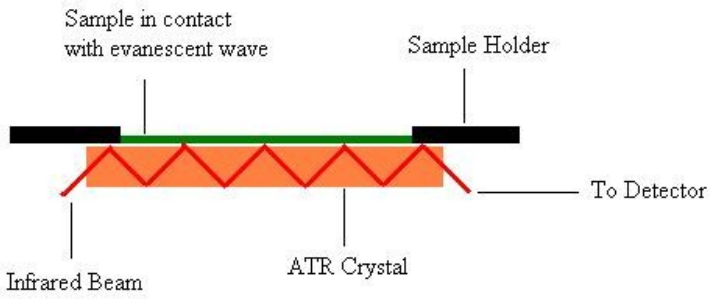

Schematic of a multiple reflection ATR system

ATR
KBr technika

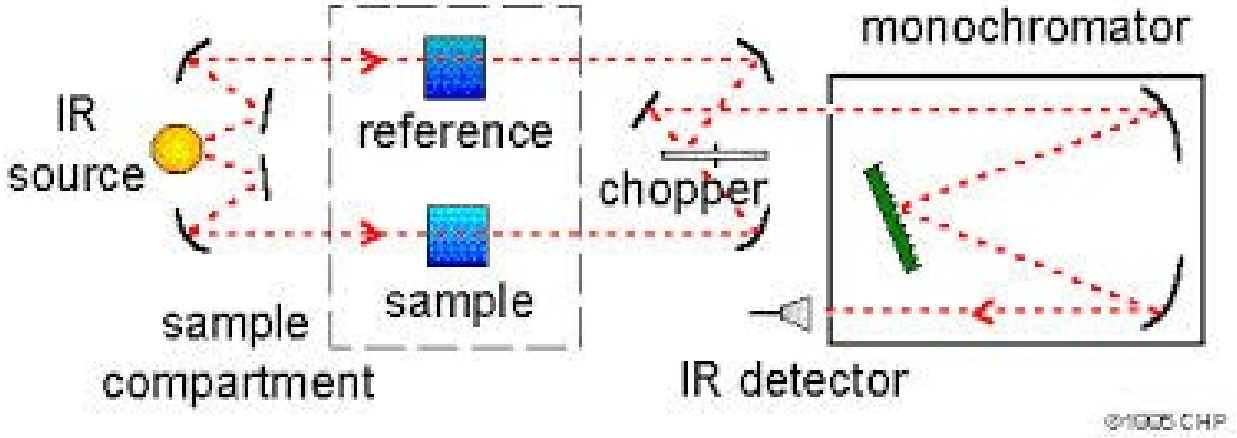

Fig. 1. The Delhi iron pillar before the construction of the iron grill cage around the stone platform.

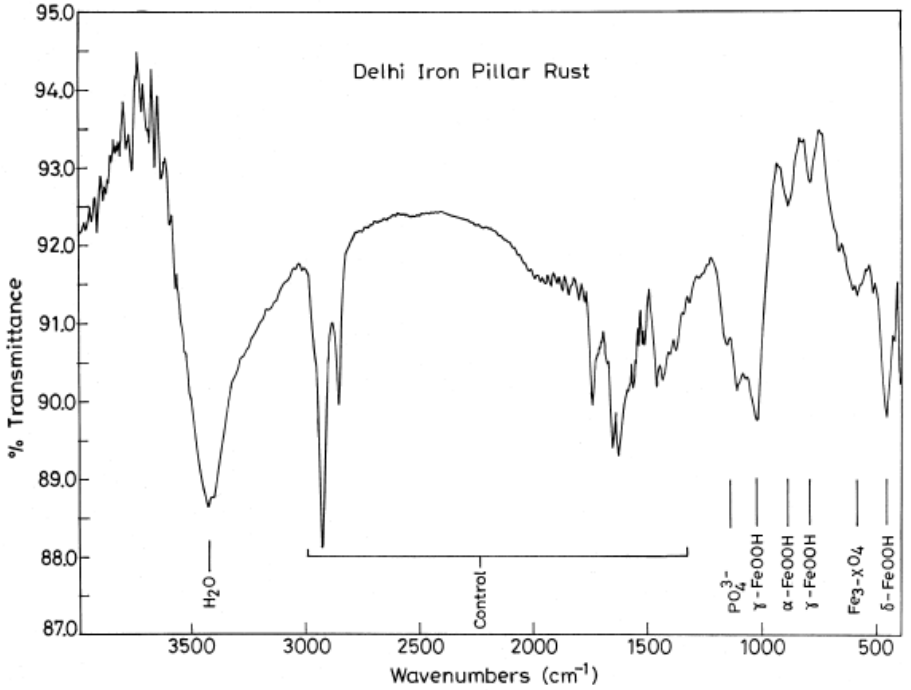

Fig. 5. FTIR spectrum from the DIP rust.

Skeletal remains from Dietrichstein tomb

Proof of presence of brushite on the bone samples from noble family Dietrichstein tomb.

Sample 1. Fragment of long bone of prince Ferdinand Josef

Sample 2. Fragment of skull of prince Leopold Ignác

Sample 3. Fragment of vertebra of prince Walter Xaver

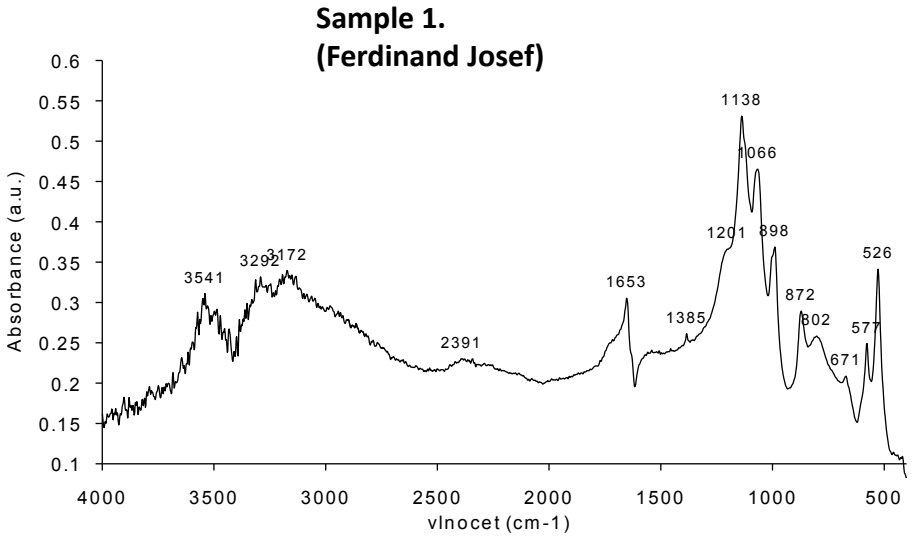
Sample 1.
(Ferdinand Josef)
Absorbance (a.u.)
vlnocet (cm-1)
3541
3292
3172
2391
1653
1385
1138
1066
1201
898
872
802
671
577
526

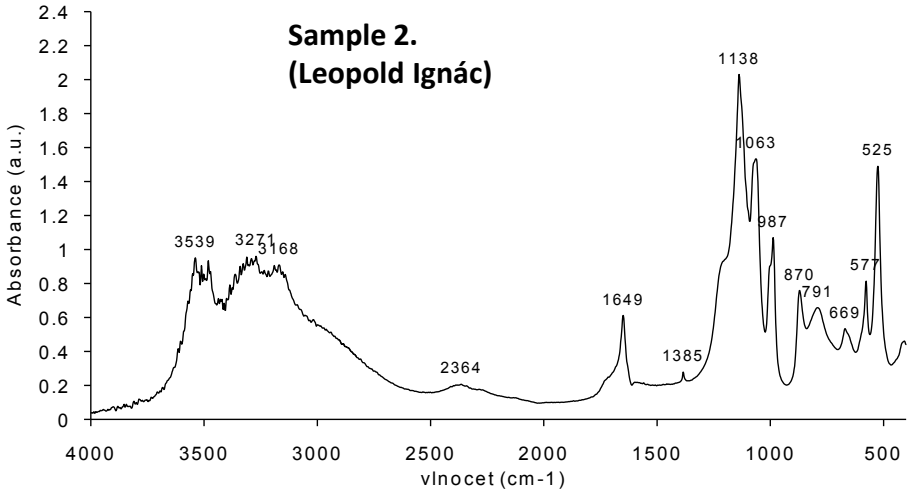
Sample 2.
(Leopold Ignác)
Absorbance (a.u.)
vlnocet (cm-1)
3539
3271
3168
2364
1649
1385
1138
1063
987
870
791
669
577
525

brushite

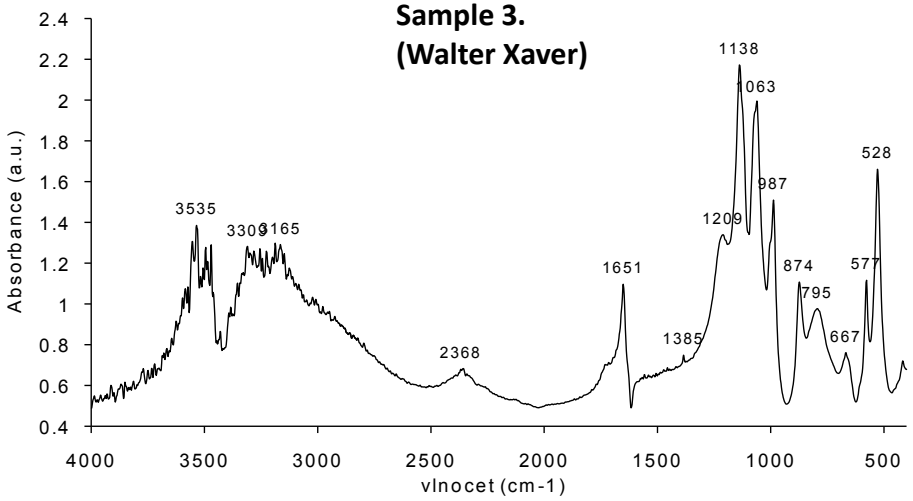
Sample 3.
(Walter Xaver)
Absorbance (a.u.)
vlnocet (cm-1)
3535
3309
3165
2368
1651
1385
1209
1138
1063
987
874
795
667
577
528

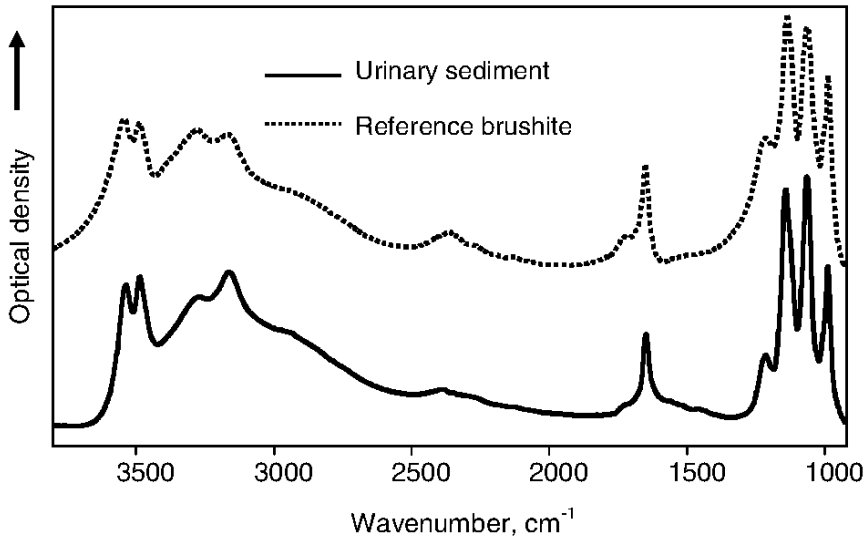
Urinary sediment
Reference brushite
Optical density
Wavenumber, cm-1

Cremation

Temperature (°C)	Color Effects
300	Black color of cortical bone
200–400	Ultrastructural orientation of collagen fibers is well preserved
600	Gray color indicates a leaching out of the organic portion
800	White color of bone

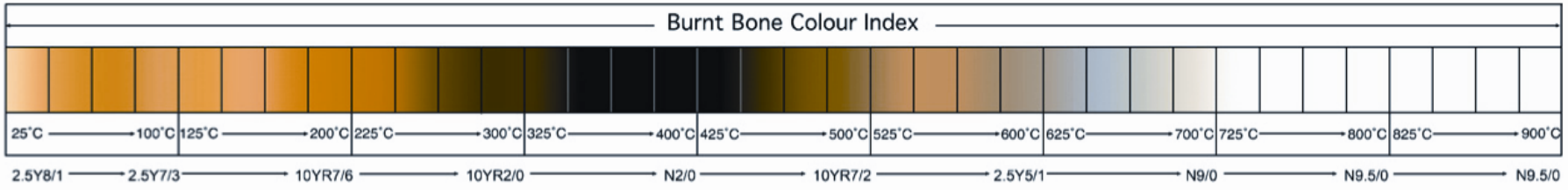

Bone Color (temp. °C)	Cortical Position	Crystal Morphology	Size Range	Lamellar Pattern	Collagen Fibers in Haversian Canal
White (800–1400)	Outer	Spherical and Hexagonal	0.25 ± 0.07 μm to 0.41 ± 0.09 μm	Not observable	Indistinguishable
Gray (~600)	Mid-cortex	Spherical	~0.060 ± 0.007 μm	Not observable	Fraying
Black (200–600)	Inner	No crystals	–	Observable	No Fraying

Závislost tvaru IR pásů na teplotě kremace

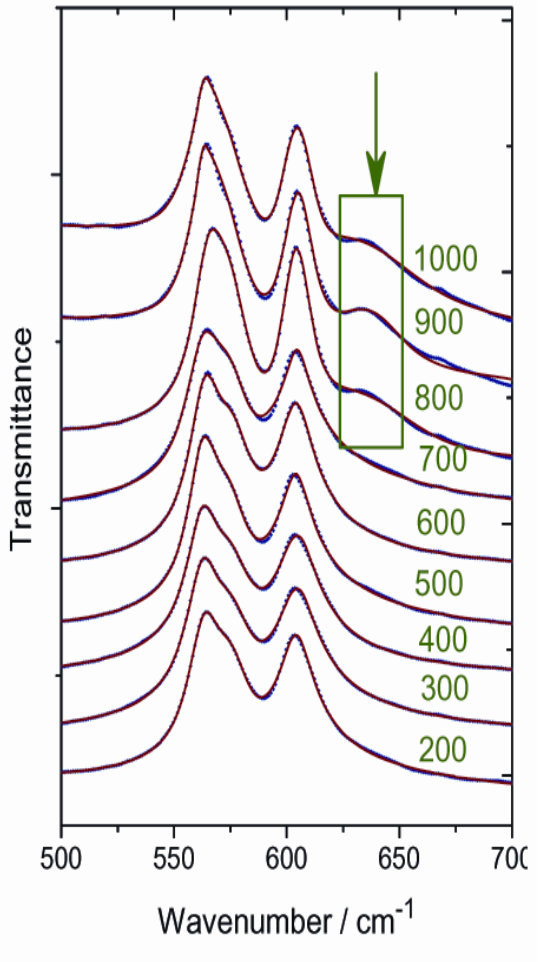

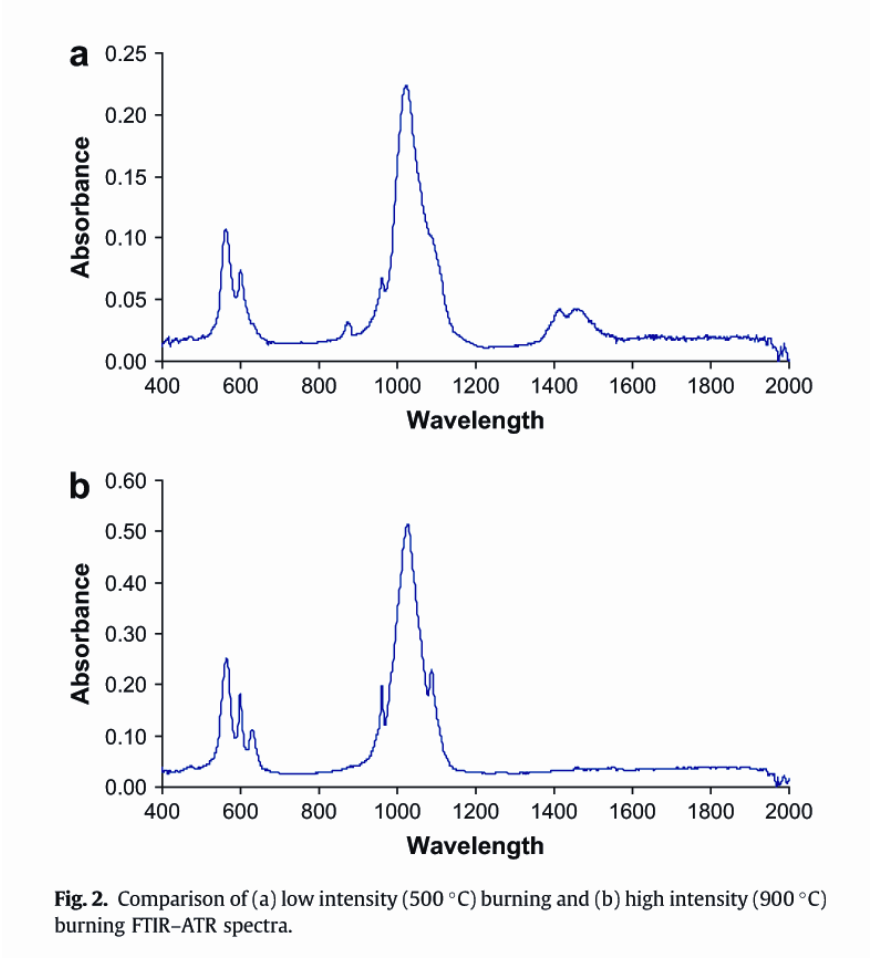

Fig. 2. Comparison of (a) low intensity (500 °C) burning and (b) high intensity (900 °C) burning FTIR–ATR spectra.

Příbor, mladší doba bronzová

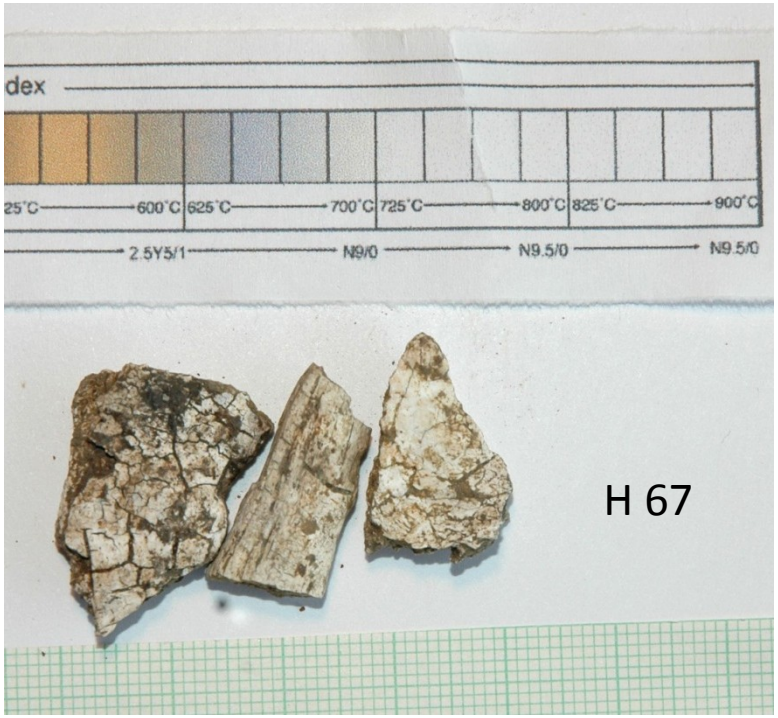

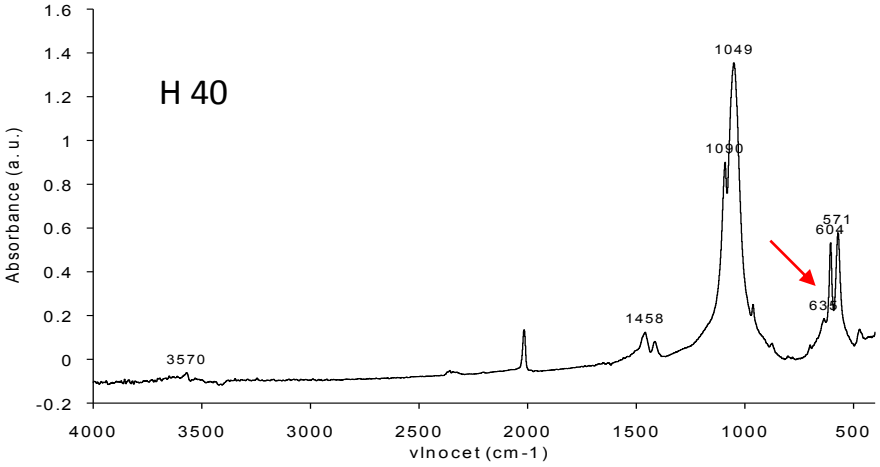
H 40
Absorbance (a. u.)
vInocet (cm-1)
3570
1458
1090
1049
635
604
571

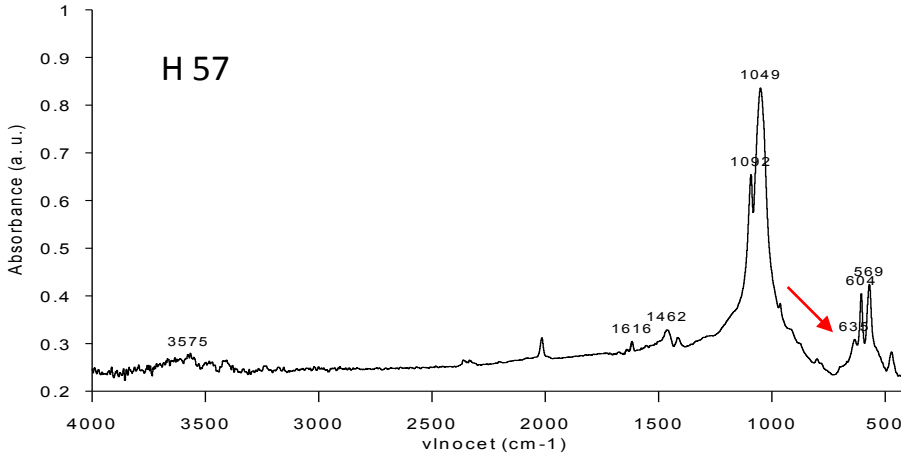
H 57
Absorbance (a. u.)
vInocet (cm-1)
3575
1616
1462
1092
1049
635
604
569

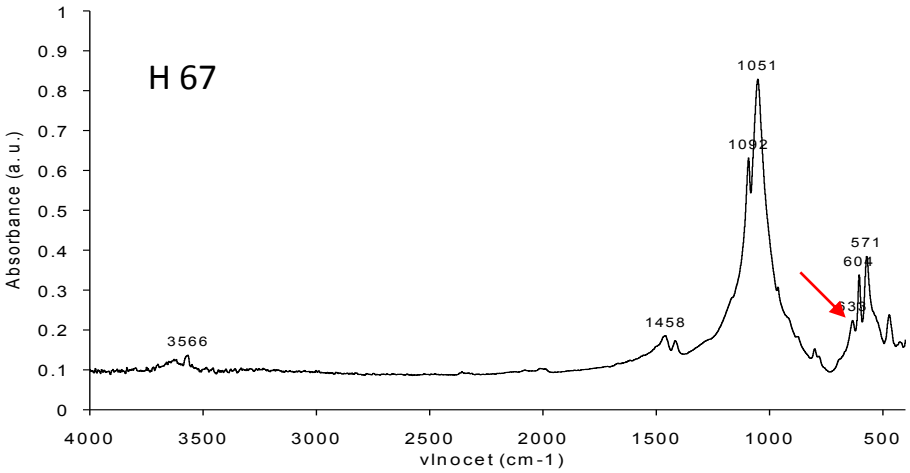
H 67
Absorbance (a. u.)
vInocet (cm-1)
3566
1458
1092
1051
635
604
571

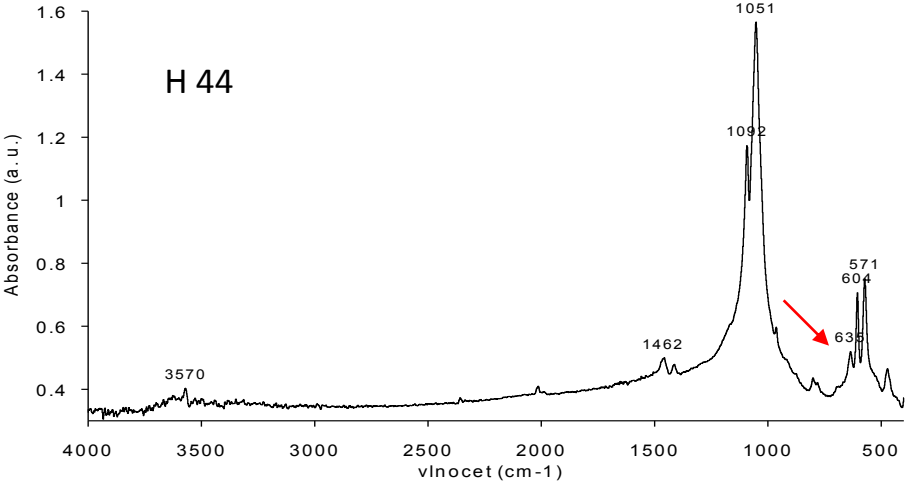
H 44
Absorbance (a. u.)
vInocet (cm-1)
3570
1462
1092
1051
635
604
571

Egyptská kniha mrtvých

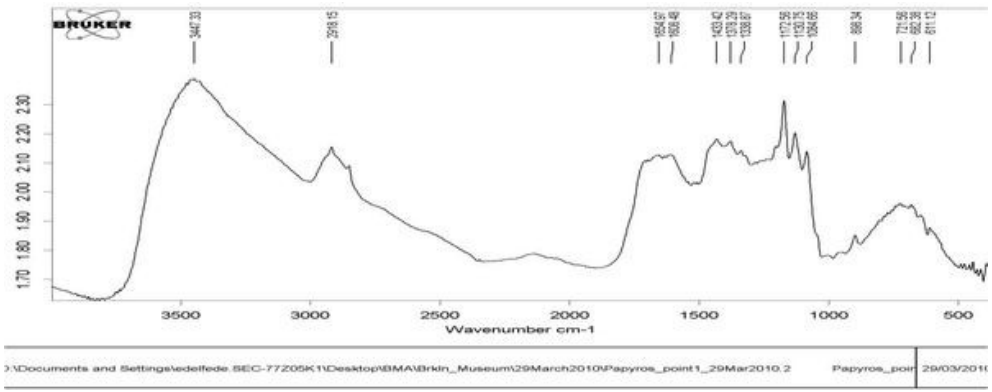

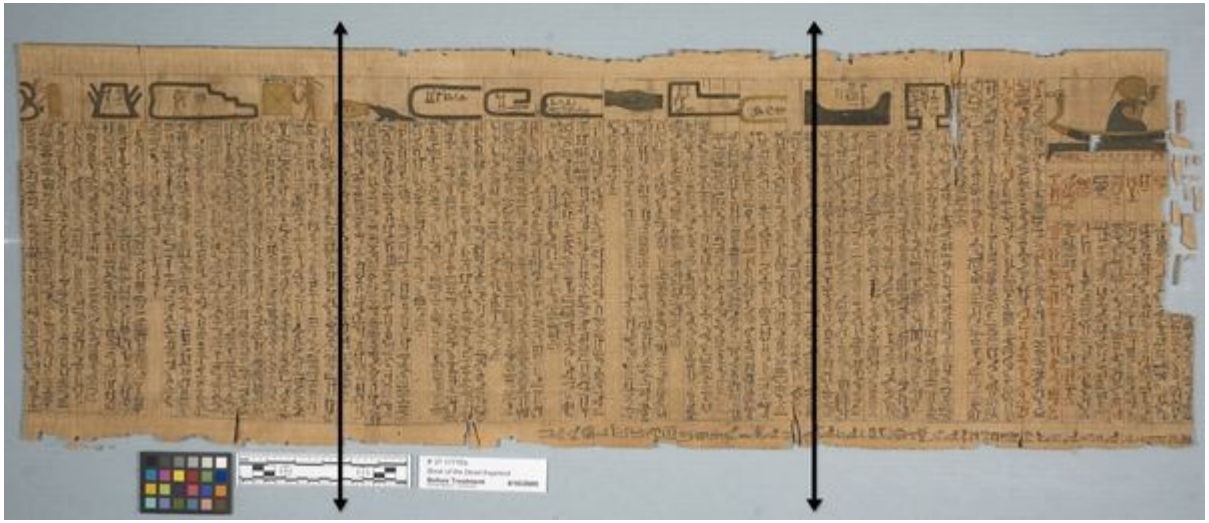

Přenosné FTIR zařízení

Odraz záření

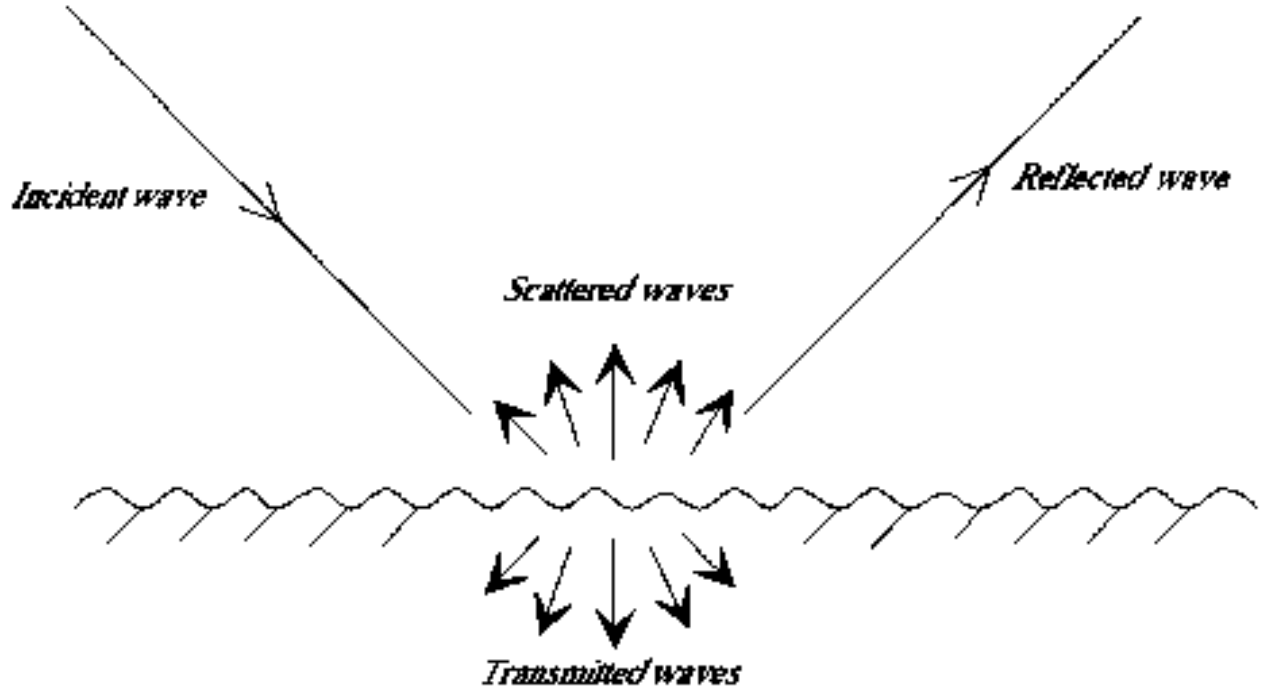

Figure 15. Case of natural environments: sum of specular reflection and diffuse reflection (volume reflection is ignored here).

Reflektografie

Aplikace infračervené reflektografie - zviditelnění podkresby

Reflektografie

Aplikace infračervené reflektografie - zviditelnění tetování na mumifikovaných rukou z pohřebiště Semna South, Núbie (dnešní Súdán), stáří cca 2000 let.

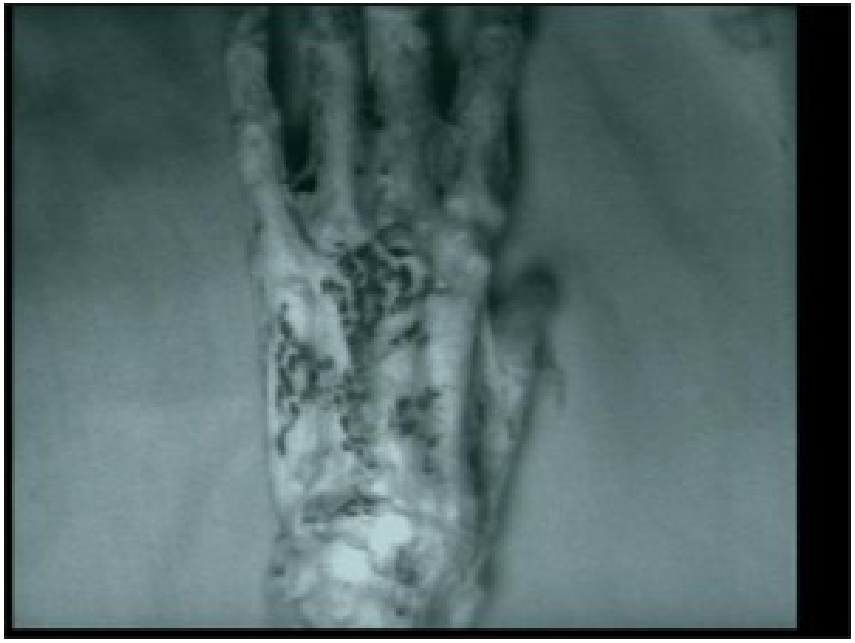

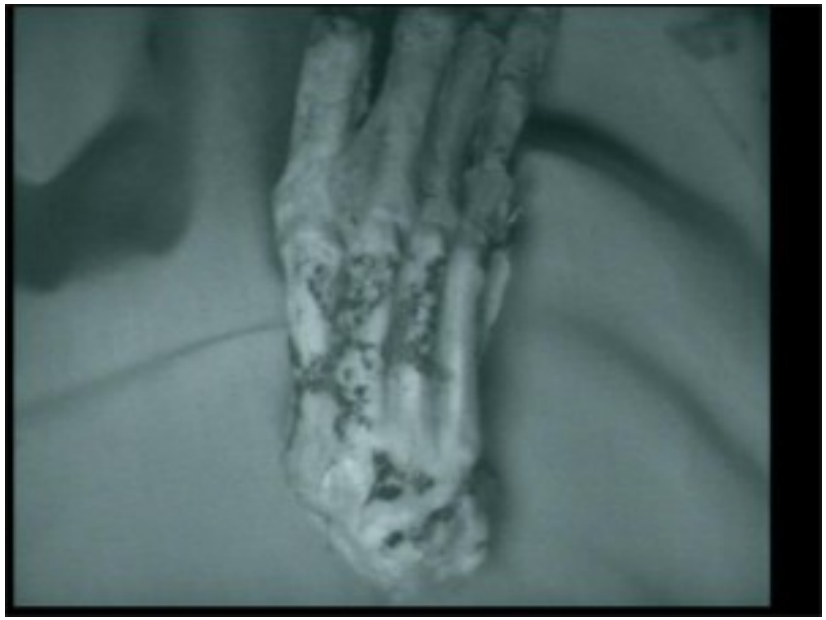

Precipitace v tekutém prostředí:

Nefelometrie

-hodí se pro nižší koncentrace

viditelné světlo

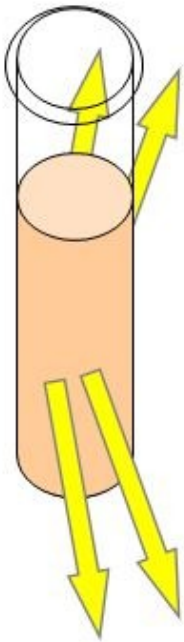

detektor je ve směru kolmém na vstupující paprsek

měří množství světla rozptýleného při průchodu paprsku
(množství světla odraženého od vznikajících komplexů)

Turbidimetrie

- hodí se pro koncentrovanější roztoky

viditelné světlo

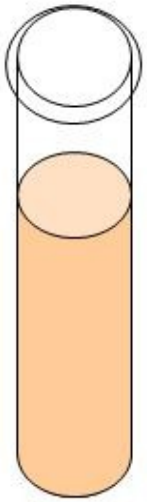

detektor je v ose paprsku

měří množství procházejícího světla (úbytek intenzity světla, které prošlo roztokem v kyvetě)

nefelometrie je 5-10x **citlivější** a **nákladnější** než turbidimetrie

Ramanova spektrometrie

Nd:YAG 1064 nm
He–Ne 632.8 nm

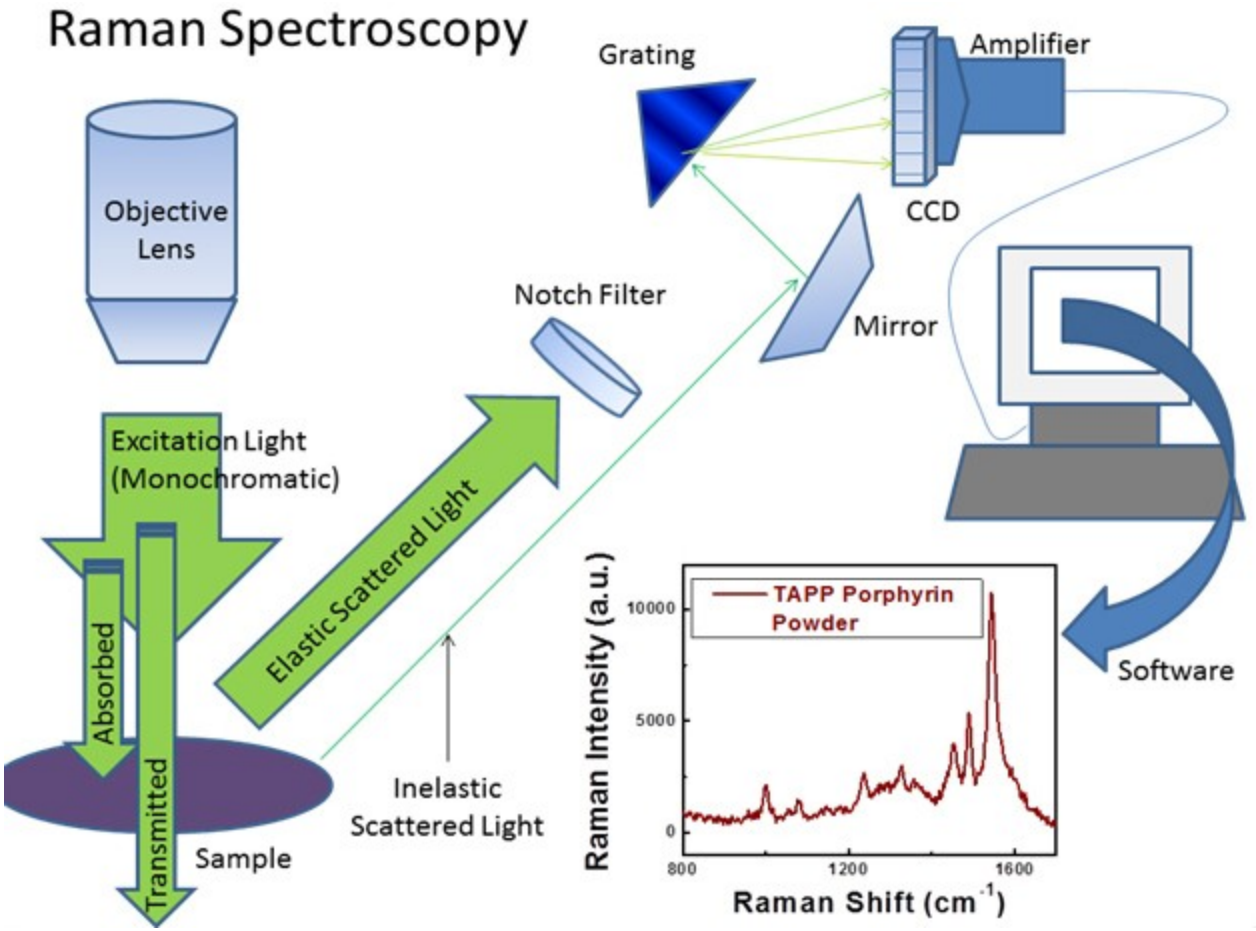

Princip Ramanovy spektrometrie

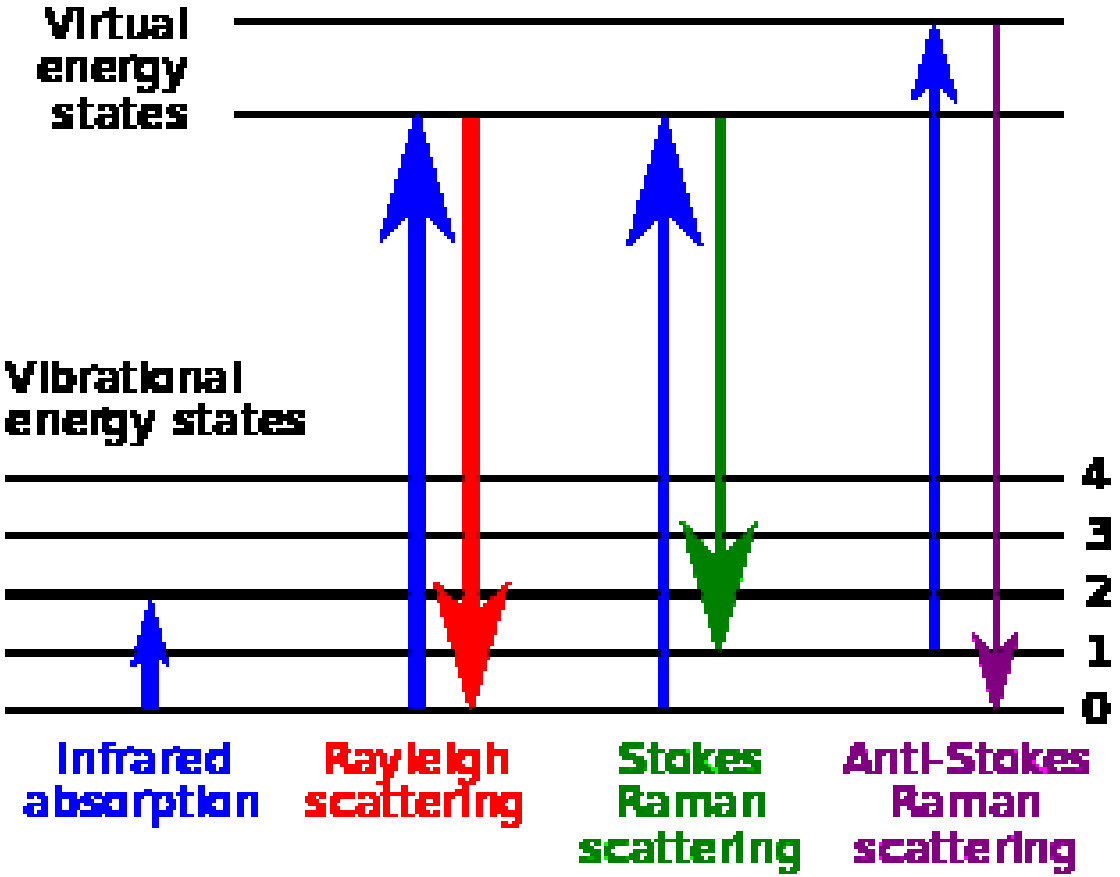

Raman vs. FTIR

FT IR

(FT) Raman

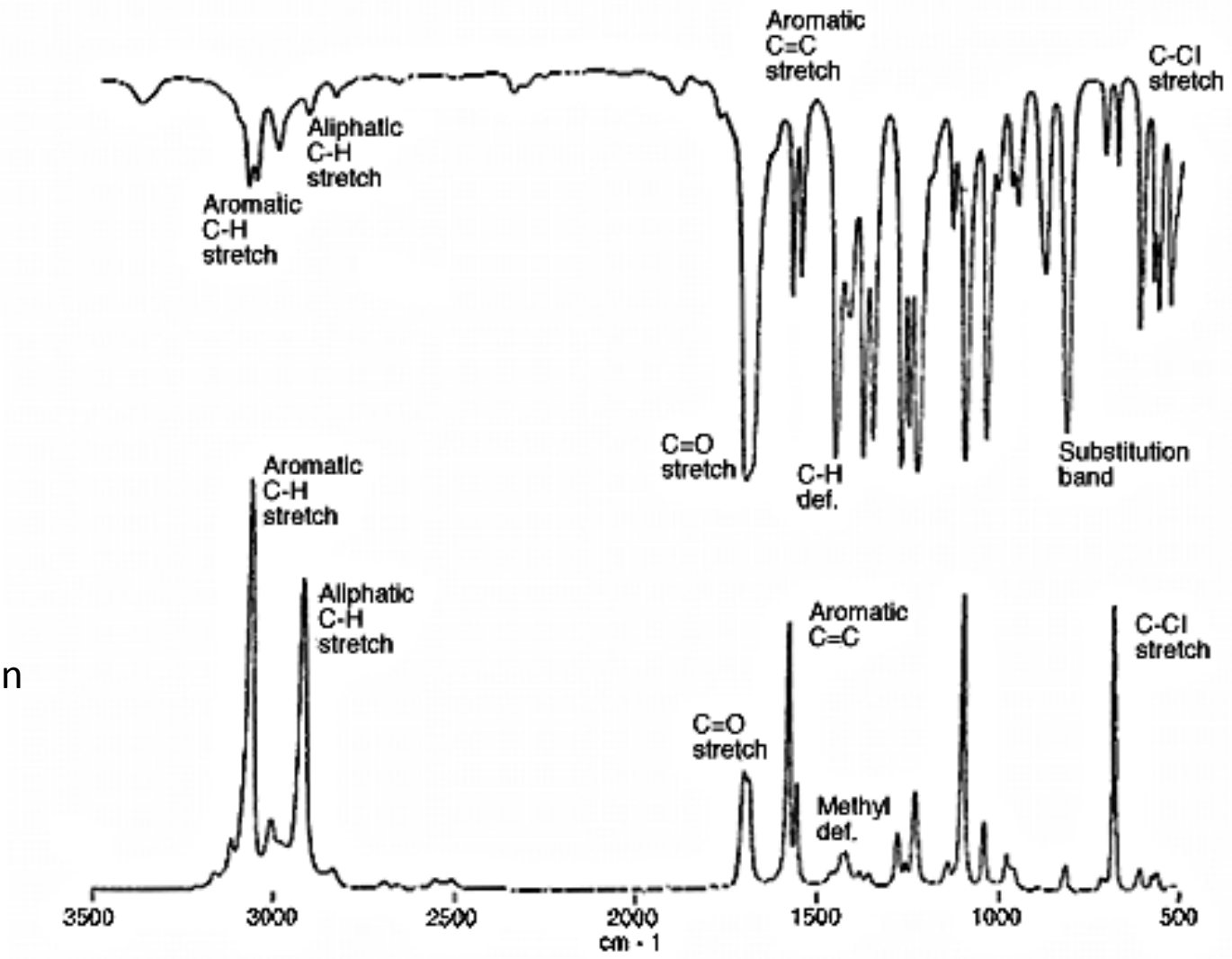

Analýza zubů

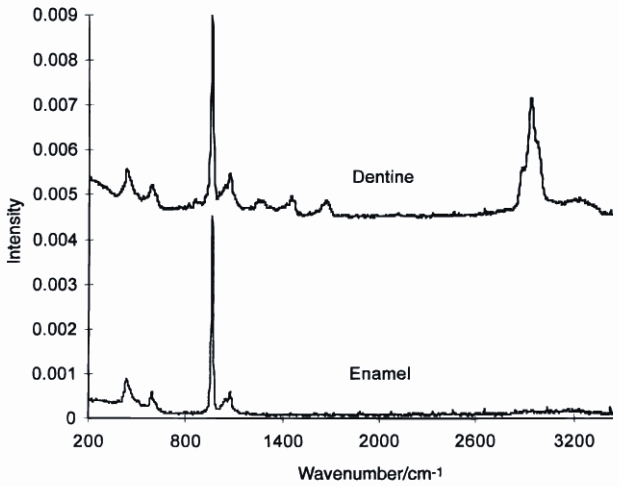

Figure 1. Typical FT-Raman spectra of human tooth enamel a dentine of a transverse section of a human tooth. 1064 nm exc tion; 4 cm^{-1}; 120 mW power; 4000 scans.

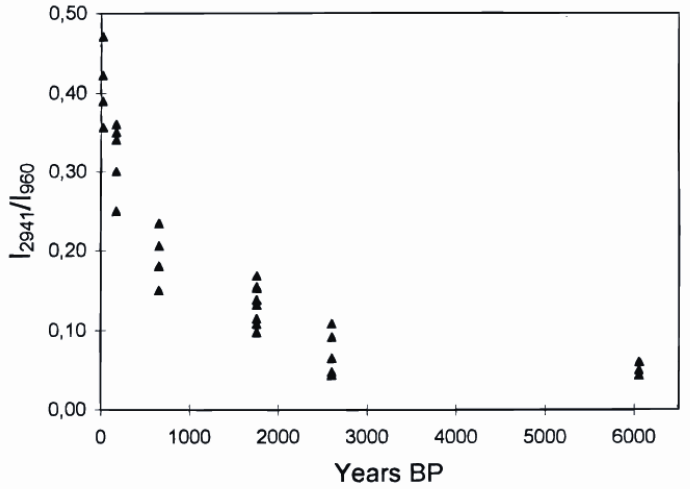

Figure 4. I_{2941}/I_{960} relative intensities as a function of the tooth burial period.

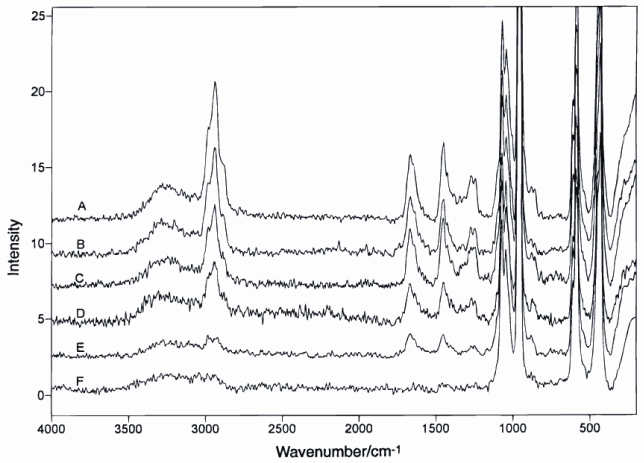

Figure 3. FT-Raman external enamel normalized spectra of the teeth examined: (A) Bologna, Italy, 0 BP; (B) Sassari, Italy, 150 BP; (C) S. Agata, Ravenna, Italy, 650 BP; (D) Bagnacavallo, Italy, 1700 BP; (E) Monte Casasia, Italy, 2700 BP; (F) Passo di Corvo, Foggia, Italy, 5800–6300 BP.

Analýza mumifikovaných tkání

FT-Raman spektra

(a) současná lidská kůže (stratum corneum),
(b) stratum corneum ledovcového muže Ötziho,
(c) peruánská světle-pigmentovaná mumie,
(d) grónská mumie (30-letá žena)
(e) peruánská tmavě-pigmentovaná mumie.

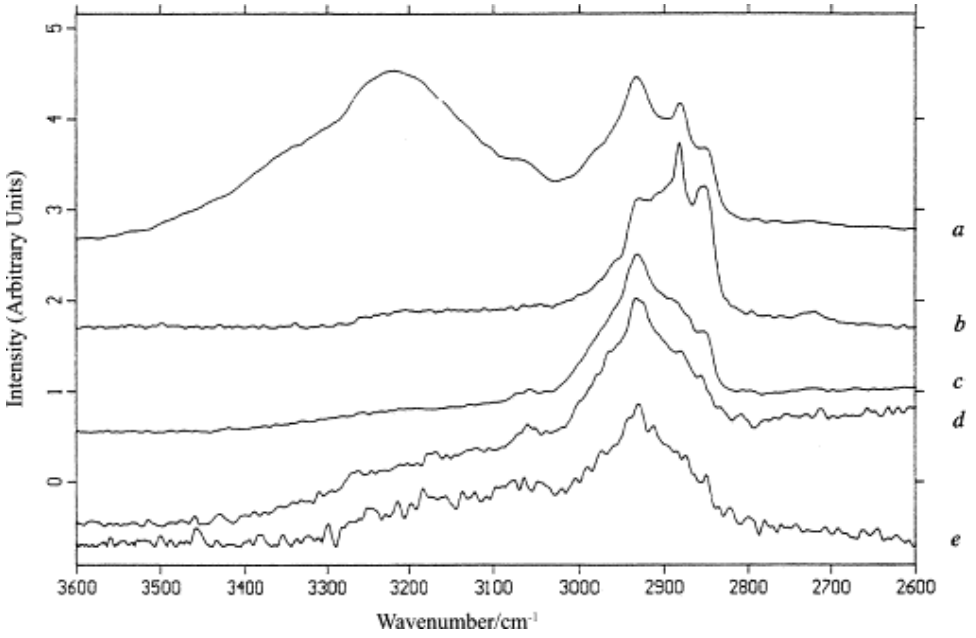

FT-Raman spektra

moderní dětský nehet (nahoře)
nehet mumifikovaného dítěte (Grónsko) (dole)

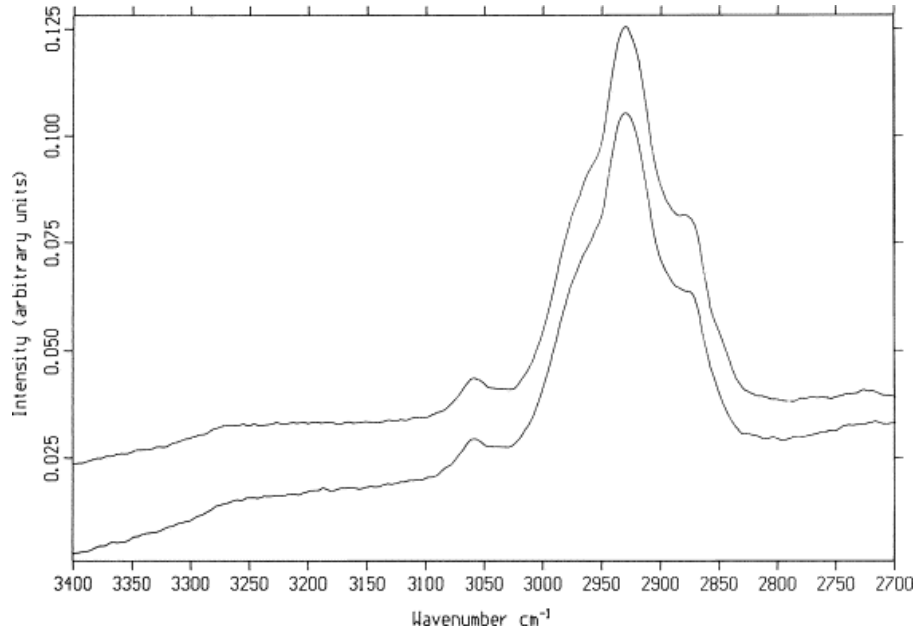

Ramanova spektrometrie pigmentů

Polychromovaná socha sv. Anny v Santa Maria la Real, Sasamon, Španělsko (13. stol.).

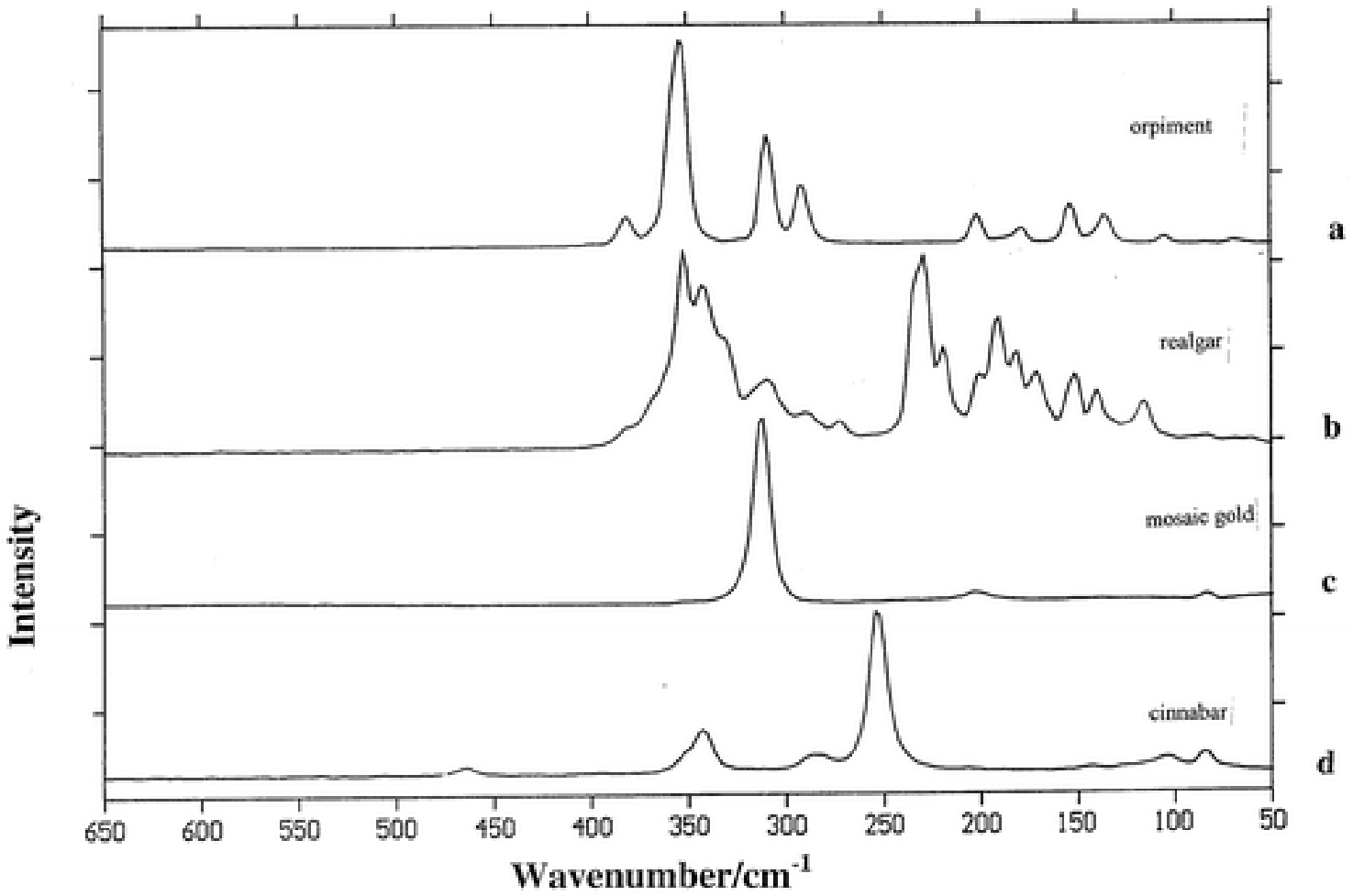

Ramanova spektra auripigmentu (As_2S_3), realgaru (As_4S_4), mozaikového zlata (SnS_2) a rumělky (Hg S).

Oltář ze “San Antolín y San Bernabé”

Pigment	*Chemical formula*	*Raman bands cm^{-1}*
Vermilion	HgS	255, 309, 347, 376
Azurite	$2CuCO_3 \cdot Cu(OH)_2$	251, 404, 623, 770, 838, 1098
Malachite	$CuCO_3 \cdot Cu(OH)_2$	153, 168, 179, 223, 272, 352, 435, 516, 538, 722, 755, 1062, 1100, 1372, 1496
Lead White	$PbCO_3$	409, 1054
Lapislazuli	$Na_8[Al_6Si_6O_{24}]S_n$	258, 286, 545, 581, 802, 1097, 1358, 1642
Massicot	PbO	286, 384, 419
Gypsum	$CaSO_4 \cdot 2H_2O$	182, 216, 416, 495, 623, 673, 1009, 1140

Table 1. Chemical formula and Raman band observed (in cm^{-1}, wavenumber) of the identified pigments.

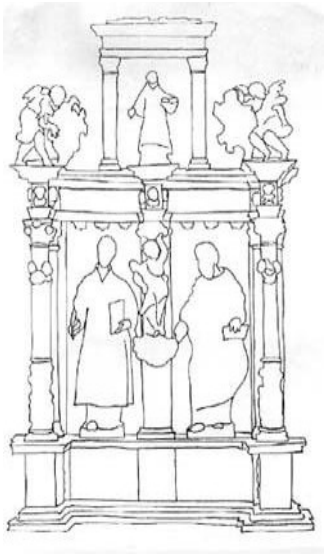

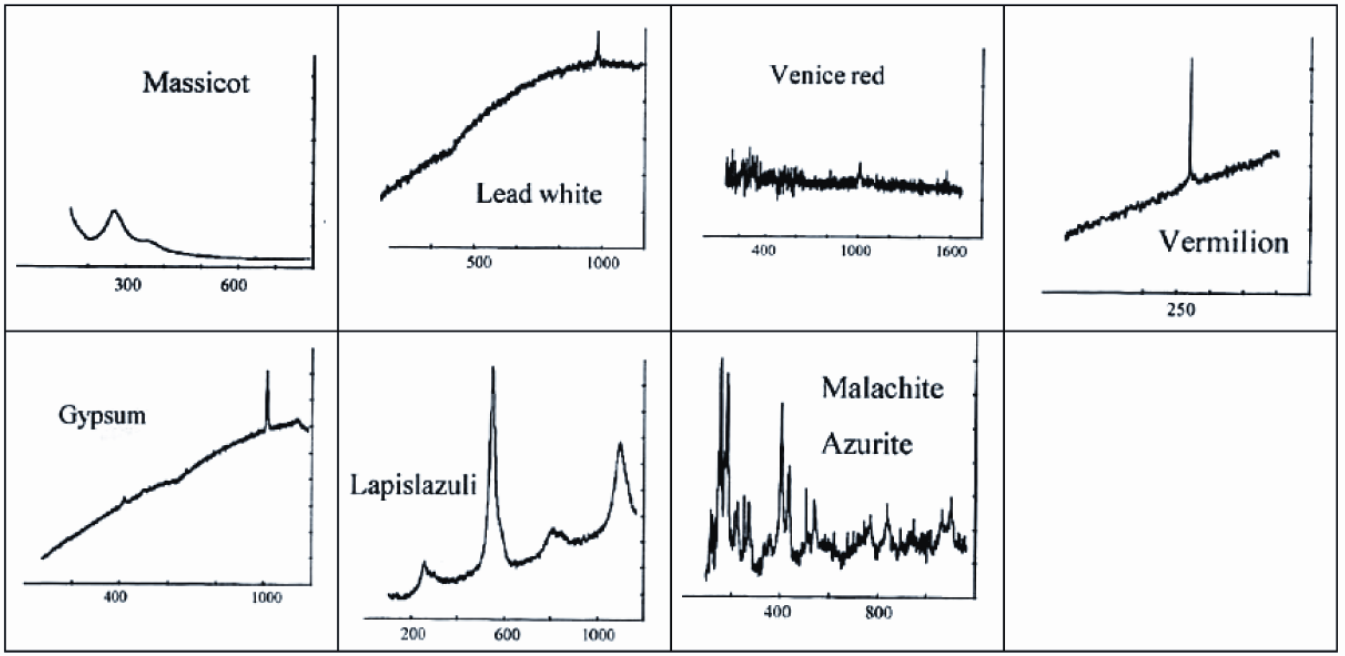

Fig. 5. The Raman spectra of the pictorial materials obtained from the “San Antolín y San Bernabé” altarpiece. The axis are Raman intensity and wavenumber (cm^{-1}).

Rozpoznání imitací

Přírodní barevné korály (karoten)

Barvené korály

Imitace korálů

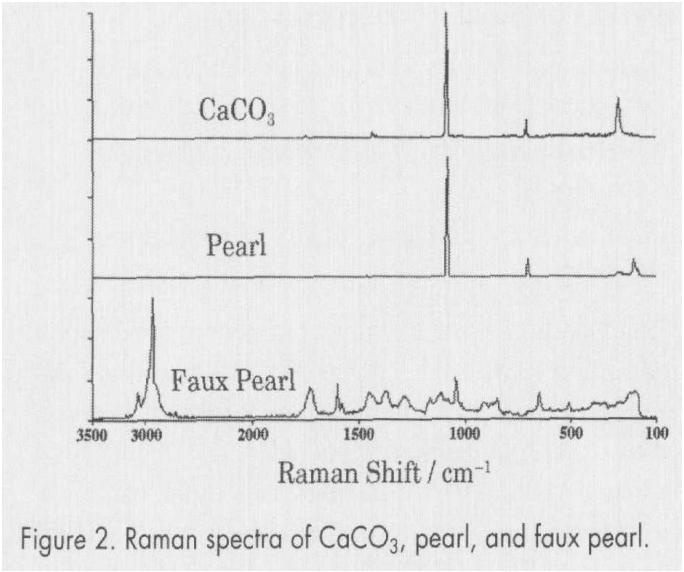

Figure 2. Raman spectra of $CaCO_3$, pearl, and faux pearl.

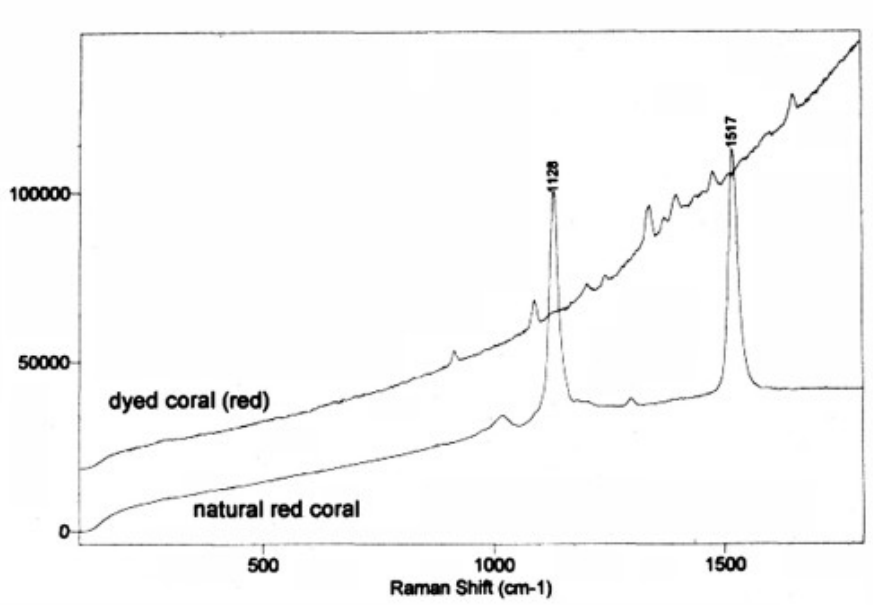

Identifikace slonoviny

FT-Ramanova spektra:

Římské pečetidlo (i)

africký slon (ii),

vorvaň (iii)

hroch (iv)

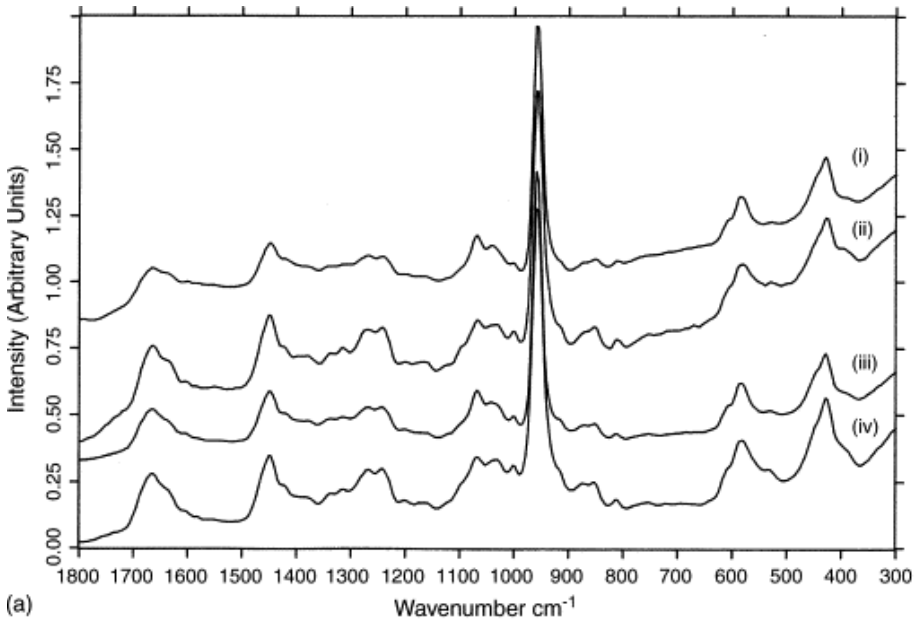

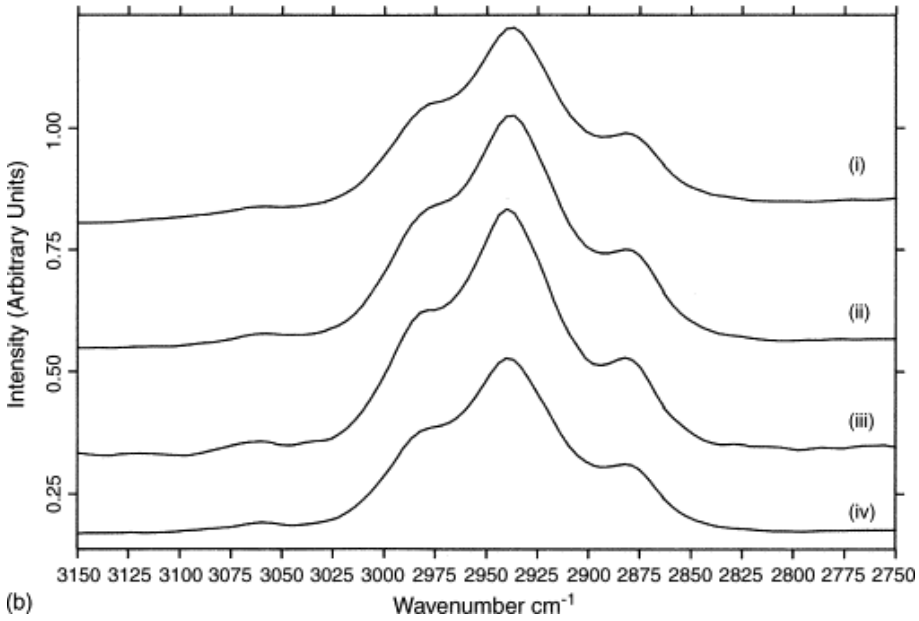

Korozní produkty

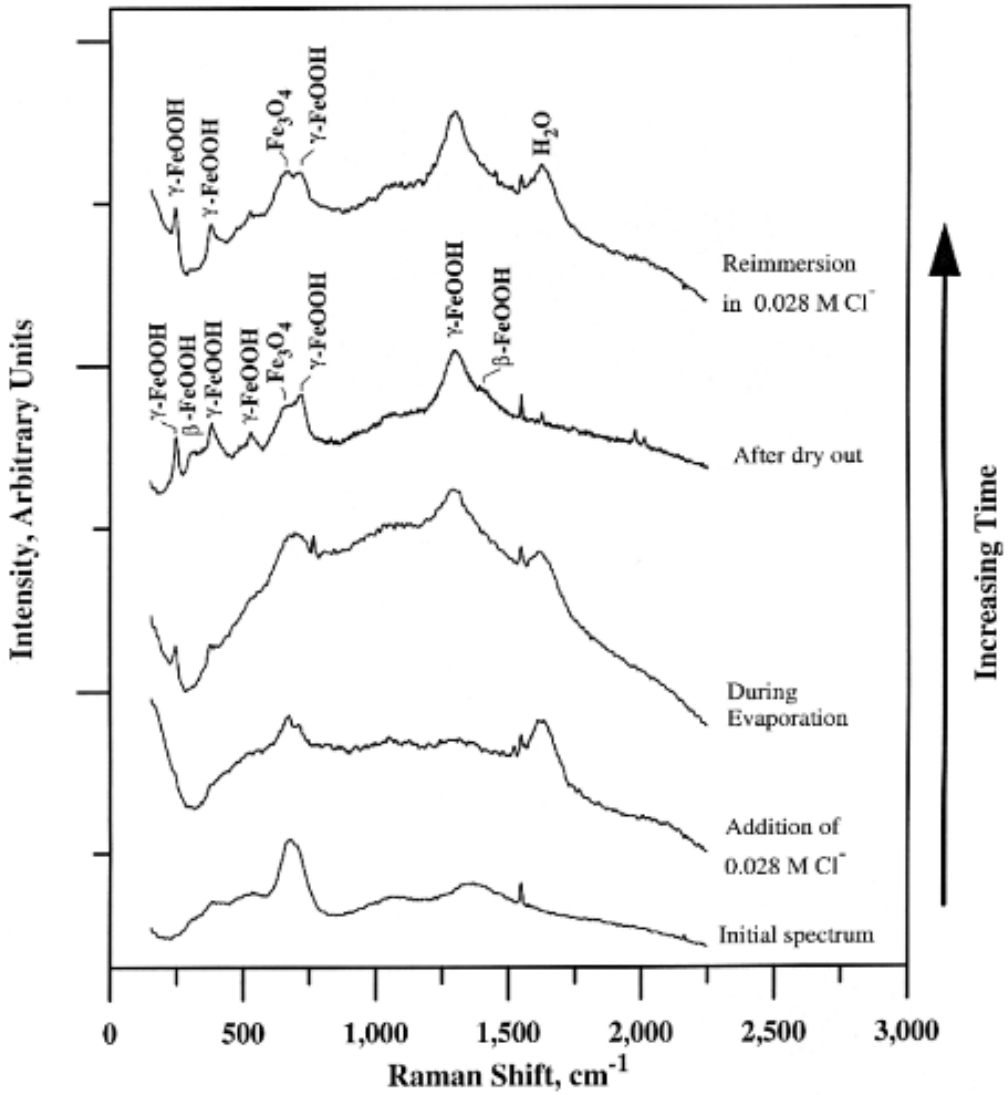

Kombinace Raman + LIBS

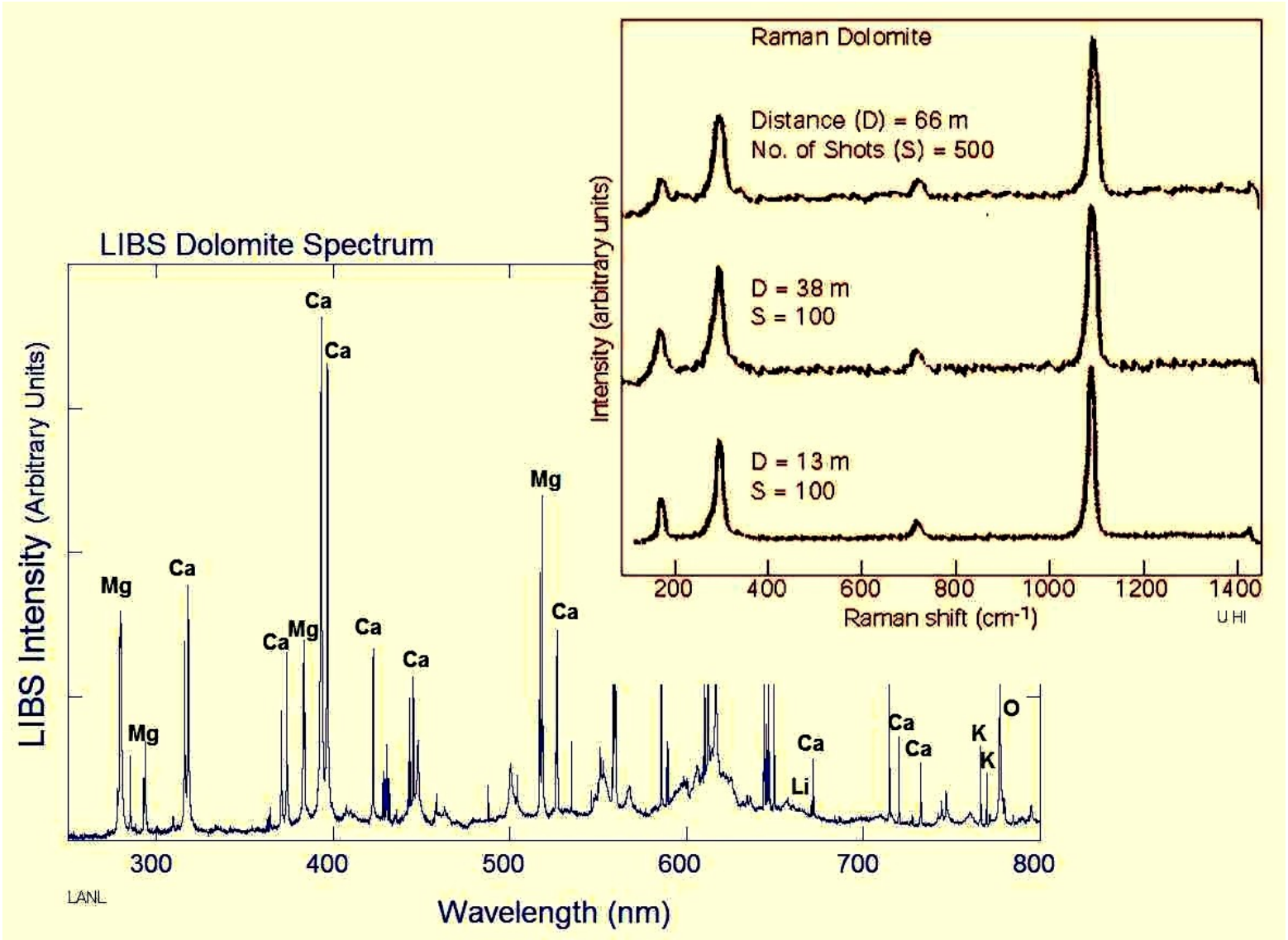

Mobilní zařízení pro Ramanovu spektrometrii

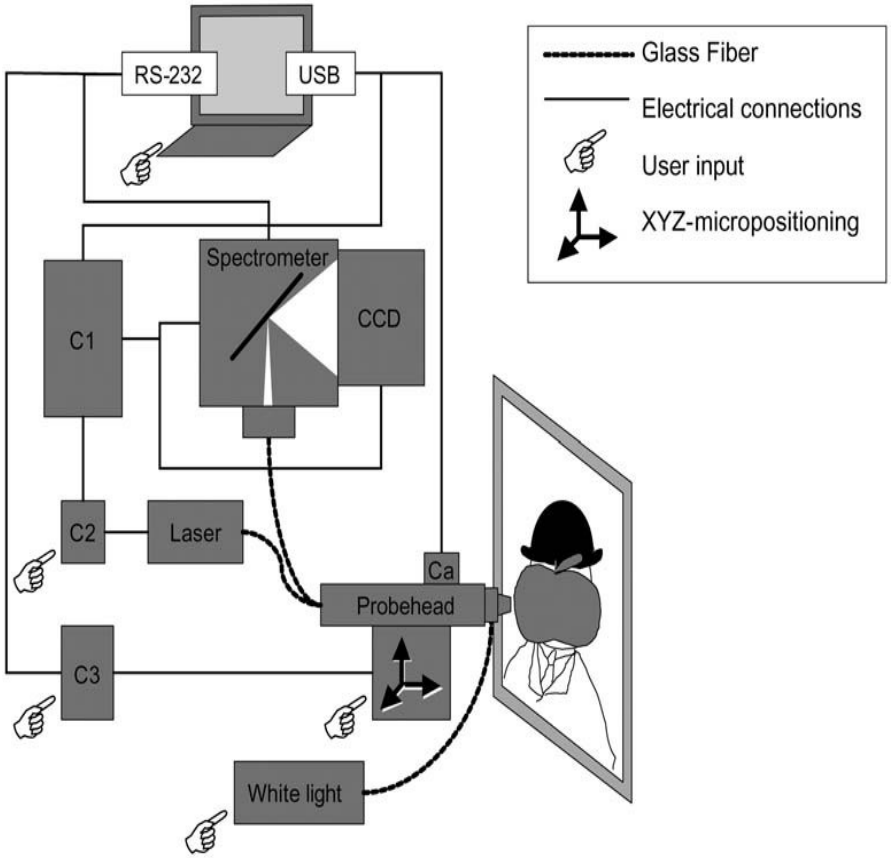

M : 95% propustné zrcadlo pro vizualizaci plochy kamerou (*Ca*).

HNF : holografické filtry odrážející laserový paprsek a propouští ramanovsky posunuté záření (Stokes)

F filtry pro anti-Stokesovskou část spektra

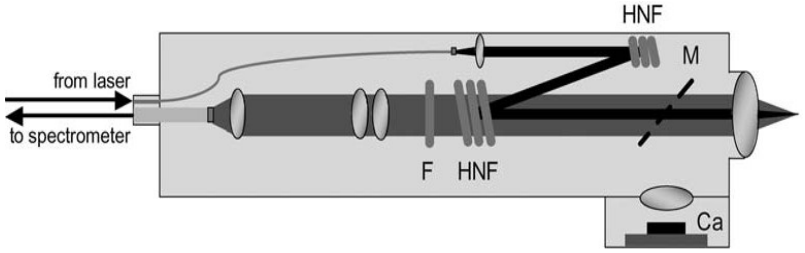

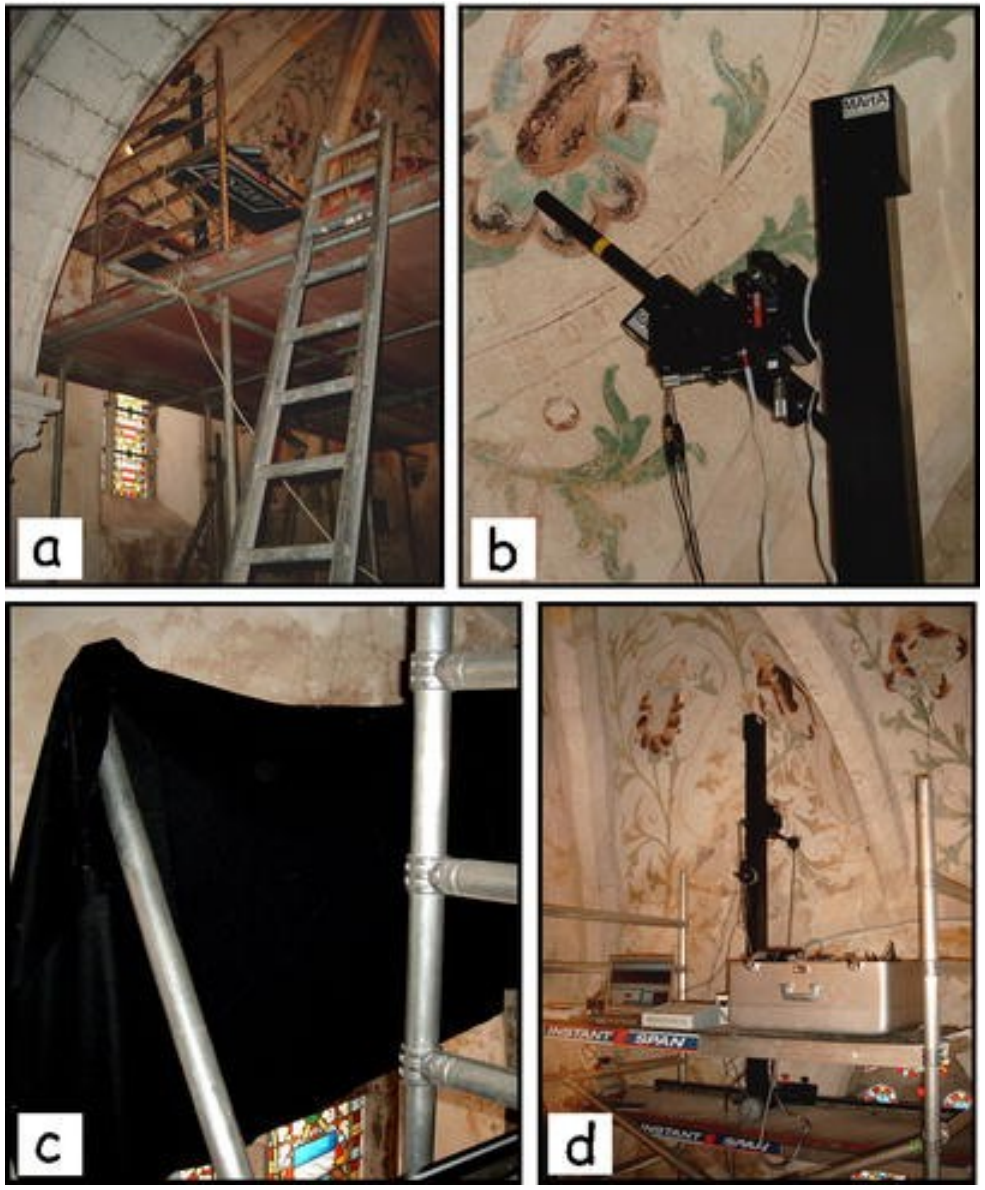

Analýza nástěnných maleb (kaple Ponthoz.)

Analýza povrchů

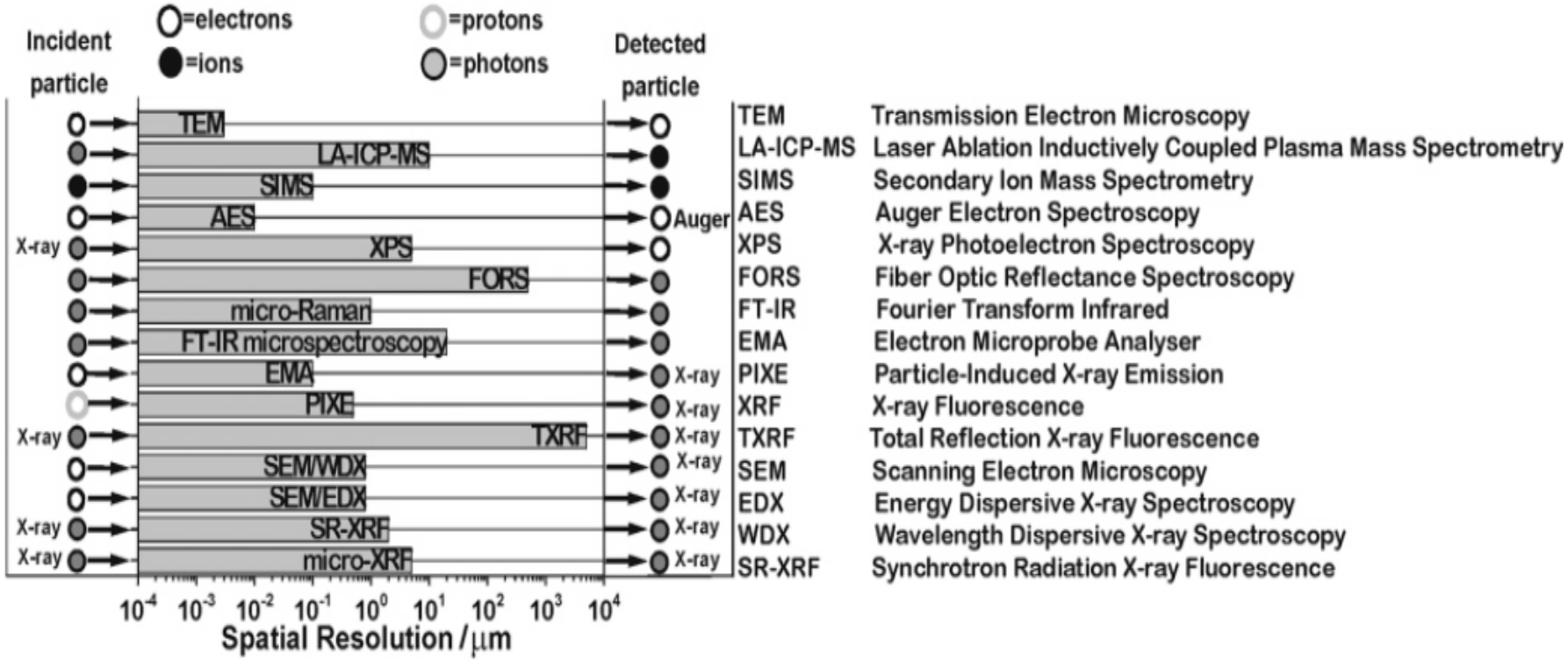

Fig. 1 Typical spatial resolution of a variety analytical techniques. The probed and detected particles are also shown.

Optická mikroskopie

V průchozím světle

V odraženém světle

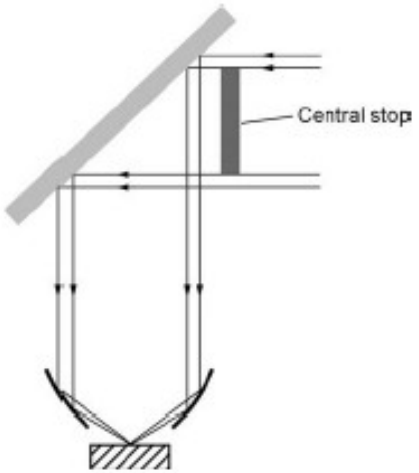

Figure 1.29 Dark-field illumination in a reflected light microscope.

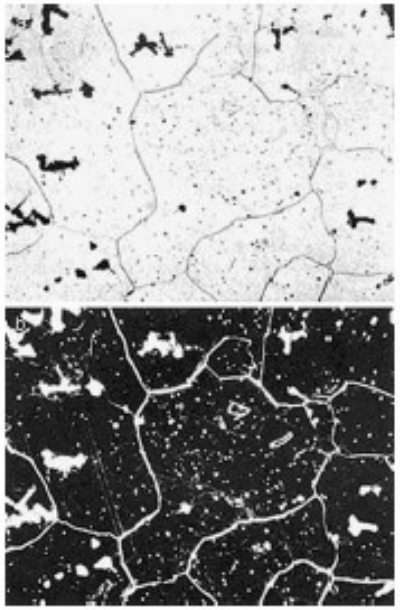

Figure 1.30 Comparison between: (a) bright-field; and (b) dark-field images of AISI 1080 hig carbon steel. In addition to grain boundaries and oxide particles, annealing twins are revealed the dark-field image. (Reproduced with permission of ASM International®. All Rights Reserve www.asminternational.org. G.F. Vander Voort, *Metallography Principles and Practice*, McGraw-Hi New York. © 1984 ASM International®.)

Figure 12. Relationship between single-phase structures in FCC metals used in antiquity.

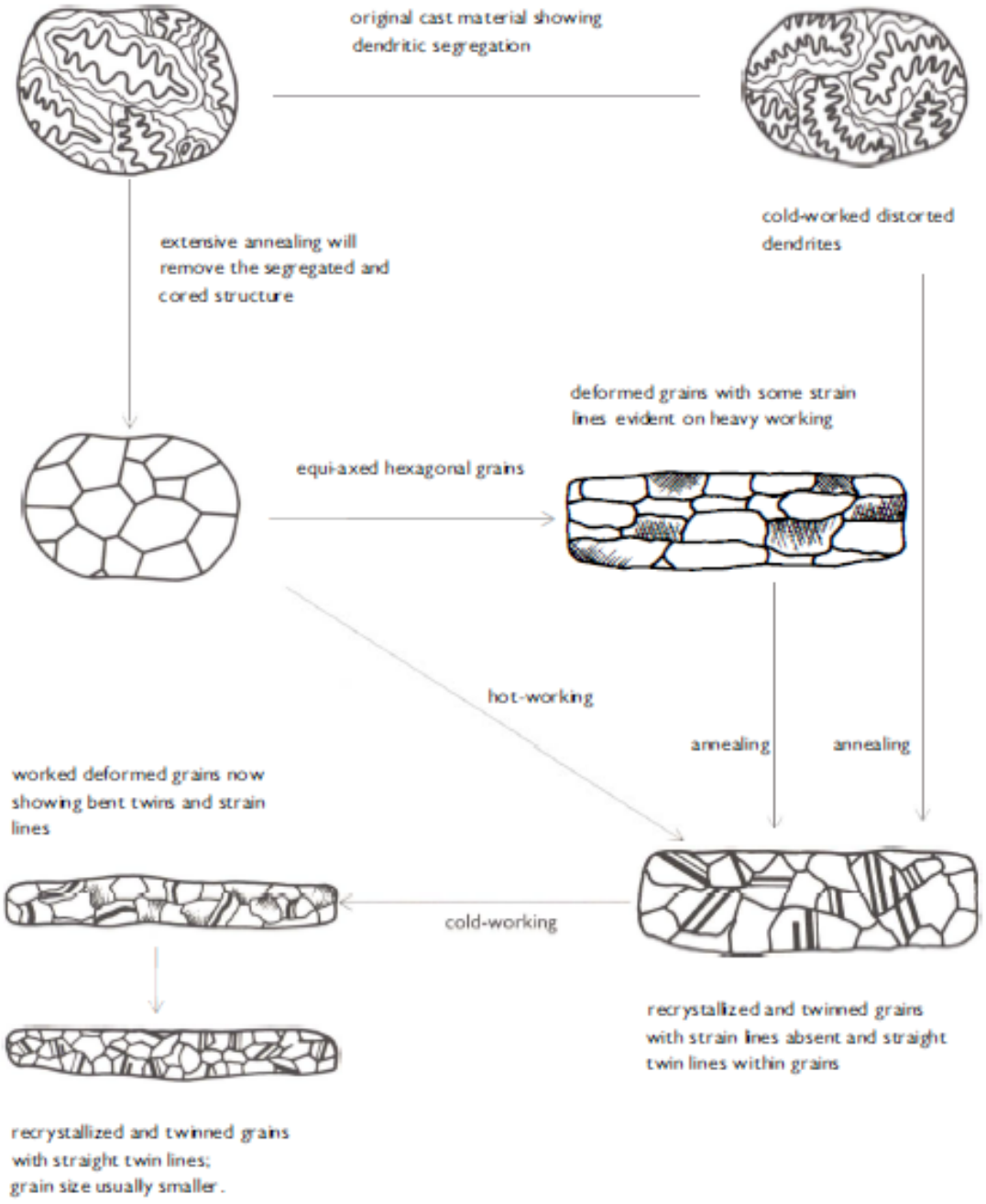

Mikroskopie v polarizovaném světle

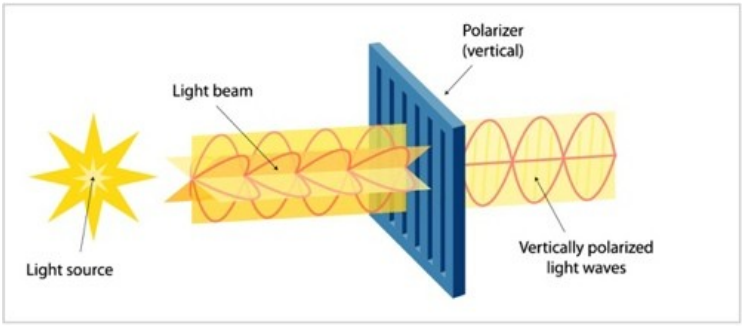

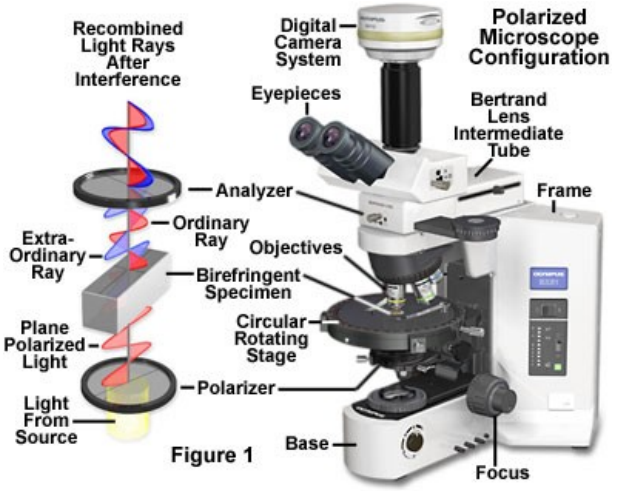

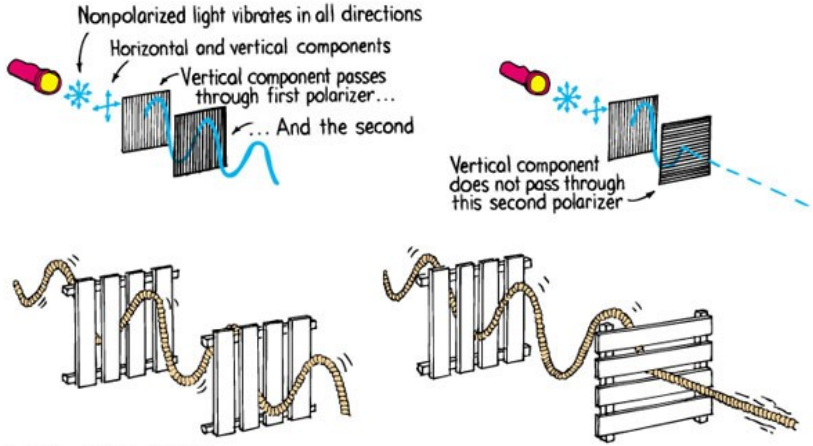

Hewitt, *Conceptual Physics*, Ninth Edition.

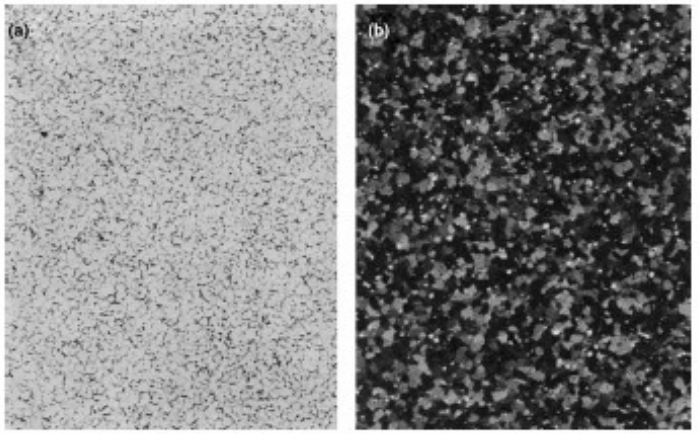

Figure 1.38 Example of using polarized-light microscopy for pure titanium specimen: (a) bright-field image; and (b) polarized light image in which grains are revealed. (Reproduced from G.F. Vander Voort, *Metallography Principles and Practice*, McGraw-Hill, New York. © N. Gendron, General Electric Co.)

Elektronová mikrosonda

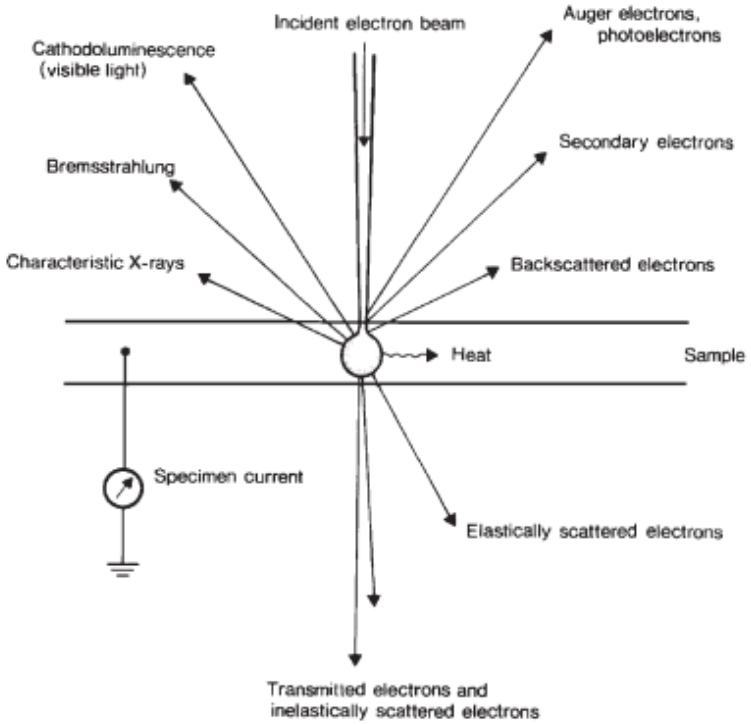

Figure 2.12 Interaction of primary electrons with a thin solid sample, showing the various processes which can take place. (After Woldseth, 1973; Fig. 4–1.)

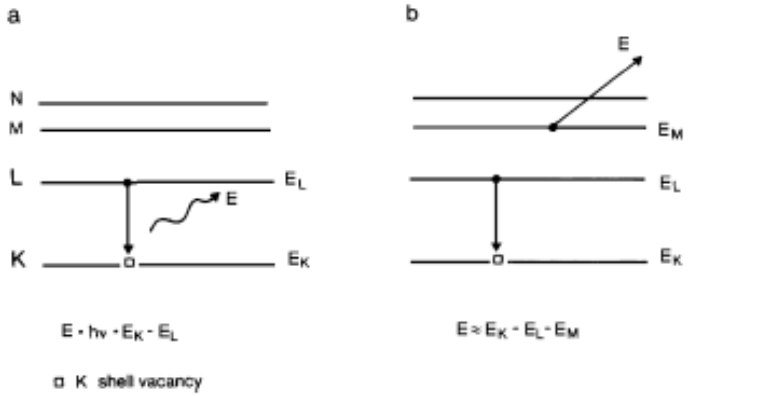

Figure 2.6 The X-ray emission and Auger processes. An inner vacancy in the K shell de-excites via one of two competing processes – (a) X-ray emission, in which an L electron drops down and the excess energy is carried away by an X-ray photon, or (b) the Auger process, in which an L electron drops down, but the excess energy is carried away by a third electron – in this case from the M shell.

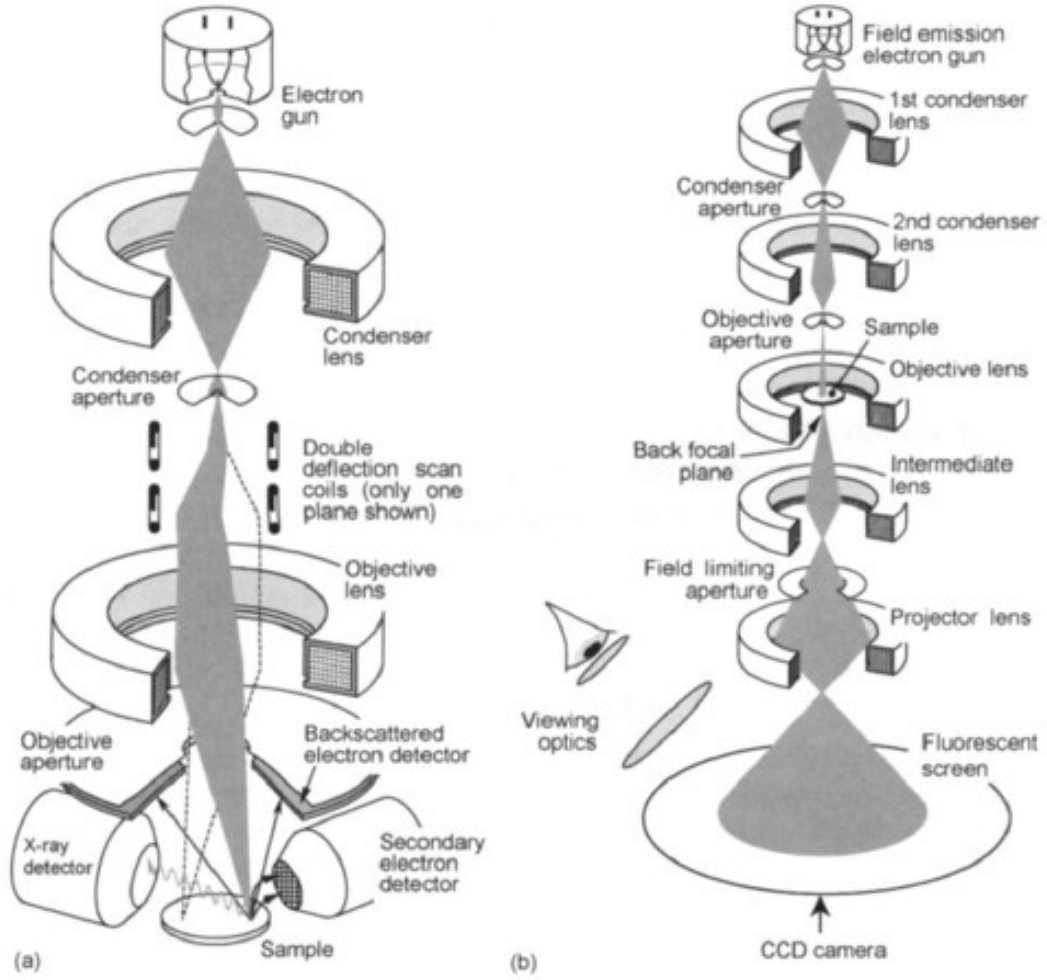

Fig. 3.1. General types of electron microscope. (a) Scanning electron microscope (SEM); (b) transmission electron microscope (TEM).

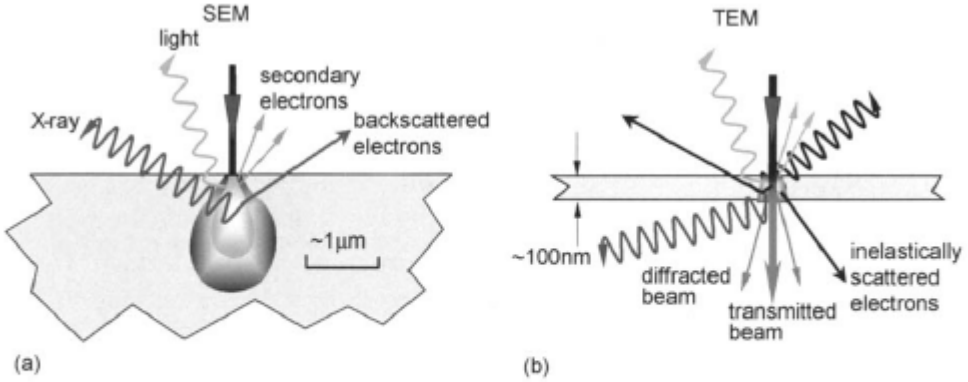

Fig. 3.2. Interaction of electrons with a solid showing effects of interaction volume. (a) SEM sample; (b) sample thinned for TEM.

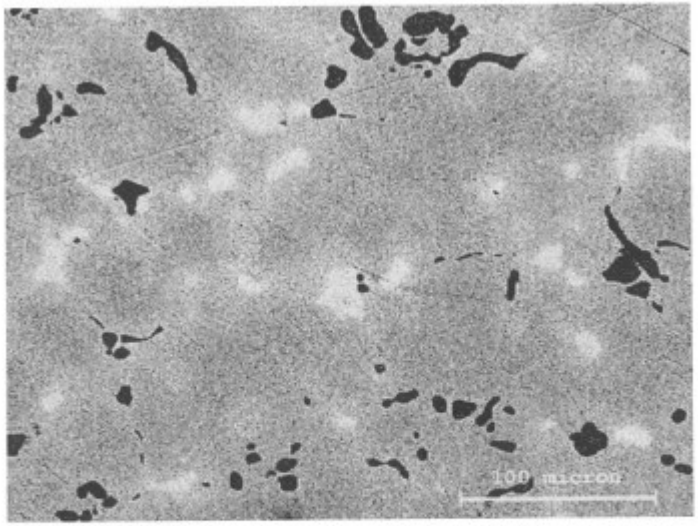

Fig. 3.25. BSE image of a copper–arsenic alloy. The alpha phase is composed of regular grains, containing 3% As. Along the grain boundaries Cu_3As intermetallics, with an As concentration up to 28% (bright phase), are present next to copper sulphide inclusions (dark phase). Magnification 400 [67]. Reproduced with permission from TMS Publications.

Fig. 1. Photograph of the coin of post-Roman Empire examined in this study. Its diameter was approximately 15 mm.

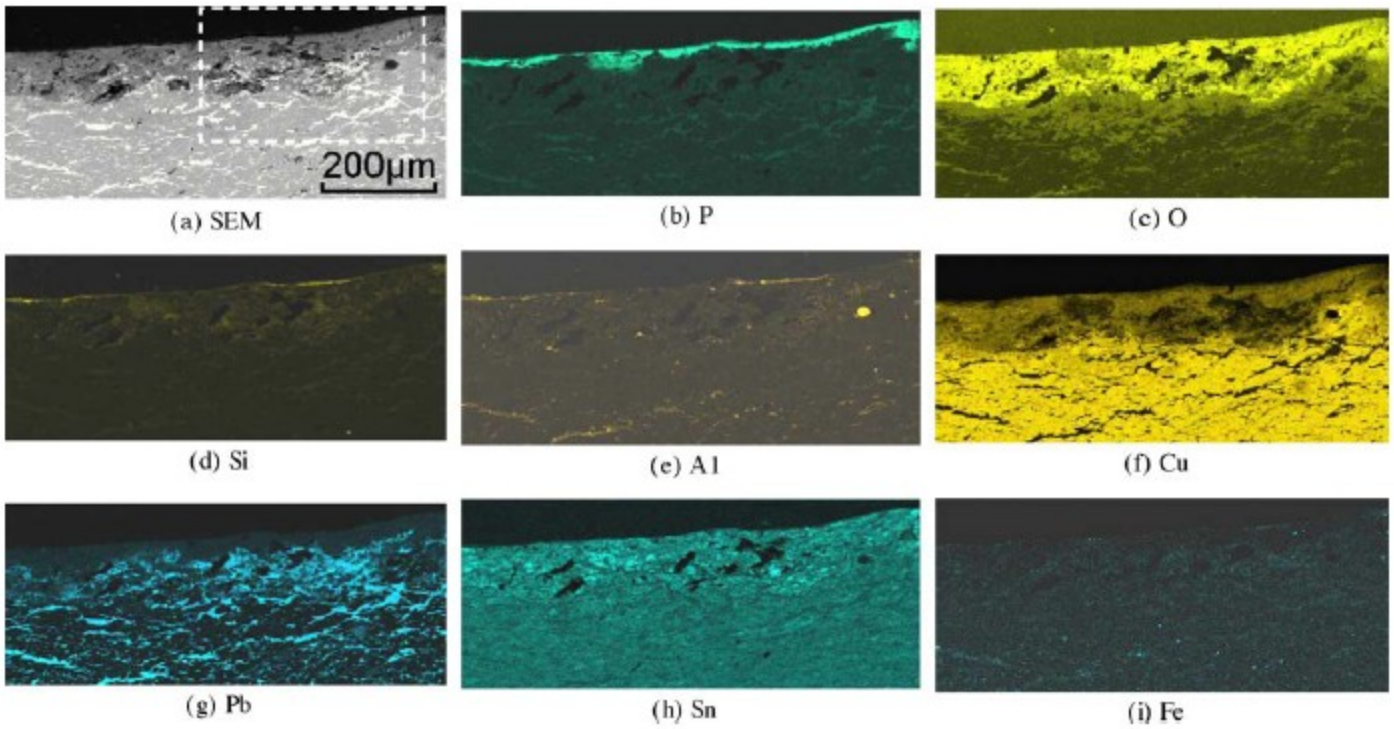

Fig. 2. SEM picture (a) and EDS analyses (b–i) of the cross-section of the post-Roman bronze coin. The dashed rectangle in (a) corresponds to the area where EDS analyses were performed (cf. Fig. 3).

Synchrotron Radiation-XRF

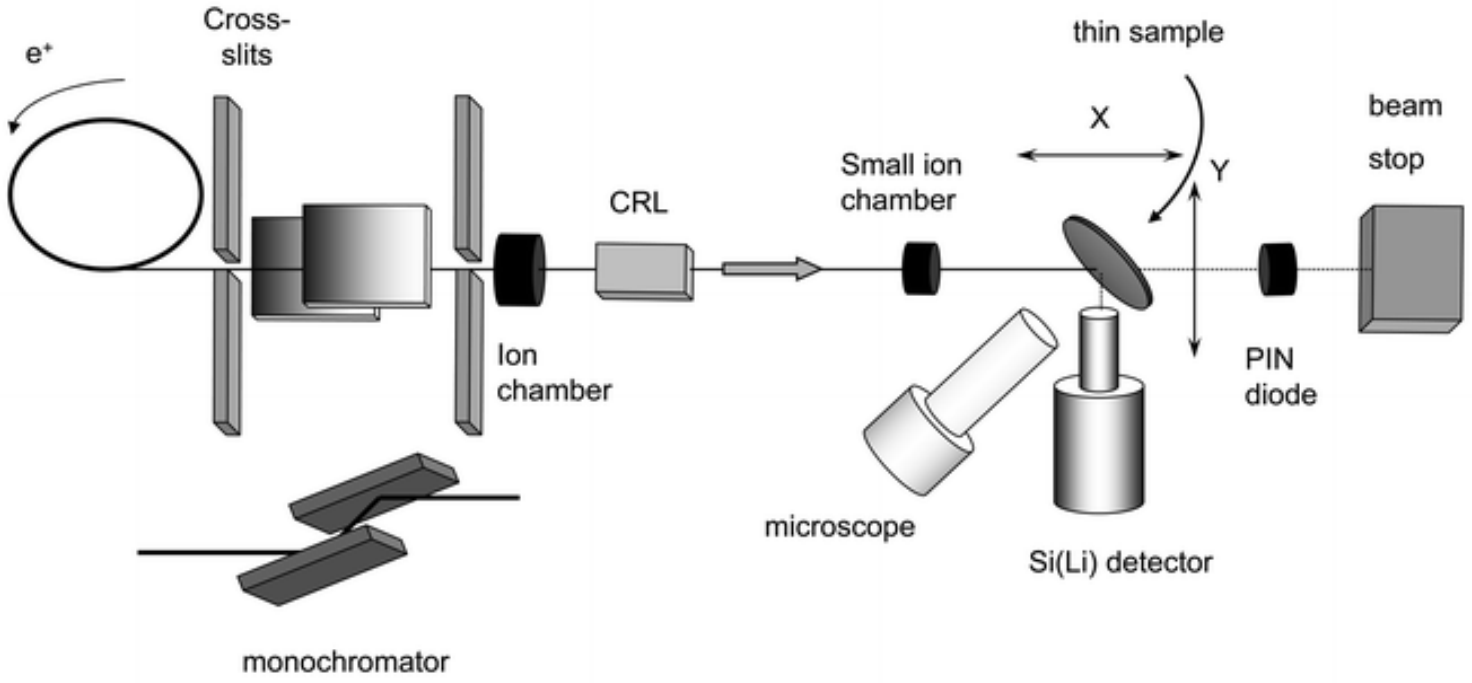

SR-XRF

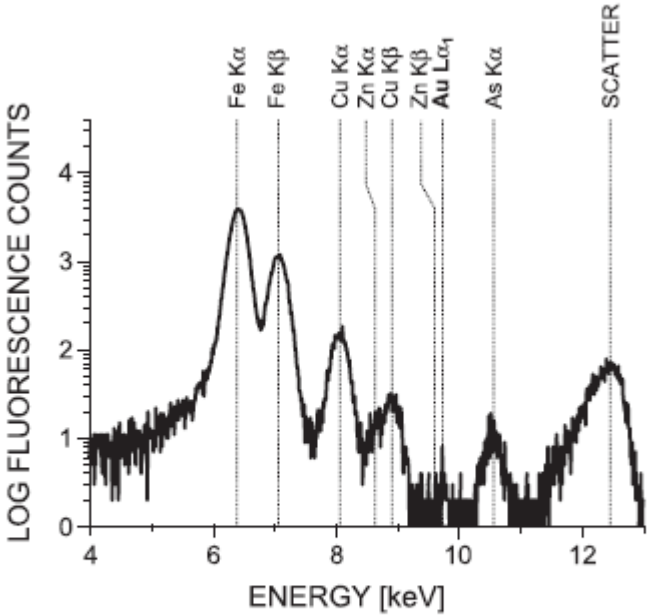

Fig. 6. X-ray fluorescence spectra collected from the surface of an ancient sword ('graveyard sword') dating from the late Iron Age. Excitation energy was set to 13.00 keV, X-ray beam size was 5×5 μm^2. Semi-logarithmic representation.

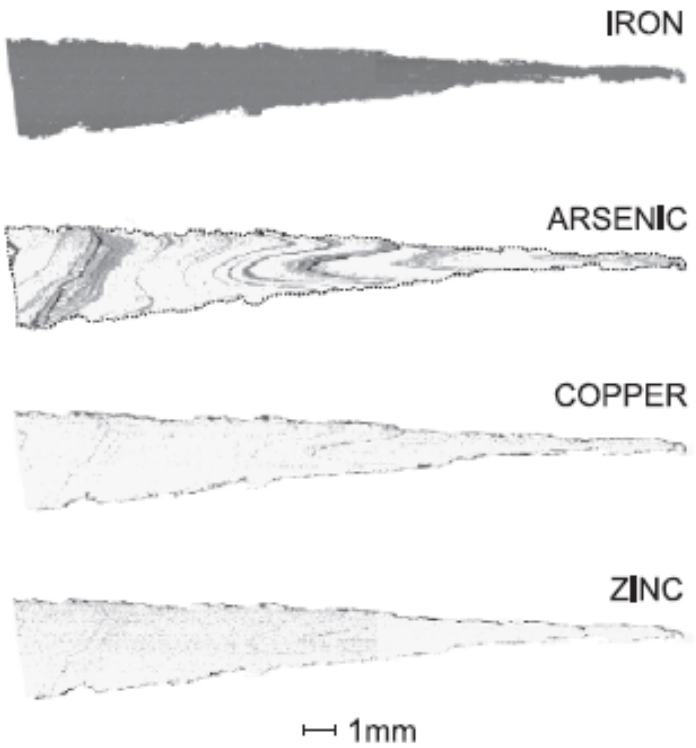

Fig. 5. Elemental distribution of Fe, As, Cu, and Zn detected by micro-XRF within a cross-section of an ancient sword ('graveyard sword') dating from the late Iron Age. In case of arsenic a dotted line is included as contour reference.

Fotoelektronová spektroskopie (ESCA)

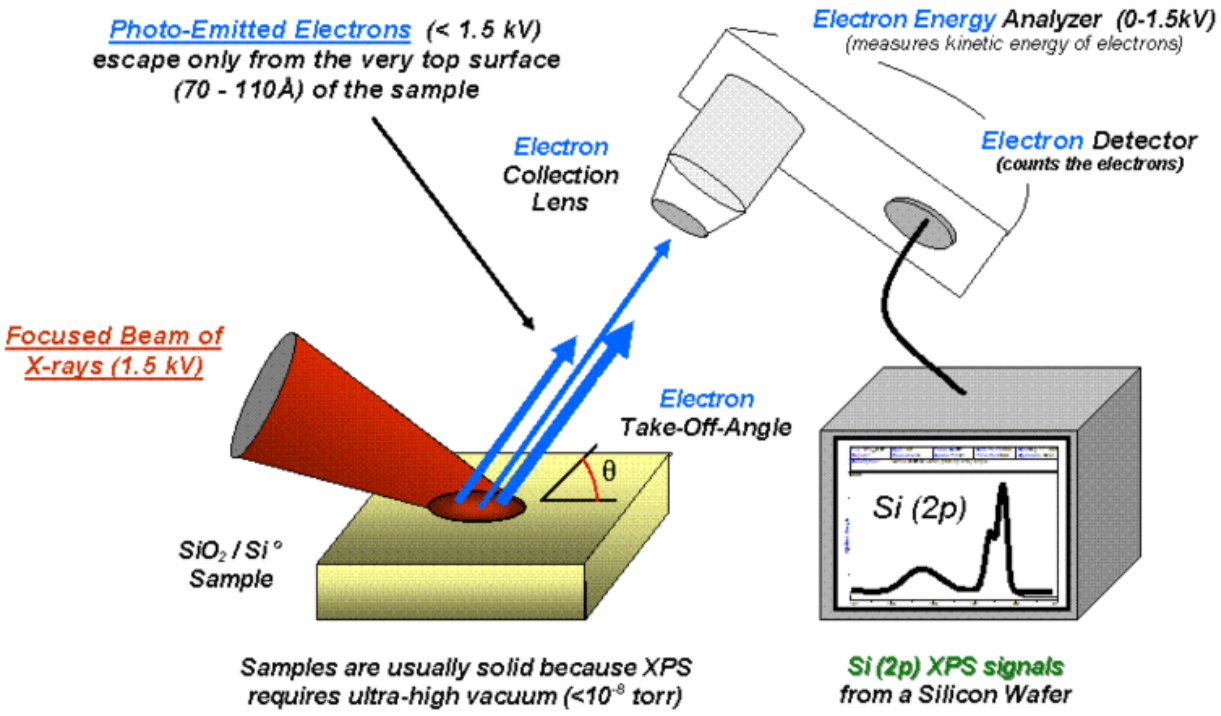

Ultrafialová (UPS)
Rentgenová (XPS)

Sledování kinetické energie fotoelektronů,
Ta závisí na energii molekulového orbitalu.

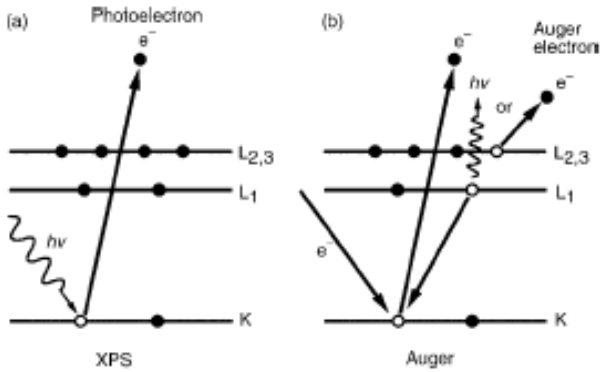

Figure 7.1 Emission processes of characteristic electrons: (a) a 1s photoelectron; and (b) a $KL_1L_{2,3}$ Auger electron

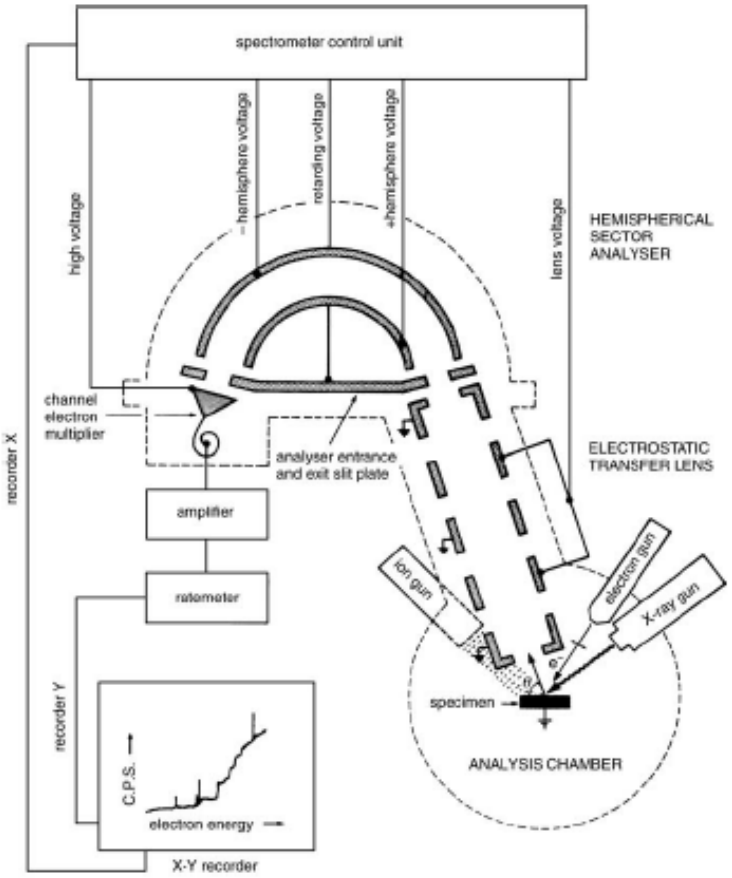

Figure 7.5 Structure of an electron spectrometer. (Reproduced with permission from J.F. Watts, *An Introduction to Surface Analysis by Electron Spectroscopy*, Oxford University Press, Oxford. © 1990 Royal Microscopy Society.)

Serratus – římská republikánská mince

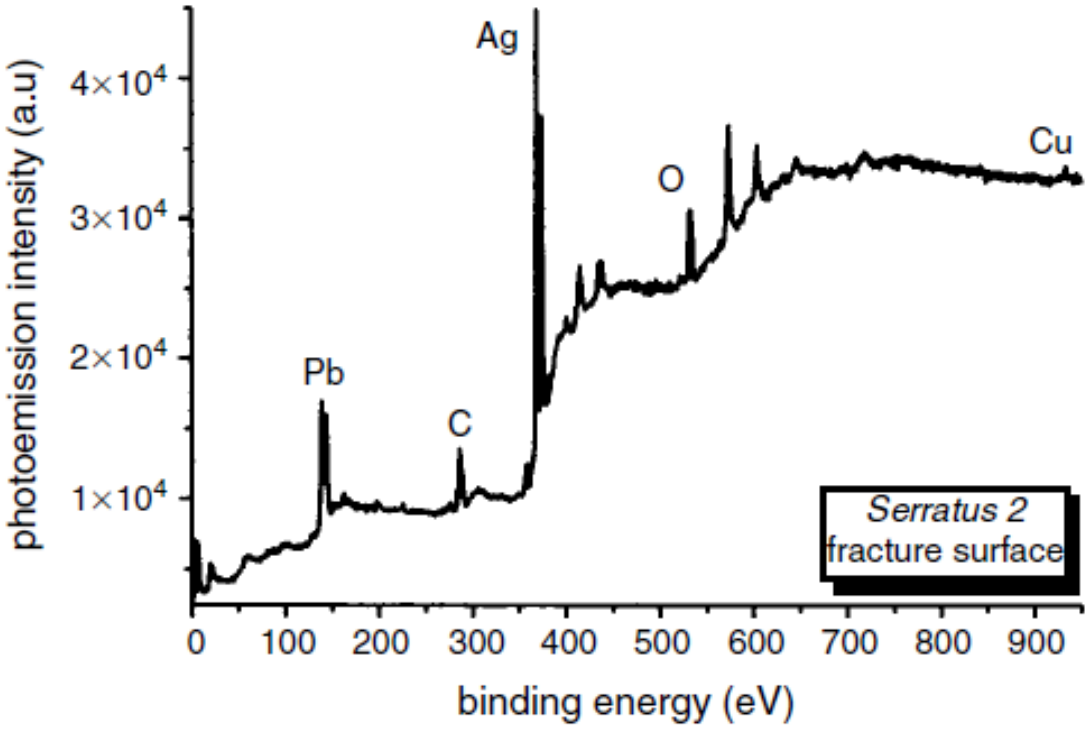

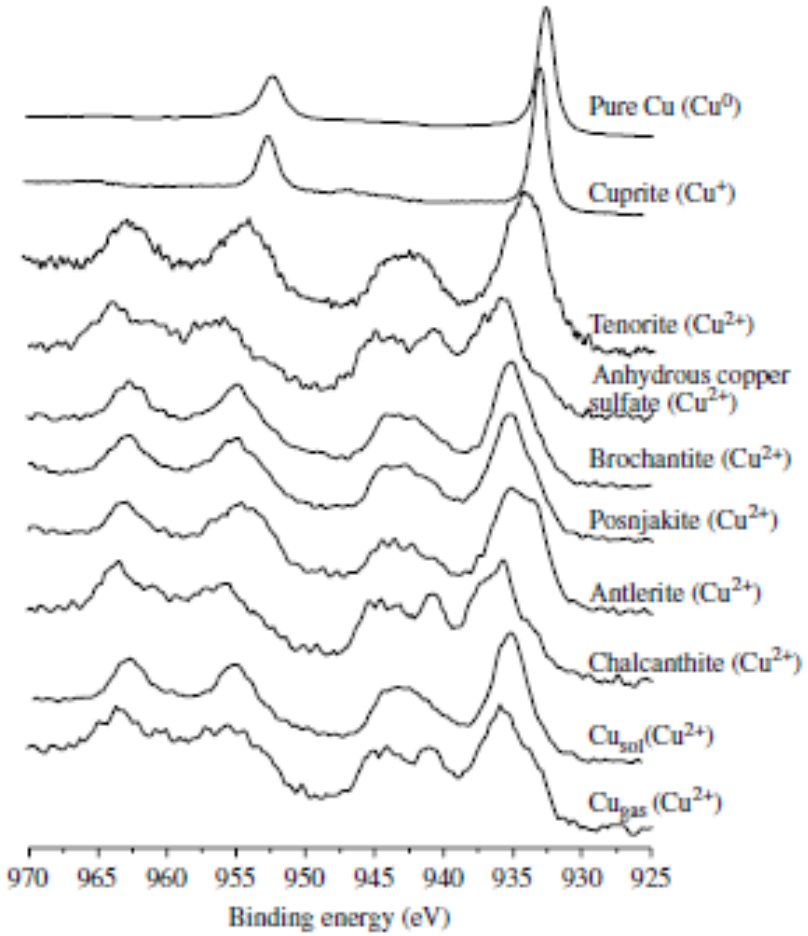

Figure 1. Normalized Cu 2p regions of the different compounds. From top to bottom: copper, cuprite, tenorite, anhydrous copper sulfate, brochantite, posnjakite, antlerite, chalcanthite, artificial weathering in solution at 20 °C, artificial weathering in SO_2 atmosphere.

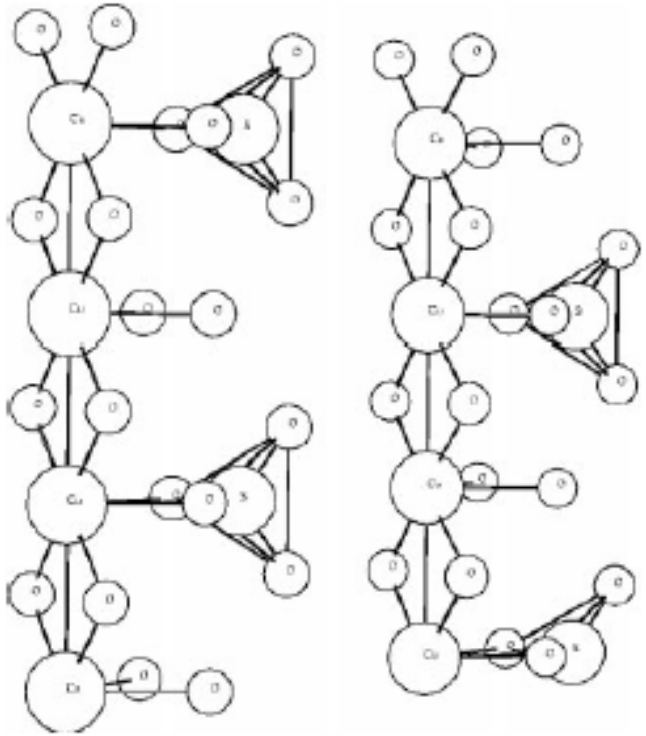

Figure 2. Structure of brochantite, realized with the software XMAKEMOL, using data from Ref. 8.

PIXE a PIGE

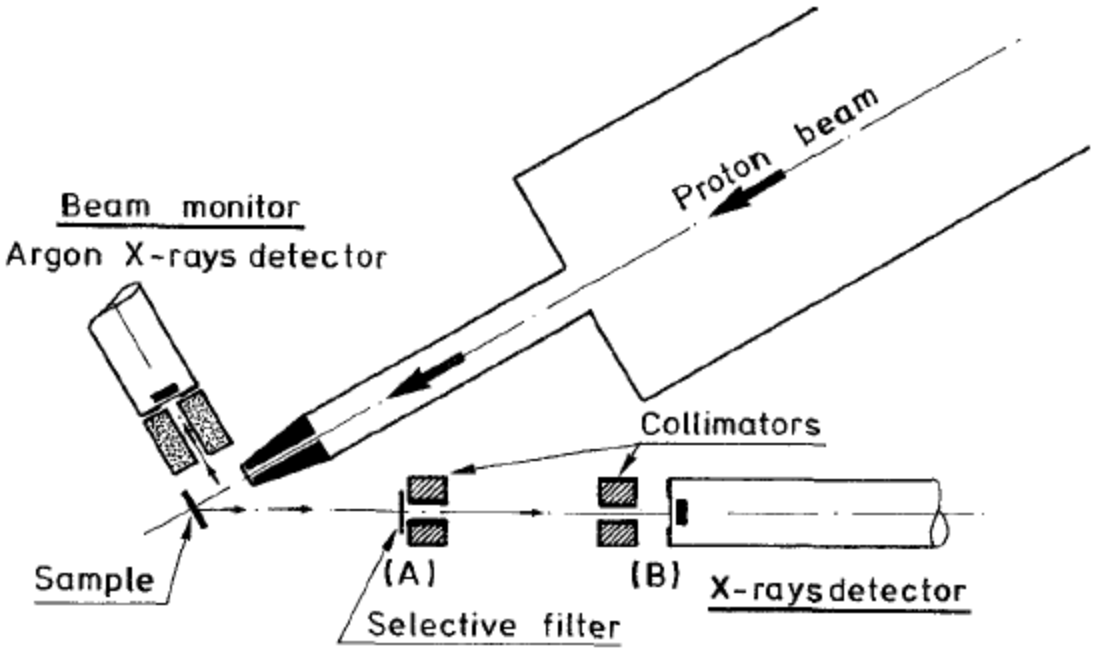

Fig. 11.1. The non-vacuum PIXE set-up used at LARN.

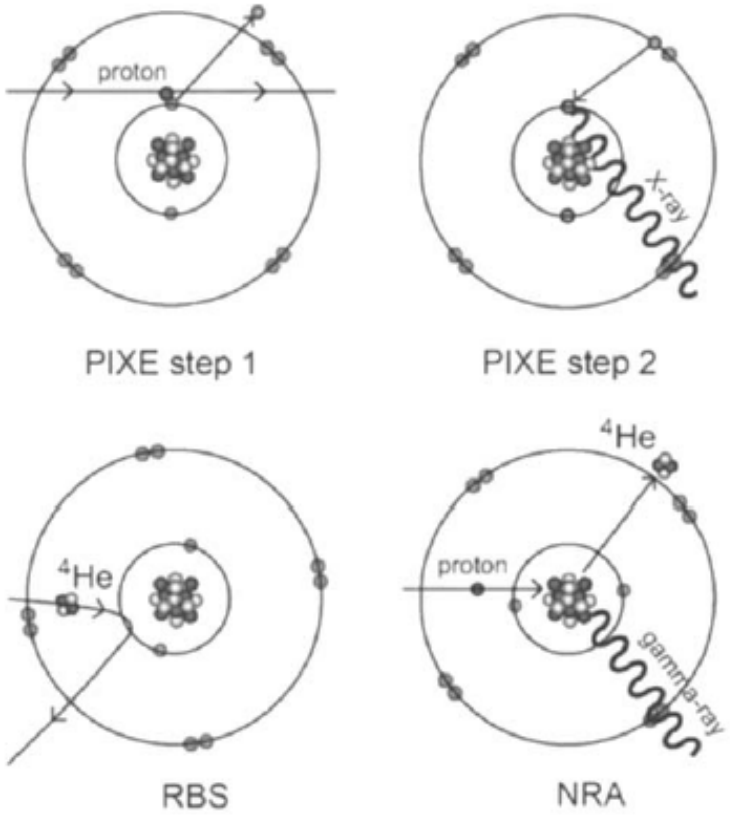

Fig. 5.1. Physical principles of IBA techniques. Particle-induced X-ray emission (PIXE) is a two-step process: an inner-shell electron of the target atom is expelled by the impinging ion, then follows an electronic rearrangement accompanied by X-ray emission. Rutherford backscattering spectrometry (RBS) relies on a purely elastic process based upon the electrostatic repulsion between positively charged projectile and target nuclei. NRA occurs when the projectile and the target nuclei come close enough to undergo a nuclear reaction with emission of characteristic photons or charged particles.

Akrotiri Řecko

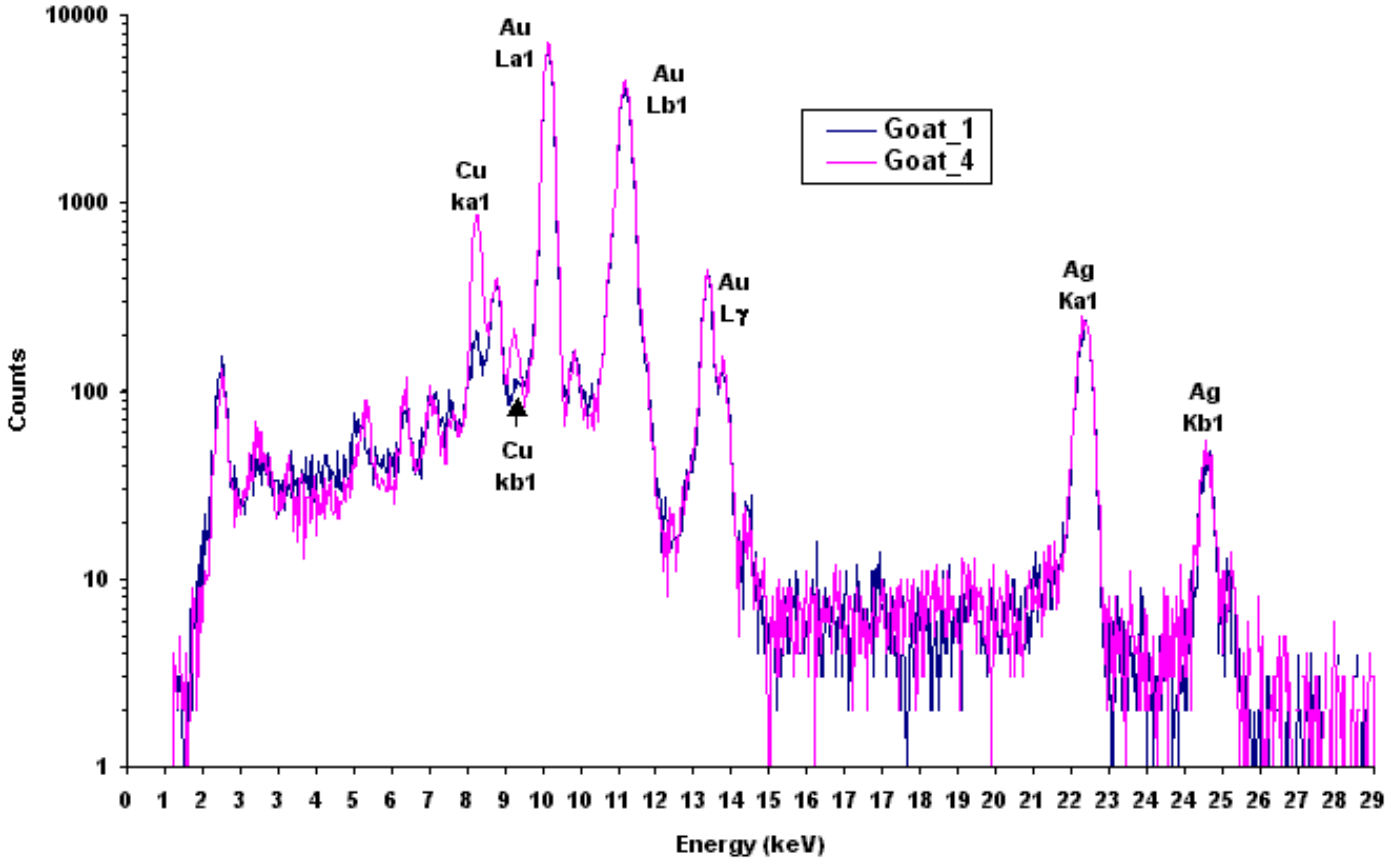

Figure 2 - Koson gold coin (Dacian stater)

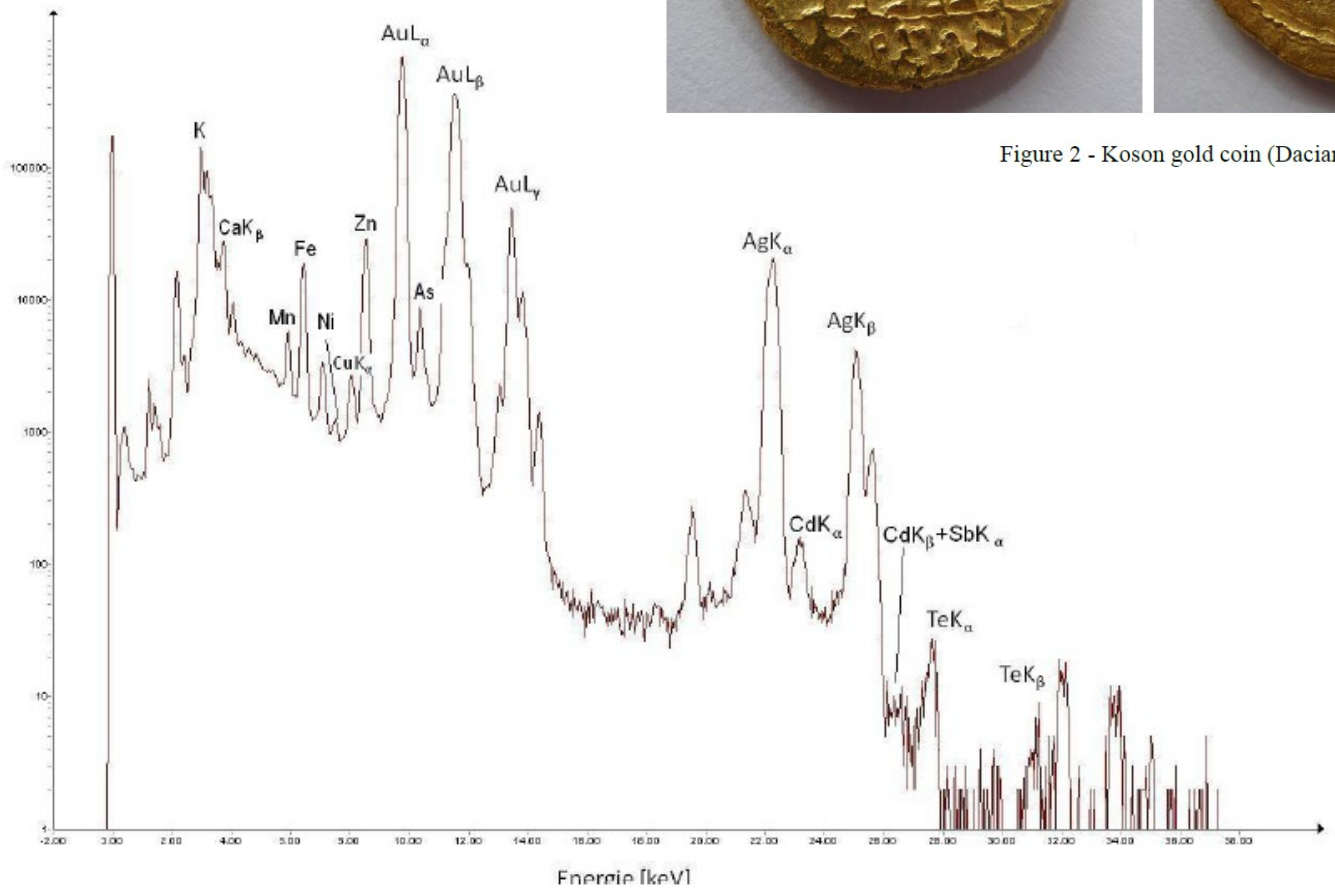

Figure 4 - Micro-PIXE spectrum – native gold sample - Cavnic

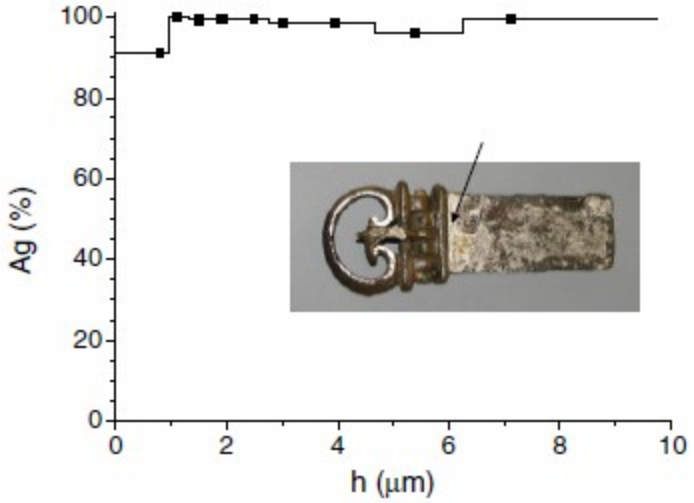

Fig. 4. Silver layer on the Roman belt buckle made of brass.

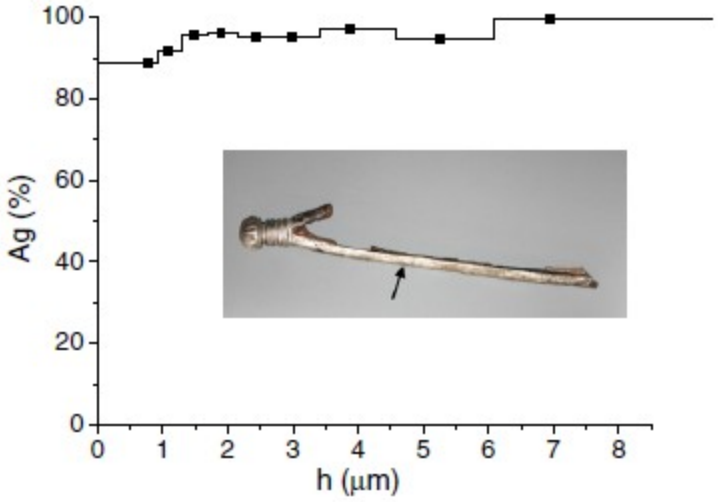

Fig. 5. Silver layer of the iron scabbard border.

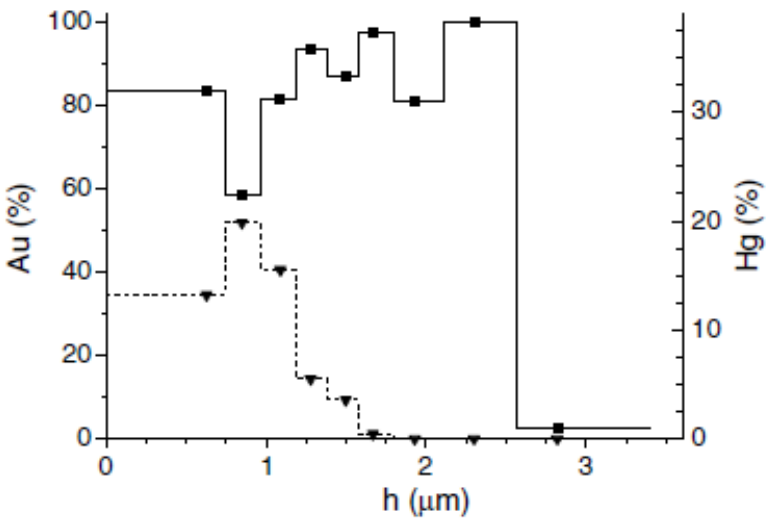

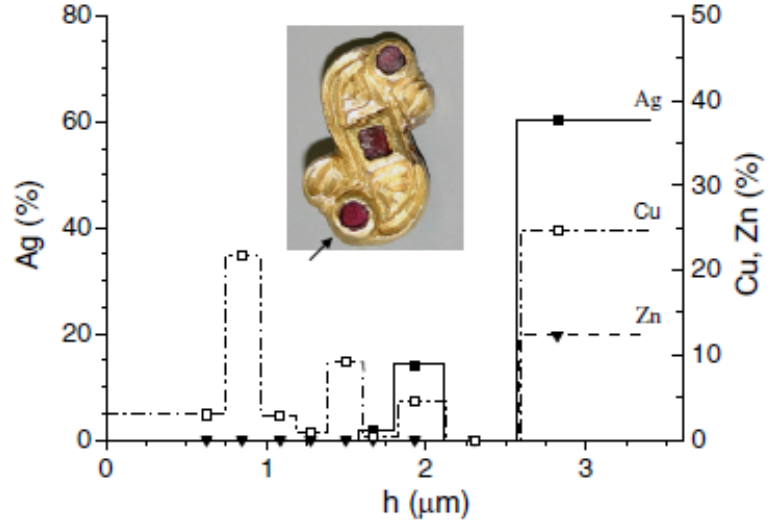

Fig. 6. Gilding layer on the S-type brooch.

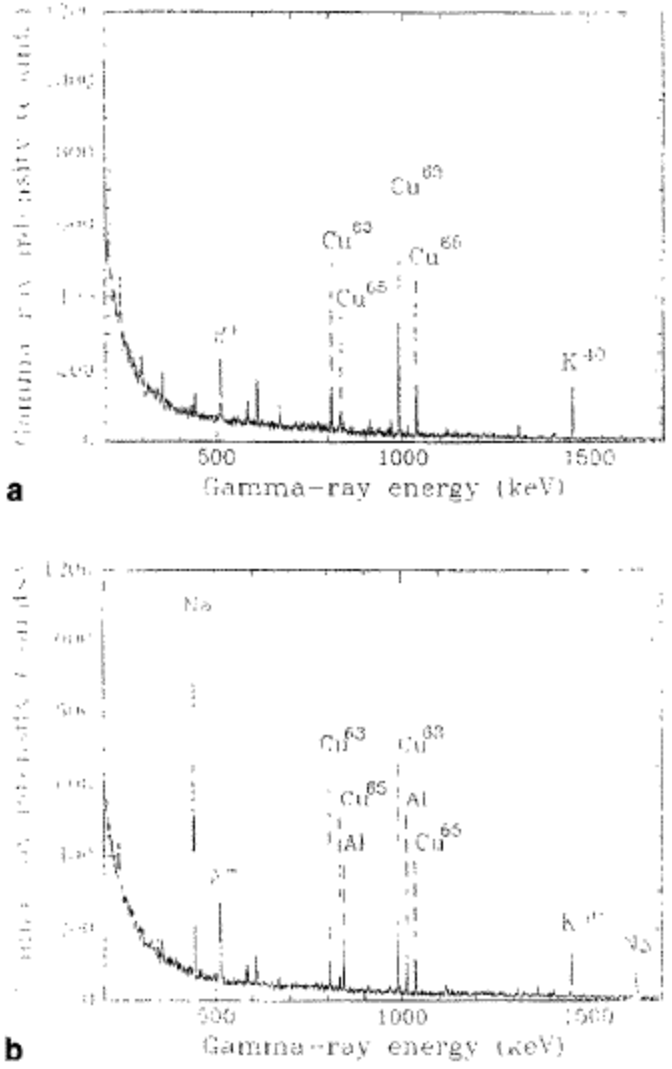

Fig. 6. 2.5 MeV PIGE spectrum of the sheet from Santa Flora (Teruel): (a) bulk and (b) patina. Spectrum (b) was obtained simultaneously with the RBS spectrum of Fig. 4(b).

2. Schematic drawings of the archaeological bronzes: (1) from Castrelín de Paluezas (León), (2) perforated sheet Castrelín de Paluezas (León), and (3) sheet from Santa a (Teruel).

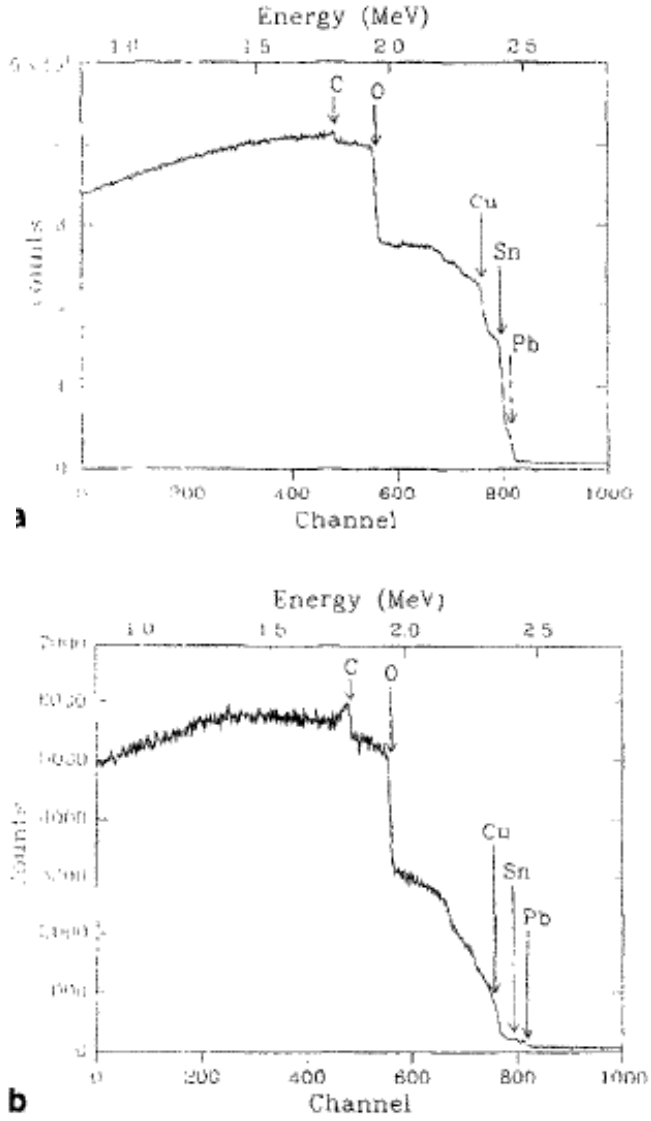

Fig. 4. 2.5 MeV RBS spectrum from a patina covered region of (a) the perforated sheet from Castrelin de San Juan de Paluezas (León), and (b) sheet from Santa Flora (Teruel).

Secondary Ion Mass Spectrometry

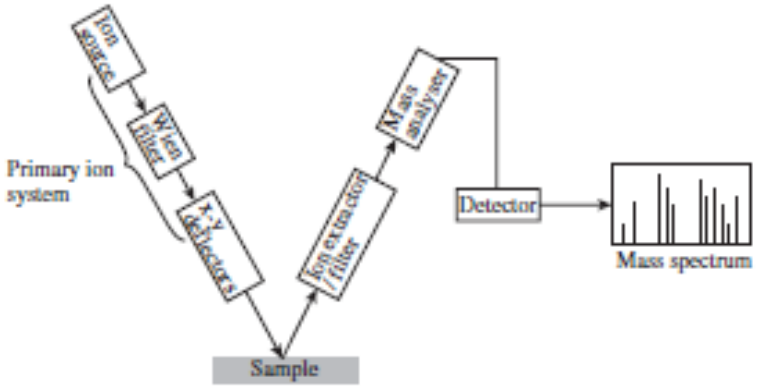

Figure 8.5 SIMS instrumentation.

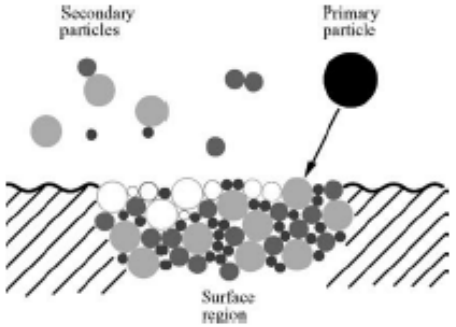

Figure 8.1 Secondary particle generation by an energetic primary particle.

Ar+
Xe+

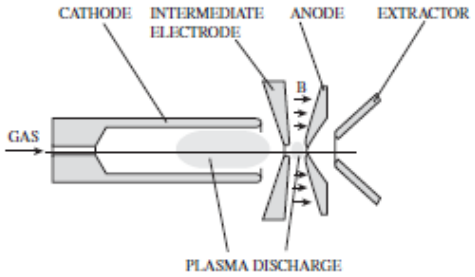

Figure 8.7 Duoplasmatron ion source. The magnetic field marked **B** intensifies the plasma by confining electrons close to the axis. (Reproduced with permission from J.C. Vickerman and D. Briggs, *ToF-SIMS Surface Analysis by Mass Spectrometry*, IM Publications and SurfaceSpectra, Chichester and Manchester. © 2001 IM Publications.)

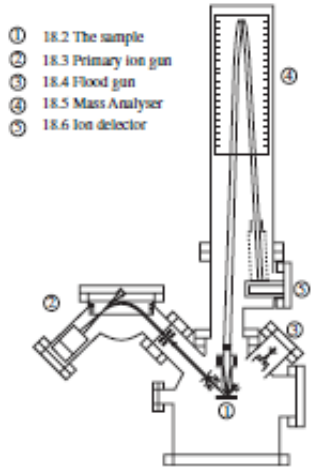

Figure 8.13 Time-of-flight SIMS instrumentation. (Reproduced with permission from J.C. Vickerman and D. Briggs, *ToF-SIMS Surface Analysis by Mass Spectrometry*, IM Publications and SurfaceSpectra, Chichester and Manchester. © 2001 IM Publications.)

Tell Beydar (Izrael)

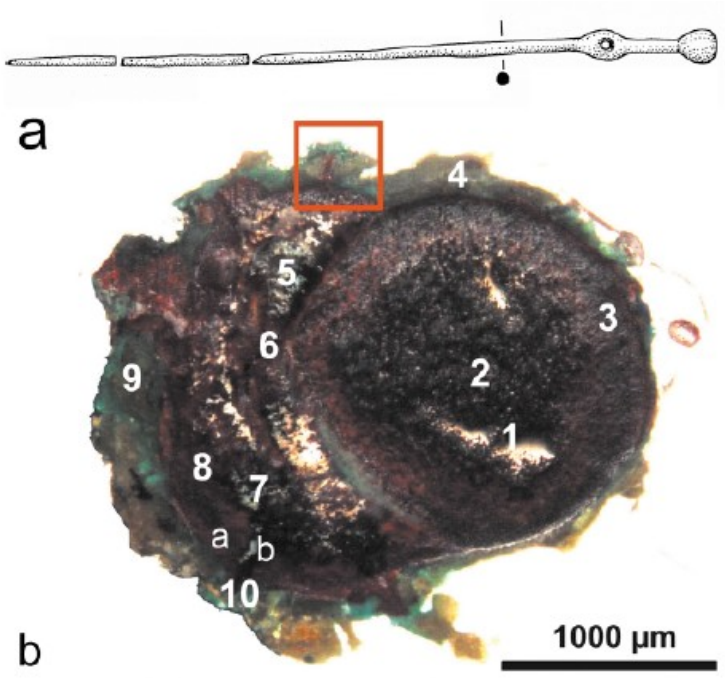

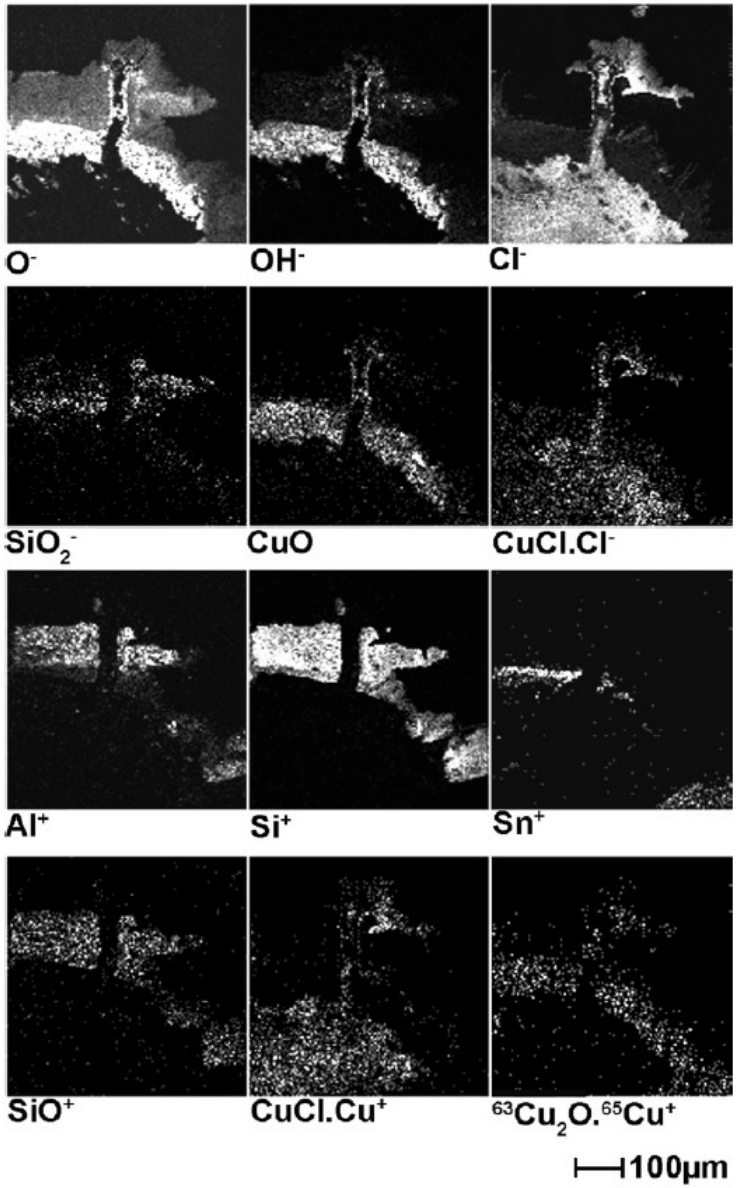

Fig. 3 Ion images of sample B18 obtained with TOF-SIMS. The area of analysis is indicated by the square in Fig. 1b

FTIR mikroskopie

Fig. 10.11. Egyptian bronze solid cast statuette of the God Osiris, inlaid with gold and blue glass. The surface has been extensively altered to massive light blue and dark green corrosion, identified as an overall patina of atacamite, with patches of chalconatronite. Frontal view. (*For a colored version of this figure, see Plate 10.III.*)

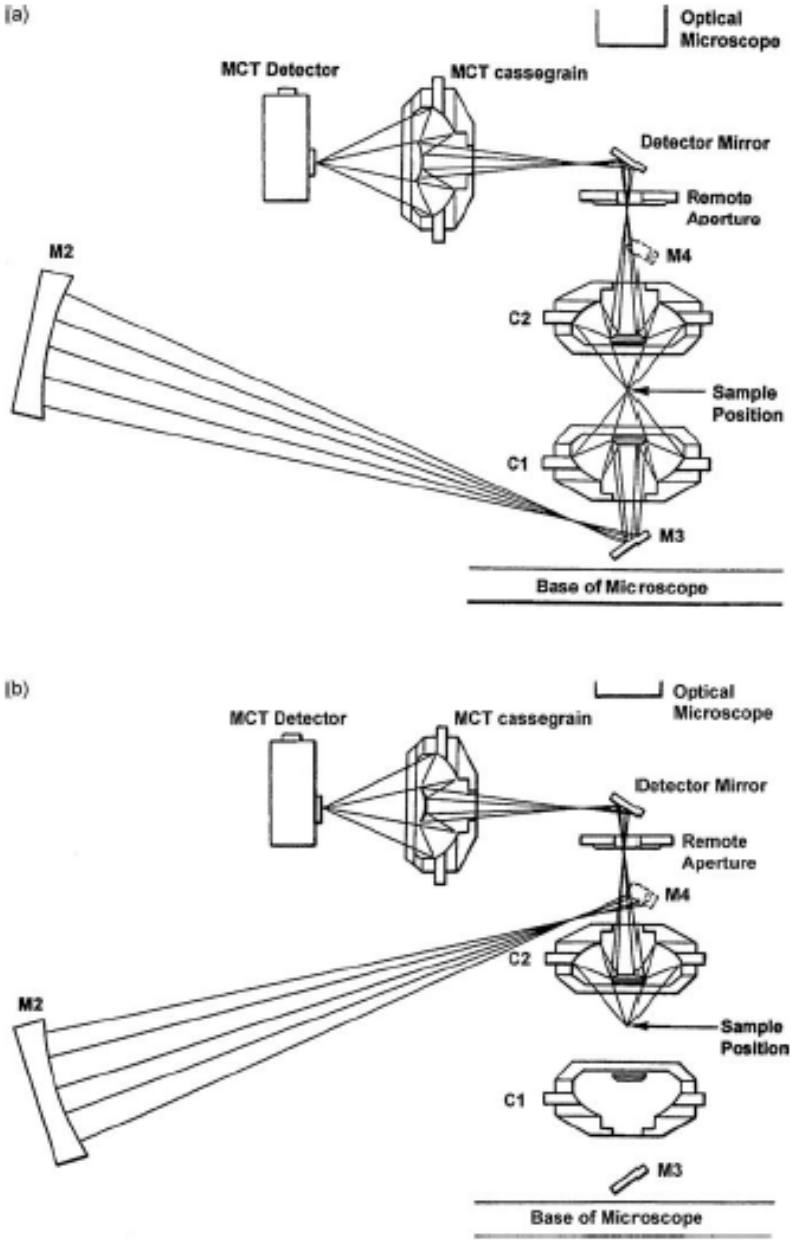

Figure 9.25 Optical paths of FTIR microscope with IR radiation: (a) transmittance; and (b) reflectance. M, mirror; C, Cassegrain lens. (Reproduced by permission of PerkinElmer Inc.)

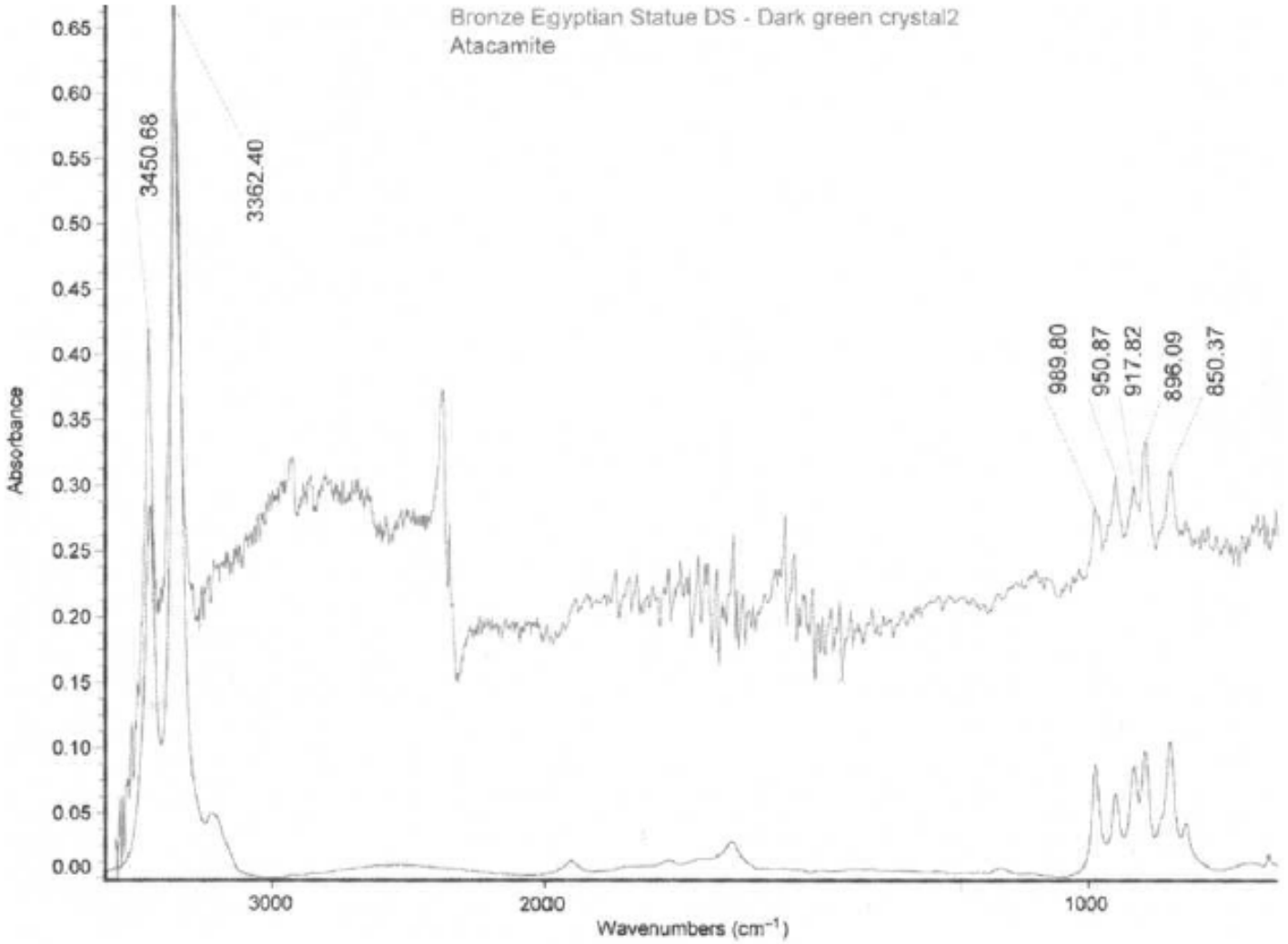

Fig. 10.17. FTIR Spectrum obtained, in situ, from the dark green surface of the Egyptian bronze Osiris shown in Fig. 10.11. The patina was shown to be of atacamite, but the result was only obtained with some difficulty and the chalconatronite patina could not be identified by this technique without sampling.

Ramanova mikroskopie

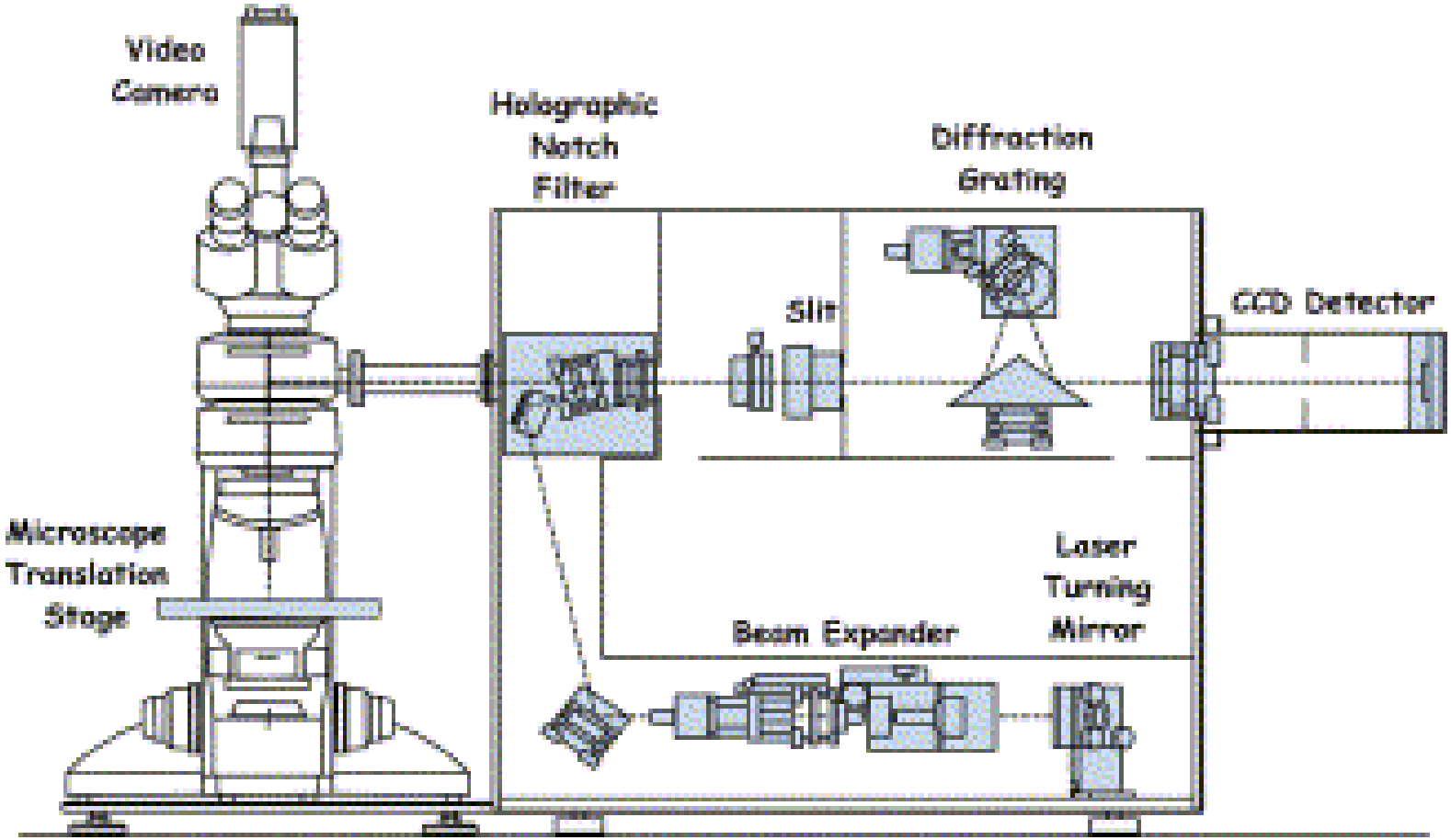

Ramanova mikroskopie maleb

Portrét mladíka **(neznámý severoitalský malíř, cca 1515)**

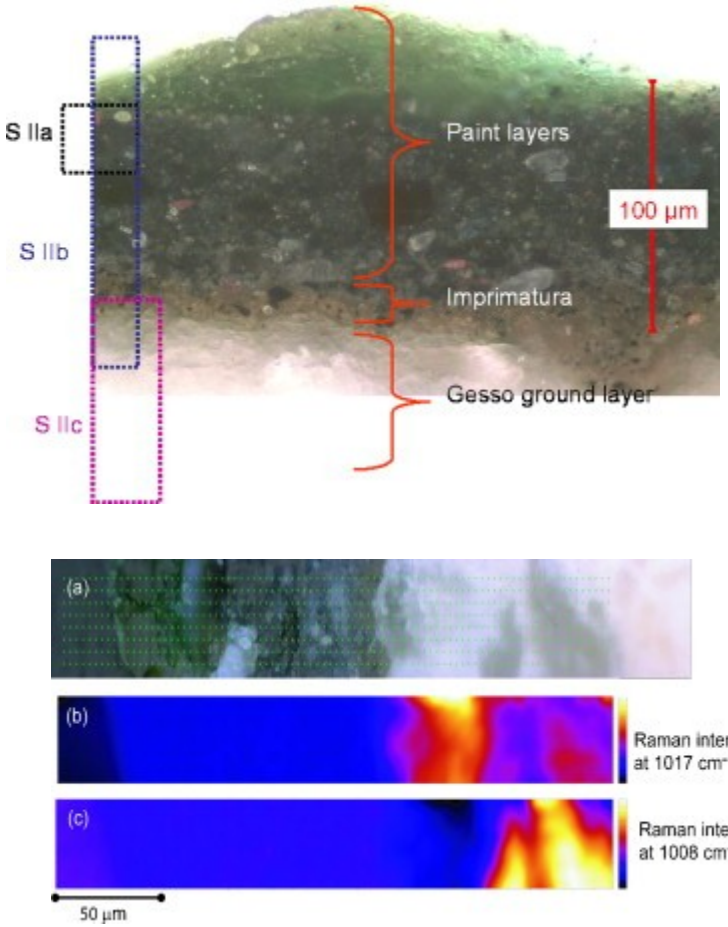

Ramanovské mapy vzorku S IIb.
(a) optický obraz, (b) anhydrit, (c) sádrovec (gypsum).

Ramanova mikroskopie

mikrofosilie
v jurských
rohovcích

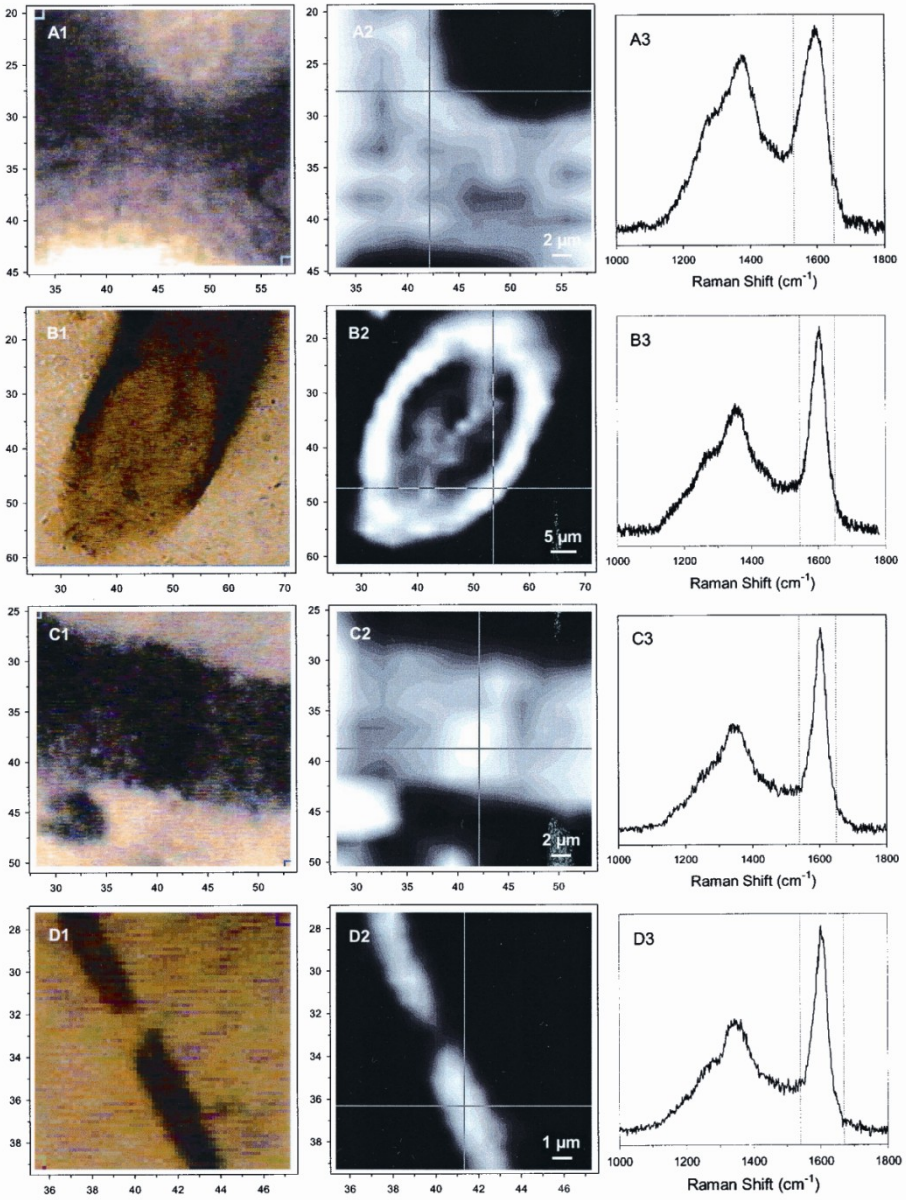

Fig. 1. Optical images (column 1), Raman images (column 2), and spectral bands used for Raman imaging (column 3) of permineralized carbonaceous fossils at or near the upper surfaces of polished chert thin sections: (*A*) Cell wall in the conductive tissue (lignified xylem) of an aquatic fern cf. *Dennstaedtia* from the essentially unmetamorphosed ≈45-Ma-old Clarno Formation of Oregon. (*B*) Tangential section of the tubular sheath of a *Lyngbya*-like oscillatoriacean cyanobacterium in a conical stromatolite (*Conophyton gaubitza*) from the subgreenschist facies ≈650-Ma-old Chichkan Formation of Kazakstan. (*C*) Transverse cell wall of a broad cellular trichome (*Gunflintia grandis*), and (*D*) a narrow prokaryotic filament (*G. minuta*), in domical stromatolites of the greenschist facies ≈2,100-Ma-old Gunflint Formation of Ontario, Canada. Each Raman image was produced by combining several hundred pixel-assigned point spectra (''spexels''), like those shown for each specimen in column 3, acquired over a small square part of the total area analyzed. The resolution of the Raman images is defined by the pixel dimensions of their component spexels; for *A*–C, 2 μm per pixel, and for *D*, 0.5 μm per pixel.

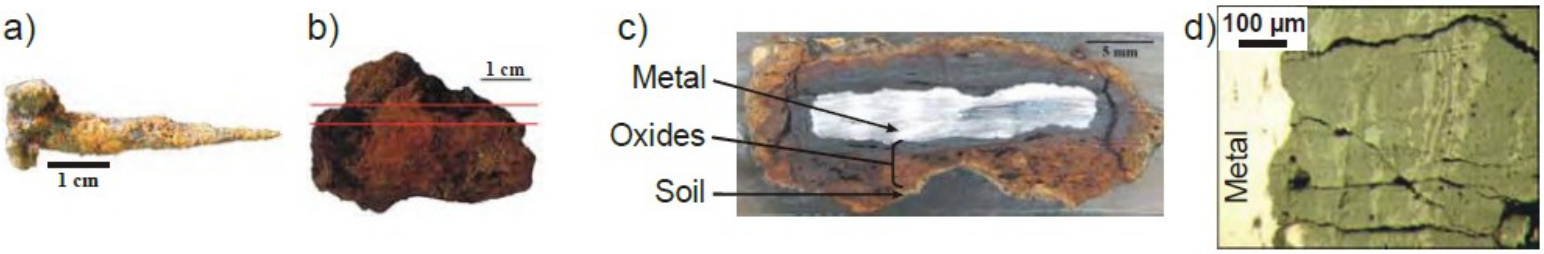

Fig. 1. Examples of studied excavated objects. a) nail, b) plate, c) cross-section of the whole corrosion system, d) micrography of the corrosion layers (sample Cab21h, Cabaret site).

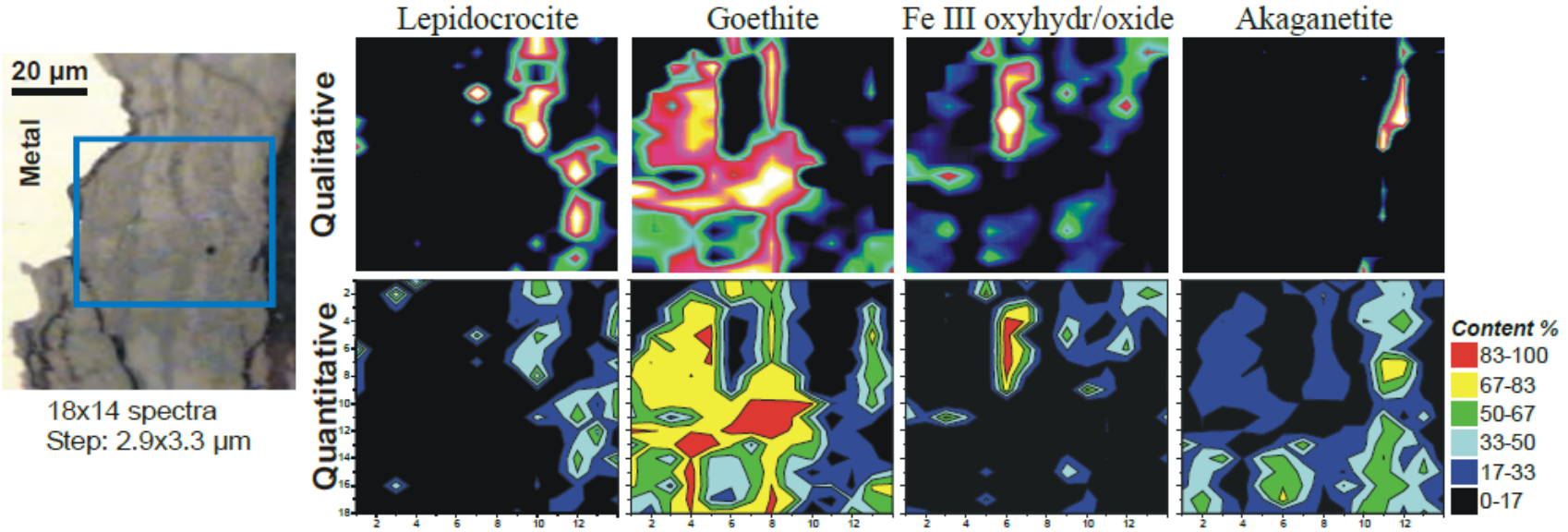

Fig. 9. Raman structural imaging (sample Am IVE110, Amiens, obj. x50) with the comparison of phase mapping between qualitative treatment (from spectrum region of interest) and semi-quantitative results from spectral decomposition.

Raman + FTIR mikroskopie